On the application of an eddy viscosity turbulence model sensitized to rotation/curvature to the cyclone separator

Yaser H. Alahmadi
Department of Mechanical Engineering
The University of Sheffield

This thesis is submitted for the degree of
Doctor of Philosophy

Jan 2016

I would like to dedicate this thesis to my grandfather Mr. Atiqullah Alahmadi for his love and spiritual support. I would also like to dedicate this thesis to my parents Mr. Hussain Alahmadi and Mrs. al Jawza Alahmadi. Thank you both for your love and support throughout my life. Special thanks to my wife Anood for her love, support, and enthusiasm and to my children Omar and Yousef.

I would like to sincerely thanks my supervisor Dr. Andrew Nowakowski for his encouragement, guidance and support during this study. I have been extremely lucky to have a supervisor who cared so much about my work, and who responded to my questions and queries so promptly.

Declaration

I hereby declare that except where specific reference is made to the work of others, the contents of this thesis are original and have not been submitted in whole or in part for consideration for any other degree or qualification in this, or any other University. The work reported in this thesis has been executed by myself, except where due acknowledgement is made in the text.

Yaser H. Alahmadi

Jan 2016

Abstract

The gas-solid separator devices are used in modern industries for a variety of reasons. In some instances, they are used to recover the solid particles as a product, such as those used in the food industry. In other cases, the interest is in separating the particles to purify the gaseous phase. Since the first invention of the cyclone device, a large number of researches and investigations have been reported in the literature. These studies have focused mainly on the flow pattern as well as the performance of the cyclone in terms of collection efficiency and pressure drop. Due to the exponential growth of computing power over the last decade, most researches have tended to study the flow in cyclones and predict the performance parameters by means of computational Fluid Dynamics (CFD). This alternative approach has been proven to be a convenient tool for studying the performance of the cyclone rather than expensive experimental studies.

The vast majority of numerical studies that have been conducted to investigate the flow within cyclones were performed using either Large Eddy Simulation (LES) or the Reynolds Stress Model (RSM). Although these approaches have demonstrated a high capability to deal with swirling flows, these techniques are often impractical for complex design studies, where computational speed and robustness are the key factors. For this reason, recent studies have tended to focus on eddy-viscosity models that are sensitized to rotational and curvature effects.

The objective of this thesis is fourfold. (1) To implement of the new sensitization of EVMs to rotation and curvature developed by Spalart and Shur and that developed by

Smirnov and Menter; (2) to simplify the rotation correction function further and apply it in the standard SST model developed by Menter; (3) to validate the simplified version of the SST model for a simple 2D case of a duct with a u-turn and an axisymmetric rotating-Lid in a confined cylinder; (4) and to apply the modified version of the sensitized EVMs to predict the swirling flow in the cyclone.

The CFD model of the cyclone is compared with the results of Hoekstra et al. whose study was concerned about the flow field and performance parameter of the cyclone separators. In his study, the geometry of the cyclone is based on the Stairmand high-efficiency cyclone whose design is widely quoted in the literature. The proposed model shows the ability to capture the inverted W pattern of the axial velocity profile as well as the tangential component of the velocity. As the OpenFoam code is based on an explicit solver algorithm, both the time step selection and the orthogonality of the mesh should be treated with great care in order to obtain the proper results.

The results showed that the cyclone flow simulation based on the semi-structured grid type is more efficient in terms of computational time and capacity. This is due to the high non-orthogonal faces which are produced when using the structured grid. However, the predictions of the flow pattern inside the conical section showed that the structured grid is more accurate. In addition to that, the numerical discretization schemes of the convection terms play a crucial role in the accuracy of the numerical results. The second order upwind scheme, which is known as Linear Upwind (LU), is the only one that predicts the tangential velocity profile with a high degree accuracy. The other schemes show incapability to represent both the Rankine vortex structure near the cyclone wall, and inverted W pattern of the axial velocity.

Contents

List of Figures

List of Tables

Nomenclature

Roman Symbols

$\overline{u}$	time average velocity	$\mathrm{m/s}$
a	cyclone inlet height	m
b	cyclone inlet width	m
B_C	cyclone cone-tip diameter	m
D	cyclone barrel diameter	m
D_p	particles diameter	m
D_x	vortex finder diameter	m
f_{r1}	Spalart and Shur rotation function	
f_{rot}	Smirnov and Menter rotation function	
H	distance separates the mean gas flow from chambers	m
H_t	cyclone total height	m
k	turbulent kinetic energy	$\mathrm{m/s^2}$
L	length of the parallel plates	m
p	static pressure	$\mathrm{kg \cdot s^2/m}$
Q	volume flow rate	$\mathrm{m^3/s}$
S	vortex finder length	m
u'	fluctuation velocity	$\mathrm{m/s}$

u_i	flow velocity component in the i^{the} direction	m/s
u_t	tangential velocity	m/s
v	fluid velocity	m/s
W	width of the chamber	m
w	axial velocity	m/s

Acronyms

CD	Central Differencing scheme
CFD	Computational Fluid Dynamics
Co	Courant Number
DES	Detached Eddy Simulation
EVM	Eddy Viscosity Model
GIGO	Garbage In, Garbage Out
LES	Large Eddy Simulation
LLU	Limited Linear Upwind scheme
LU	Linear Upwind scheme
NVD	Normalised Variable Diagram scheme
OpenFoam	Open Field Operation and Manipulation
PIMPLE	merged PISO-SIMPLE algorithm
PISO	Pressure Implicit Splitting Operator
RANS	Reynolds-Averaged Navier-Stokes Equations
Re	Reynolds Number
SA	Spalart-Allmaras model
SARC	Spalart-Almmaras model with Rotation Curvature
SARCM	Modified Spalart-Almmaras model with Rotation Curvature

SFCD	Self Filtered Central Differencing scheme	
SIMPLE	Semi-Implicit Method for Pressure-Linked equations	
SST	Shear Stress Transport model	
SSTCC	Shear Stress Transport model with Curvature Correction	
SSTCCM	Modified Shear Stress Transport model with Curvature Correction	
TVD	Total Variation Diminishing scheme	
UD	Upwind Differencing scheme	

Greek Symbols

ε	turbulent dissipation	$1/\mathrm{s}$
η	cyclone collection efficiency	
μ	dynamic viscosity	$\mathrm{kg} \cdot \mathrm{m}/\mathrm{s}$
ν	kinematic viscosity	m/s^2
Ω	angular velocity	$1/\mathrm{s}$
Ω	magnitude of the vorticity	$1/\mathrm{s}$
ω	turbulent frequency	$1/\mathrm{s}$
ω_{ij}	mean rate-of-rotation tensor	$1/\mathrm{s}$
ρ	fluid density	kg/m^3
ρ_p	particles density	kg/m^3
τ_{ij}	Reynolds stress tensors	$\mathrm{kg} \cdot \mathrm{s}^2/\mathrm{m}$
$\tilde{\nu}$	viscosity-like variable	m/s^2
υ_t	particle's setting velocity	m/s

Chapter 1

Introduction to Separator Devices

1.1 Introduction and Overview

The gas-solid separator devices are used in modern industries for a variety of reasons. In some instance, they are used to recover the solid particles as a product, such as those used in food industry. In other cases, the interest is in separating the particles in order to purify the gaseous phase. The types of dust collectors can be classified into four main principle categories. They include the inertial separators, fabric collectors, wet scrubbers and electrostatic precipitators. The particle size is the main character that determines which dust collector type should be selected. For instance, if the particles' size is extremely small, *i.e.* in the range of 10^{-2} micron to one micron, the suitable collector device is electrostatic precipitators, whereas the cyclone separator, which is of our main interest, is used if the particle size varies from one micron to 10^3 micron. Figure 1.1 shows the classification of the most famous types of dust collector devices according to the range of the particles size. The following sections discuss briefly the settling chambers, the wet scrubbers and the electrostatic precipitators. The cyclone separator, which is the main subject of this thesis, is discussed in more details.

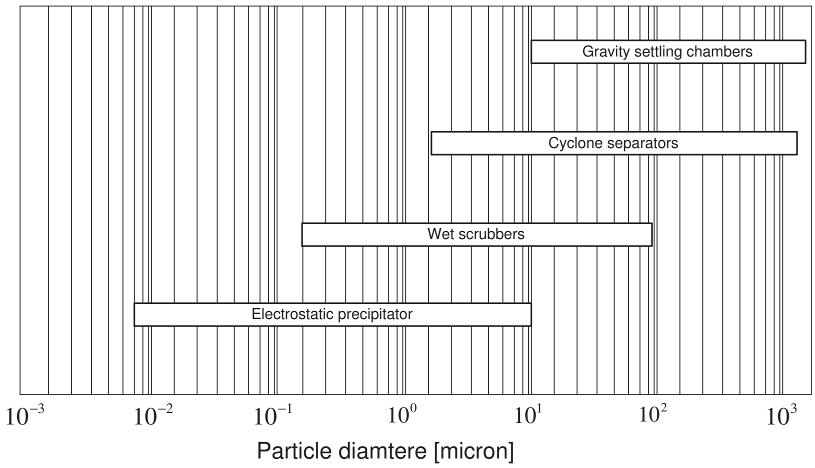

Fig. 1.1 Classification of dust collectors according to particle size.

1.2 Gravity Settling Chambers

Gravity Settling Chambers are the oldest and the simplest type of all the dust collectors. In general, settling chambers are built as a large horizontal box, which consists of hoppers at the bottom of the box with one inlet and one outlet at the top as shown in Figure 1.2. The function of the hoppers is to keep the removed particles trapped inside and then discharged outside the system. The purpose of the chambers is to reduce the flow velocity by increasing the size of the duct or vessel cross section which is located in front of the inlet. As a result of the low velocity, the particles fall down into the hoppers by the effect of the gravitational force.

The settling chambers are used widely in heavy industry and are limited to remove particles of diameter larger than 43 micrometers. Therefore, they are usually used as pre-cleaner devices to remove the larger particles before the gas stream flows through a more efficient dust collector device. The efficiency of the gravity settling chamber differs according to the flow regime. For example, in case of the laminar flow, the particles are distributed uniformly, and thus the vertical mixing between particles does not exist. For this flow regime efficiency of the settling chamber is given by:

$$\eta = \frac{\upsilon_t L}{\overline{u} H} \tag{1.1}$$

Where the $\overline{u}$ is the gas velocity, and L is the length of the parallel plates, H is the distance that separates the mean gas flow from the chambers. The particle's setting velocity υ_t is given by:

$$\upsilon_t = (\frac{\rho_p g D_p^2}{18\mu}) \tag{1.2}$$

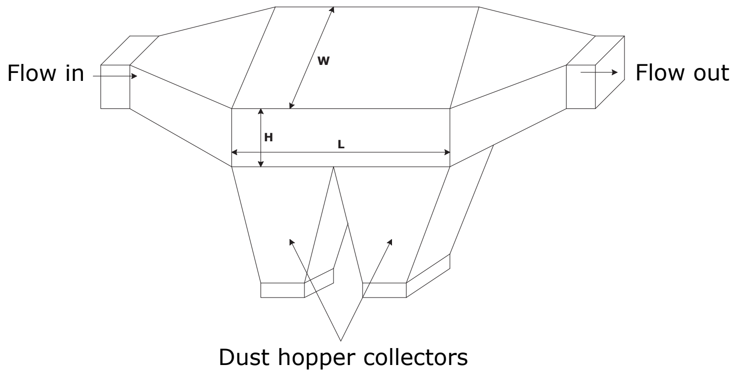

Fig. 1.2 Basic configuration of the gravity settling chambers.

Where g is the gravitational acceleration, ρ_p and D are the density and the diameter of the particle, respectively. The other flow regime is the turbulent flow, where the distribution of the particles are enhanced by the flow motion. In this case, the streamlines of the particles are not uniform. For this flow regime, the collection efficiency is given by:

$$\eta = 1 - exp(-\frac{LW\rho_p D_p^2}{18\mu Q}) \tag{1.3}$$

Where Q is the flow volumetric rate of the stream through the chamber and given by $Q = \overline{u}HW$, and W is the width of the chamber.

Advantages

- Low capital and running cost.
- Absence of moving parts.
- low maintenance cost.
- Low pressure drop.

Disadvantages

- The collection efficiency is relatively low.
- Large physical size.

For further information on the basic principle of the gravity settling chambers, the interested reader can be referred to Green [56] and Flagan et al. [44].

1.3 Wet Scrubbers

Wet collectors or wet scrubbers utilise water wash to the dirty gas flow. The collision between the dust particles and the water droplets results into adequate wetted particles. Therefore, the particles gain weight, and become heavier. The wetted particles are then discharged with the disposal water. Wet scrubbers are grouped into three basic types, namely; gas humidification, gas liquid contact and gas liquid separation.

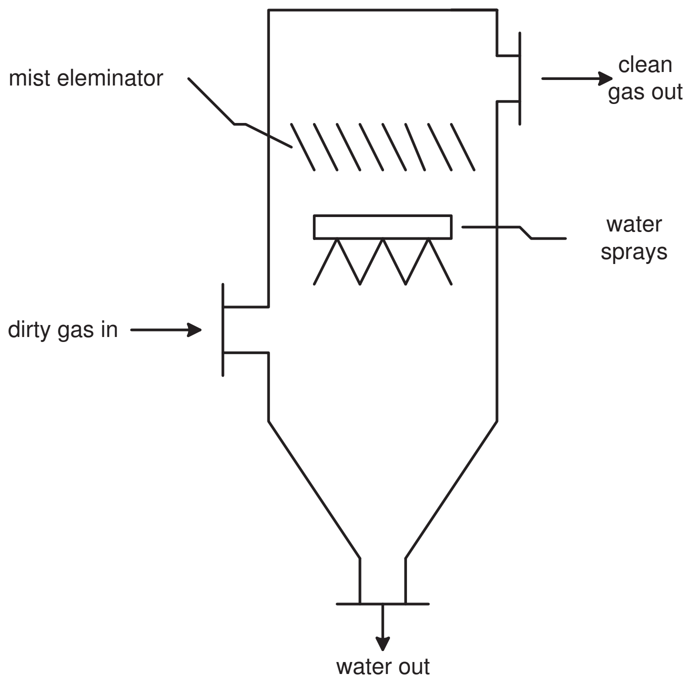

Fig. 1.3 Basic design of the wet scrubber.

Advantages

- No secondary dust sources.
- Relatively small space requirements.
- Ability to collect gases as well as particulates.
- Low capital cost.

Disadvantages

- Corrosion problems more severe than with dry systems.
- Relatively high maintenance costs.
- Product collected wet.

1.4 Electrostatic Precipitators

The electrostatic precipitator is a highly efficient device that removes particles and smokes from a carrier gas by using electrostatic charge. The efficiency of the device arises from the minimum use of the energy applied to filter and it separates the particles from the gas. In electrostatic precipitators, the energy is applied only to the particles. Other dust collector devices apply energy to the flowing gas and particles. Hence, the electrostatic precipitator is very efficient in terms of energy consumption.

The working principle of the electrostatic precipitator is illustrated in Figure. 1.4. The gas containing particles passes through a metal rod that is charged to a very high negative voltage. The particles pick up the negative charge. As the flow moves toward the exit, there are two highly positive charged plates at the sides of the pipe. The function of these positive charged plates is to attract the negatively charged particles. The collecting process ends up by shaking the two plates so that the particles fall off the charged plates down into the containers.

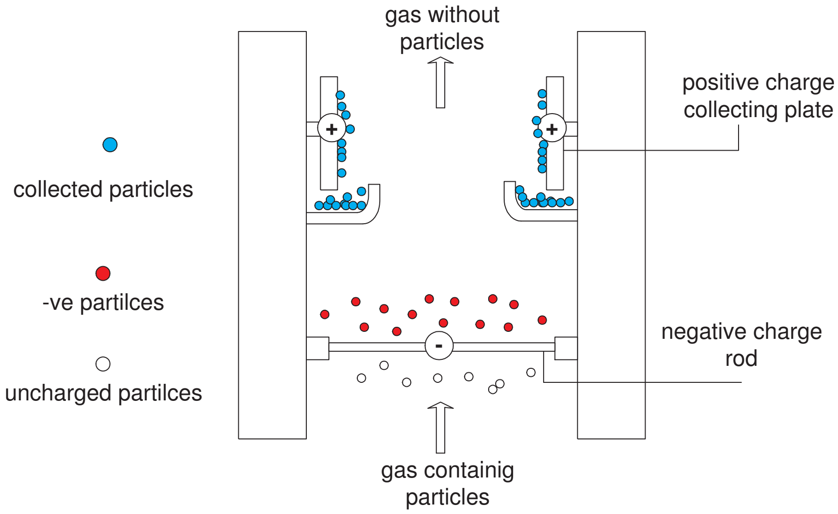

Fig. 1.4 Basic configuration of the electrostatic precipitator.

1.5 Cyclone Separator

The cyclone separator is a fixed and stationary mechanical device that separates the solid particles from a carrier gas stream by employing a centrifugal force. Figure. 1.5 demonstrates the basic configuration of the cyclone body, which consists of four main parts: the tangential inlet, the vortex finder (the gas outlet tube), the cylindrical section (also known as cyclone body) and the conical section. In some cyclone configuration, a hopper section is attached as an additional part to collect the discharged solid particles. The geometry of each basic part is a function of the cyclone body diameter. For instance, the most common types of the cyclone are the high efficiency Stairmand cyclone design and the Lapple cyclone (see Table 1.1). Each part has a relative influence on the flow within the cyclone and its performance.

Table 1.1 Geometry of the most common cyclone design.

cyclone type	**a/D**	**b/D**	**Dx/D**	**S/D**	**h/D**	**H/D**	**Bc/D**
Stairmand cyclone	0.5	0.2	0.5	0.5	1.5	4.0	0.375
Lapple cyclone	0.5	0.25	0.5	0.625	2.0	4.0	0.25

The tangential inlet at the top of the device plays a crucial role on the mechanism and the working principle of the cyclone. The tangential inlet causes the flow to descend in a spiral motion and generates centrifugal force. The centrifugal force deposits the solid parti-

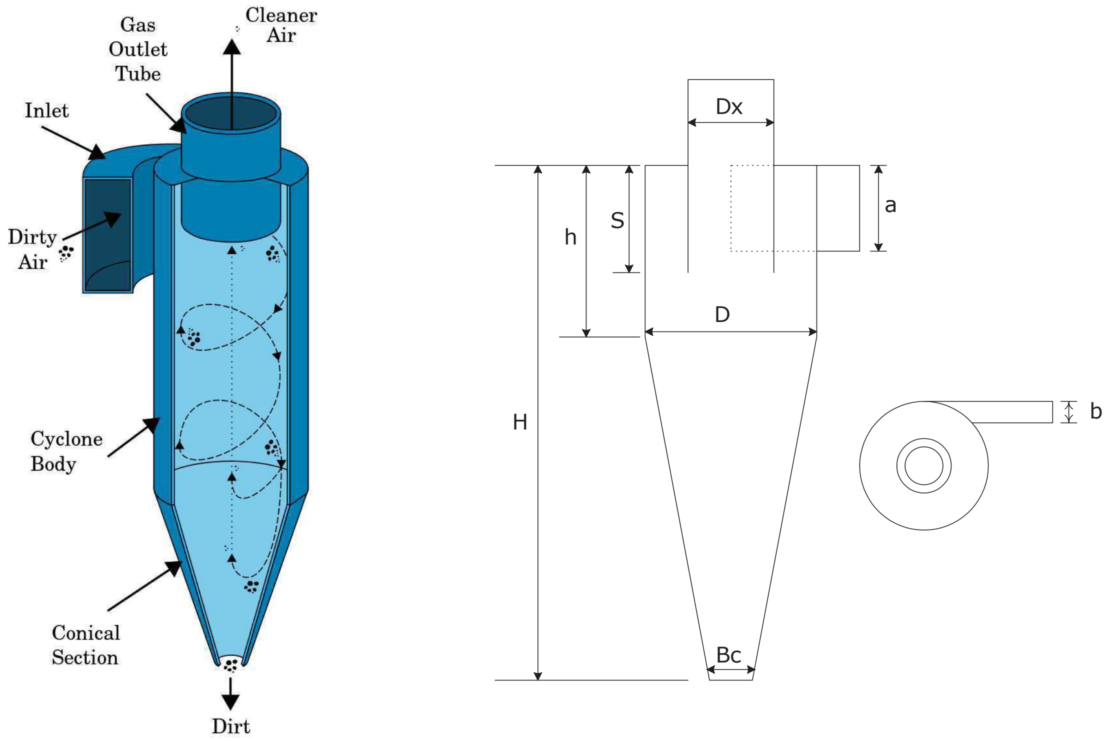

Fig. 1.5 Basic configuration and geometry of the cyclone separator.

cles onto the cyclone body wall and spiral down with the descending flow. At the end of the conical part of the cyclone, the solid particles can either be trapped in a hopper section or discharged out from an apex exit. The gas phase reverses, ascends axially in a spiral motion at the core of the cyclone and exit from the upper exit pipe. The purpose of the conical section is to ensure that the smaller and finer particles are concentrated at the inner wall. The rotational radius reduces and narrows as the gas stream moves down.

The cyclone separator is used widely in many (heavy or light) industrial applications. The widespread use of the cyclone separators is due to several factors. For example, the absence of any moving parts, the low maintenance cost, the low running cost as well as the simple geometry.

During the last century, large number of researches and investigations has been done on the design and the performance of cyclones. These studies vary between experimental, theoretical and computational approach. For instance, in 1952, Kelsall reported a detailed experimental study of the flow pattern and the velocity profile within the cyclones. These experimental results have been used later to test theoretical studies. Between 1960s and 1980s, some of the leading theoretical studies have been introduced to describe velocity distribution alongside with separation efficiency and how it is influenced by some physical quantities. For example, pressure drop, cyclone geometry, particle characteristics and the flow rate. A literature on these different approach studies is presented in chapter (2).

1.6 Scope and Motivation

Recent publications had studied the influence of cyclone separator geometry on the structure of the flow patterns within it. Although, these patterns are not yet fully understood, the basic features of the flow is well known. The recent publications are based on the CFD calculation, which has proven as an effective tool to predict the flow behavior, and at the same time to estimate the performance parameters. The Reynolds Stress Model (RSM) and the Large Eddy Simulation (LES) are the commonly used approaches to simulation flow within cyclone separators. The popularity of these approaches is due to their ability to predict the flow behavior of anisotropic turbulence nature.

It is well known that the conventional Eddy Viscosity Models (EVMs) are developed based on the Boussinesq hypothesis, which assumes the turbulent viscosity as an isotropic scalar. Consequently, accurate prediction of the flow within cyclones is considered as a formidable task for the EVMs. This is unfortunate, as the robustness and computational cost of the EVMs are superior to RSM as well as the LES. In spite the exponential growth of computing power over the last decade, the LES and the RSM are still impracticable for complex and large applications. Therefore, the challenge and the motivation of this work is to modify the EVM in order to cope with the streamline curvature and the swirling flow behavior.

1.7 Aims and Objectives

The main objectives of the study described in this thesis are as follows:

- Implementation of the new sensitization of EVMs to rotation and curvature developed by Spalart–Shur and that developed by Smirnov and Menter.
- Simplify the rotation correction function further and apply it in the SST model developed by Smirnov and Menter.
- Validate the proposed model by performing an axisymmetric 2D simulation of a flow in a confined cylinder with a rotating led. Then, different numerical discretization schemes are tested to examine the accuracy and stability of the numerical computations. The purpose of this case study is to manifest the ability of the model to capture the swirling flow behaviour.
- The model is validated and compared with other models in a simple benchmark problem of a flow in a channel with a U-duct.
- Apply all the versions of the sensitized EVMs to predict the swirling flow in cyclone.

1.8 Thesis Outline

The outline of the thesis is as follows. A brief review of previous studies on cyclone was given in chapter 2. This includes theoretical, experimental and computational studies. Chapter 3, describes the governing equations and the turbulence modeling that is based on Reynolds decomposition of the Navier-Stokes equations. These are followed by a detailed description of the finite volume discretisation used to approximate the governing equations. Chapter 5 gives a brief introduction to the swirling flow inside cyclones. Physical and analytical description of the vortex pattern is revisited. An explanation of the numerical implementation of the proposed approach is given in chapter 6. The results of the computational work are presented in chapter 7. First, a u-duct problem is utilized for verification and validation studies. Then, a Stairmand cyclone model is numerically investigated to demonstrate the capabilities of the proposed formulation in a swirling flow regime. The conclusion is drawn in Chapter 8.

Chapter 2

Review of Previous Studies on Cyclone

The first invention of the gas cyclone (which was known as a dust-collector) was granted to John M. Finch back in 1885 [42]. Since then, there have been many researches and investigations on the design as well as the performance of the cyclone separators. Even though there are no significant changes in the basic shape and the function of the cyclone, there were some leading attempts aimed at increasing the performance of the device by manipulating some geometrical parameters. For instance, Fig. 2.1 shows the historical trend of the cyclone separator design, starting from the most simple design of low efficiency with no vortex finder, ending with various high efficient designs [48].

The most common geometrical parameters that had been changed over the years include total height, cylinder (barrel) height and cone height (See Table. 2.1). These parameters are the basic configuration of cyclone, which have remained almost unchanged over the years. The size of each parameter has some relative influence on the performance of the device. This fact has led to the emergence of different cyclone designs, each of these designs has different performance specifications. Further information about the relationship between the cyclone geometry and the performance can be found in the optimisation study of Elsayed [36].

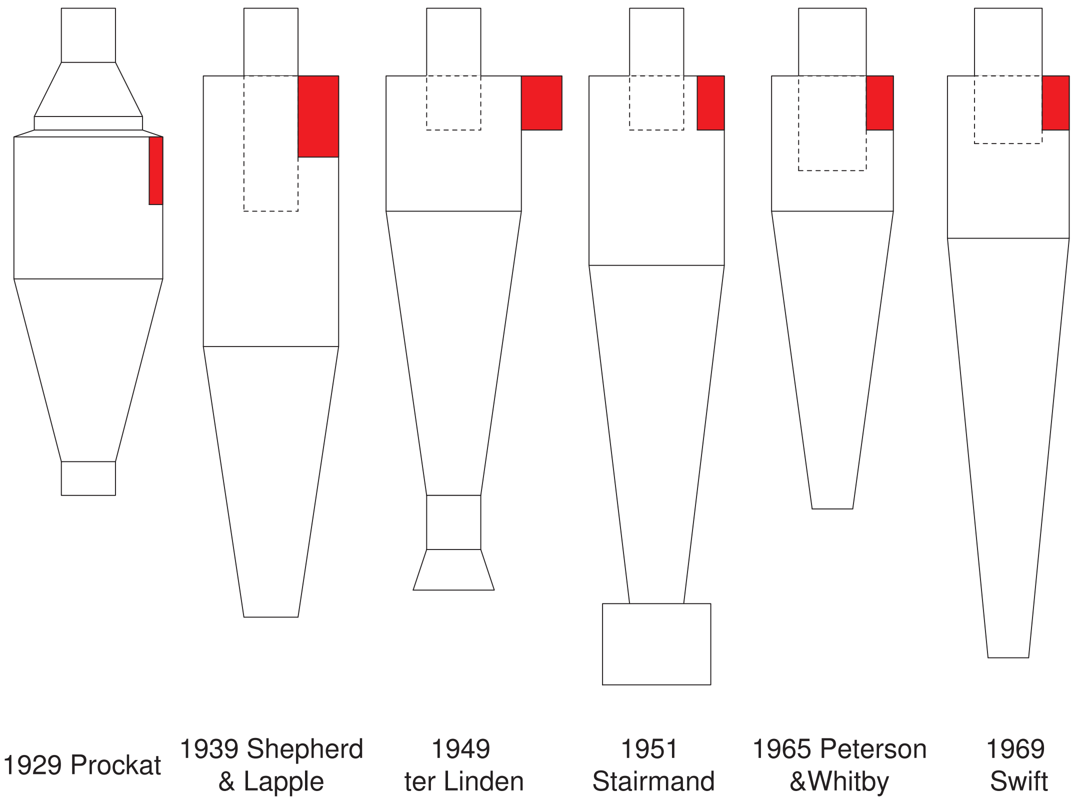

Fig. 2.1 Historical pattern of the cyclone separator design.

Table 2.1 Height of the most common cyclone design.

Author (date)	**Height/Diameter**			
	Efficiency	Cylinder	Cone	Total hight
Prockat (1929)	Low	1	1	2
Shepherd & Lapple (1939)	High	2	2	4
ter Linden (1949)	High	1	2	3
Stairmand (1951)	High	1.5	2.5	4
Peterson & Whitpy (1965)	High	1.33	1.84	3.17
Swift (1969)	High	1.4	2.5	3.9

2.1 Theoretical Studies

Since the first invention of the cyclone device, several approaches and theoretical models have been developed for the calculation and the estimation of the flow pattern within the cyclone and the performance parameters, precisely, the pressure drop and the collection efficiency [2]. The pioneer works of Eugen Feifel, which extended for more than 12 years, had a major impact on the understanding of the flow behavior and the particle motion within the cyclone [67]. Whereas, the most leading studies that focus on the flow pattern and its implications was carried out in 1939 by Shephered and Lapple [113]. They reported that the flow within the cyclone can be classified into two different flow regimes, an outer downward spiral flow and an inner upward spiral flow with higher velocity and smaller diameter. Ten years later, ter Linden [124] investigated experimentally the influence of the cyclone principle dimensions on its performance. Many other researchers proposed different theoretical models. For example, the most resent approaches, including but not limited to, Bose el al. [14], Zhao et al. [139, 140], Elsayed et al. [38] and Karagoz et al. [6, 75]. Guessing the separation efficiency of cyclones implicates the prediction about the behaviour of particles in the separation space. For this purpose, it is very important to understand the velocity distribution of the gas inside cyclones. Some researchers have concentrated on flow pattern as well as separation efficiency while proposing models of cyclones, whereas many have focused only either on flow pattern or on separation efficiency.

2.2 Experimental Studies

The design of cyclone has remained mainly unchanged for almost a century. For the experimental researches, generally, two types of cyclone designs has been used, namely the straight-through cyclone and conventional reverse flow cyclone. As comrade to straight-through cyclone, the most frequently used cyclone is the reverse flow type. The main objectives of these experimental studies were to calculate the performance and/or obtain the flow pattern inside the cyclone. The vast majority of these experiments used one of the following methods: either the particle image velocimetry method (PIV) or the laser doppler anemometry method (LDA). Some of these studies were applied on a specific cyclone model and aimed to measure the pressure drop and the collection efficiency without referring to the flow pattern. For example, Dirgo and Leith experimentally tested the performance of Stairmand high-efficiency cyclone by measuring the collection efficiency and the pressure drop over a range of air flows [31]. The results were compared with some theoretical predictions, and it was found that a modified version of Barth's theory and the Leith-Licht theory were closest to experimental results.

The LDA method was adapted by several studies. For example, the most recent studies are those of Hokestra et al. [64], Gorton et al. [55], Obermair et al. obermair2003 and Solero and Coghe [117]. The experimental work of Hokestra targeted a reverse-flow gas cyclone to investigate the ability of different Computational Fluid Dynamics (CFD) approaches to predict the cyclone flow field. By comparing the CFD results with the LDA measurements, Hokestra supported the notion that the Eddy Viscosity Models (EVMs) are not capable to capture the swirling flow inside cyclones. Shortly after that, Gorton investigate the flow field of both the gas phase and the solid-particles.

2.3 Numerical Studies

Computational Fluid Dynamics (CFD) is one of the most powerful techniques used to solve a vast array of fluid flow problems. The recent evolution in computer technology has resulted in more effective performance and high capacity computers. This evolution has a tremendous impact on the CFD community towards the calculation of complicated flow fields with a relative ease. By means of CFD, the fluid flow and the related physical phenomena can be described by a set of partial differential equations, which is very difficult to solve analytically. These equations can be solved numerically by utilising a discretisation method which approximates the differential equations by a system of algebraic equations, and then can be solved computationally. A more general introduction to the basics and principle of the CFD technique is given by Anderson [4] and Ferziger [41].

One of the earliest attempts to model the gas flow and the particle motion occurring in cyclone separators with the aid of the CFD technique was carried out by Boysan in 1982 [16]. In order to reduce the computational effort which arises from the complex flow feature in cyclones, the gas flow fields was solved in axisymmetric Eulerian framework. In addition, a closure model was employed to relate the Reynolds stress components to the time averaged quantities. A remarkable conclusion was provided by Boysan. He found that the conventional eddy viscosity turbulence model namely ($k-\varepsilon$ model) is incapable of capturing the complex features of the highly swirling flow.

In 1989, Bernard et al. adapted the model of Boysan to simulate the flow field and estimated the pressure drop of Lappel cyclone model when it operates at high temperatures [11]. The algebraic stress model (ASM) was implemented in this study, rather than the full Reynolds stress turbulence model (RSM). In 1996, Hoffmann et. al compared the model of Boysan with the (ASM) when they studied the effect of the hopper section attached to dust outlet on the flow pattern [66]. Similarly, the measurements of Zhou et al.. implemented the standard ($k-\varepsilon$) model to perform axisymmetric simulations. The obtained pressure drop and the flow pattern were validated with the Laser Doppler Velocimetry (LDV) data [141]. Other axisymmetric simulation that employed a modified ($k-\varepsilon$) model to predict the flow pattern in hydrocyclone was implemented by Dyakowski and Williams [35].

The exponential growth of computing power over the last decade allows the researchers (from academia and industry) to perform a full three dimensional simulation of the cyclone separators. For instance, in 1996, Boysan and Griffiths performed a 3D simulation to study the performance of three types of small cyclone samplers and compared the CFD results with experimental data [57]. They solved the RANS equations by using the Re-Normalisation Group (RNG $k-\varepsilon$) model. The CFD results were in a good agreement with the experimental data.

Several CFD calculations of cyclone flow published more recently employed the full RSM turbulence model. For example, Gimbun et al. studied the influence of the temperature and the inlet velocity on cyclone pressure drop and compared the CFD predictions with experimental data and with different empirical models [52]. The results showed that RSM is superior to (RNG $k-\varepsilon$) but with notifiable more computational time. In 2006, Shalaby et. al performed a comparison study between three different approaches to numerically predict the flow within cyclones. Again, the study showed that standard ($k-\varepsilon$) model is incapable to predict the flow phenomena inside cyclones. Also it showed that the Large Eddy Simulation (LES) is more informative and more accurate than RSM, but it requires more CPU times and higher computer capacity [112]. In a similar way, Gronald et. al examined three different approaches to simulate turbulent swirling flow in a single phase cyclone. Two approaches were based on finite volume discretisation namely (RANS and LES) and one LES approach based on a lattice-Boltzmann discretisation [58]. The RANS approach coupled with RSM turbulence model performed on a coarse grid and the predictions provided reasonable results with limited computational effort. On the other hand, the LES approaches are coupled to a standard Smagorinsky subgrid-scale model (SGS) with finer grid resolution and hence more computational effort. The tangential velocity was excellently predicted by the LES approaches, while it was underestimated by the RANS approach.

More recent studies put an effort on eddy-viscosity models sensitized to rotational and curvature effects. Although computationally more expensive approaches: (RSM) and (LES) have demonstrated good capabilities to deal with such flows, these techniques are very often impractical for complex design studies where computational speed and robustness are key factors. These factors are the main focus of this thesis.

Chapter 3

Mathematical Models

3.1 Theoretical Background

Recently, many researches have been conducted to investigate and predict the flow within the cyclone separator devices. The results of these attempts showed that the turbulence modeling of the continuous phase flow plays a crucial role in the accuracy of the numerical solution, which in turn leads to accurate calculation of the cyclone efficiency parameters. The cyclone separators operate normally at a range of $Re = 10^5$ to 10^6, such a flow is considered to be fully turbulent. The fundamental physics of the fluid flow is described and governed mathematically by Navier-Stokes Equation, namely, the continuity equation and the mass conservation equation. For transient incompressible flow, these equations can be written as follows;

$$\frac{\partial u_i}{\partial x_i} = 0 \tag{3.1}$$

$$\frac{\partial u_i}{\partial t} + \frac{\partial u_i u_j}{\partial x_j} = -\frac{1}{\rho}\frac{\partial p}{\partial x_i} + \frac{\mu}{\rho}\frac{\partial^2 u_i}{\partial x_j\, \partial x_j} \tag{3.2}$$

3.2 Main Characteristics of Turbulent Flow

The turbulent phenomena is one of the major unsolved problem in classical physics. It exits in nature from microscopic to macroscopic scales as well as in many industrial devices. For example, it can be found in the interior of biological cells, the circulatory and respiratory systems of living creatures, in some mechanical apparatuses, in atmospheres and oceans. And even its occurrence is somehow old as the universe. According to recent studies, the present form of the universe is a consequence of the turbulent following the Big Bang [88]. This ubiquity of turbulence urged many intellectuals to try to describe and explain this phenomenon. The earliest explanation that lid to a close understanding of the turbulent was the one that introduced by the great philosopher Leonardo da Vinci [27], he said:

> *"Observe the motion of the surface of the water, which resembles that of hair, which has two motions, of which one is caused by the weight of the hair, the other by the direction of the curls; thus the water has eddying motions, one part of which is due to the principal current, the other to random and reverse motion."*

Fig. 3.1 Leonardo da Vinci's observation of turbulent flow [27].

Figure 3.1 shows the da Vinci's sketch to visualize the water flow from a slot and flows into a pool. This sketch was drawn in the early sixteenth century, and it was the first use of visualization technique as a scientific tool to describe turbulent [96]. Also he had described the structure of the eddies in the turbulent flow in a remarkable words, he wrote:

> *"The smallest eddies are almost numberless, and large things are rotated only by large eddies and not by small ones, and small things are turned by small eddies and large."*

Although the observations of da Vinci were very enlightened, they did not give a comprehensive definition of turbulence. Since then, many scientists and physicists tried to provide a clear and thorough definition of turbulence. One of the best known of these is due to Richardson [107], in 1922 he wrote:

> *"Big whorls have little whorls, which feed on their velocity; And little whorls have lesser whorls, And so on to viscosity."*

For almost six centuries after the observations of da Vinci, many attempts have been drafted to offer a precise definition of turbulent flow. None of these definitions could successfully anticipate when turbulence will or will not occur under specific flow conditions. The difficulty of giving a comprehensive and conclusive definition of turbulent flow is due to the chaotic and irregularity nature of the turbulence itself. However, the fluid dynamics field, as it is known today, is based on the Navier-Stokes equations (3.1) and (3.2). It is universally believed that the physics of all fluid flows, including turbulence ones, can be described by these equations. The main dilemma is the **Navier-Stokes existence and smoothness problem**. Where for three dimensional system of equations, and at a given initial conditions, a smooth solutions of Navier-Stokes is not always exist.

In 1883, Osborne Reynolds [104] proposed one of the most groundbreaking report, he systematically investigated the transition of fluid flow in a pipe from laminar to turbulent. Figure. 3.2 illustrates the classical experiment that he performed. He first started with a tank filed with water to a constant height. A tube is attached to oneside of the tank at the bottom. One end of the tube has a flared entry (Bell mouth intake) to prevent any disturbance when the fluid passing through the tube. The other downstream end was initially closed by a valve.

In order to visually observe the nature of the flow, he injected a color dye at the entrance of the attached tube. The stop valve was gradually opened, thus increasing the velocity of the fluid and the colored liquid flowed, as shown in Fig. 3.3. He observed that at a certain velocity, the flow will transient from laminar to turbulent. By doing the experiment with different fluids in different tubes, the critical velocity varies from fluid to fluid and also varies according to the tube diameter. Finally, he concluded that the critical velocity at which the flow transient from laminar to turbulent depends upon the pipe diameter and the fluid properties (density and viscosity). The profound findings of this experiment led

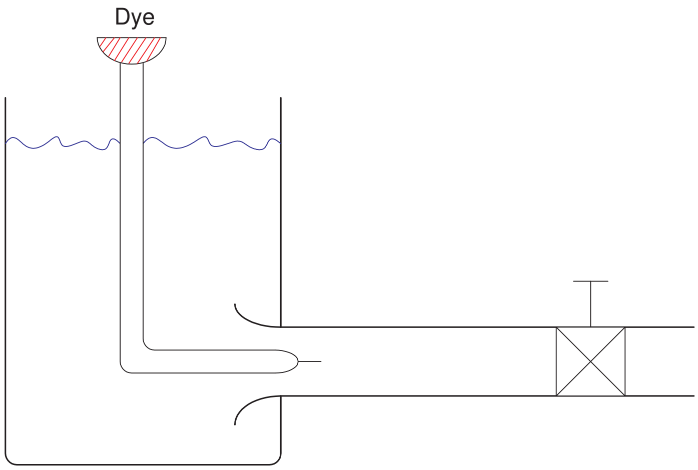

Fig. 3.2 The classical experiment of Reynolds.

to identification of a criterion dimensionless number, which is known today as *Reynolds number*. This number is defined as the ratio of inertial forces to viscous forces, and denoted *Re*:

$$Re = \frac{\rho U L}{\mu} \tag{3.3}$$

where ρ and μ are the fluid physical properties, density and viscosity respectively, U is the inlet velocity and L is the length scale and in this case it is the pipe diameter.

After the work of Reynolds, the flow behavior can be characterized according to the flow Re number. For example, at a relative low Re (less than 2000), case (a) in Fig. 3.3, the flow is more likely to behave in a uniform and a smooth manner, which is called a laminar flow regime. As the Re increases, the flow streamlines start to wave as indicated

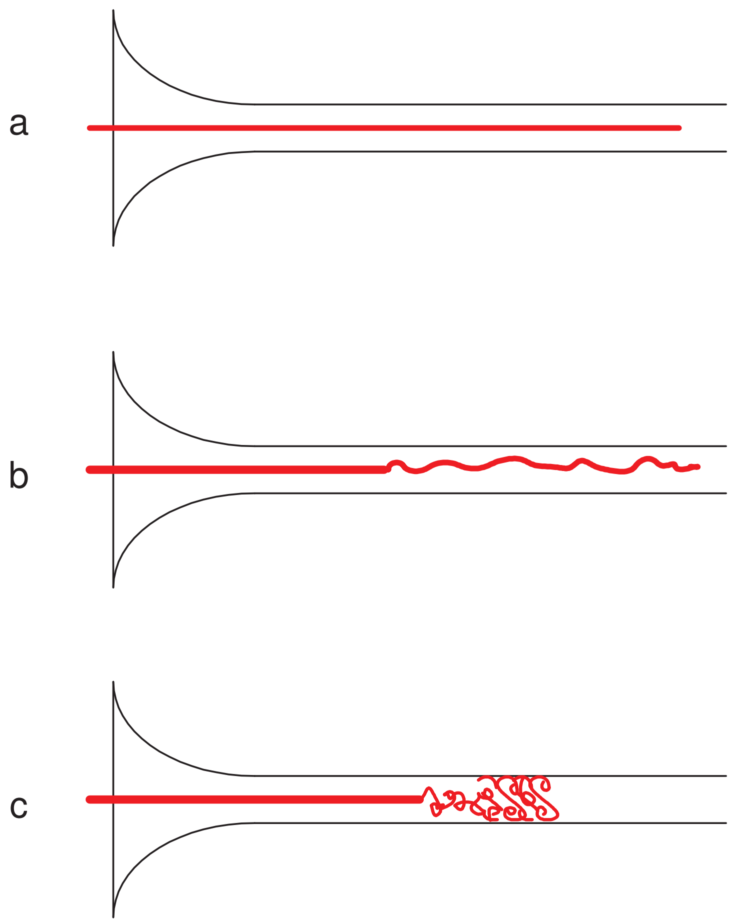

Fig. 3.3 Reynolds observations; a) flow in laminar state, b) early transitional, c) flow transits to turbulence.

in Fig. 3.3(b). At this stage *Re* lies between 2000 and 3200 and the flow is identified as a transient from laminar to turbulent, but still considered a laminar flow as the streamlines are clearly identifiable. Figure 3.3(c) shows the fully turbulent regime, where the value of *Re* exceeds 3200. At this regime, the flow is extremely chaotic and irregular, and the motion of fluid particles is not uniform. To relate this number in the Navier-Stokes equations, the equation (3.2) can be rewritten as follows:

$$\frac{\partial u_i}{\partial t} + \frac{\partial u_i u_j}{\partial x_j} = -\frac{1}{\rho}\frac{\partial p}{\partial x_i} + \frac{1}{Re}\frac{\partial^2 u_i}{\partial x_j\,\partial x_j} \tag{3.4}$$

for high *Re* the nonlinear term $\frac{\partial u_i u_j}{\partial x_j}$ will be more dominant, which in turns makes the equation very difficult to be solved. Finally, the characteristics of turbulent can be summarized as follows:

- **Irregularity**
  the turbulent by its nature is irregular and complex, not predicted and not easy to describe.

- **Three dimensional**
  there is always a three dimensional element to the flow regime. Even in the presence of an apparently strong directional flow, there is always secondary flow mechanisms in place.

- **Diffusivity**
  there is usually a rapid mixing of momentum, heat and mass.

- **Dissipation**
  kinetic energy of the associated turbulent eddies are readily dissipated into heat under the influence of fluid viscosity. The energy required to maintain the turbulence itself therefore comes from the mean flow via the interaction of shear stresses and velocity gradients.

3.3 Turbulent Flow Simulation

The fluctuation of the mean velocity gradients in the flow field forms the initial turbulence eddies. These eddies create smaller levels of fluctuations, and hence generate an even smaller eddies. This process continues to a scale where the eddies size is sufficiently small and the corresponding velocity gradients are sufficiently large. At this infinite small scale, turbulence energy is dissipated by the effect of the viscosity (See Fig. 3.4).

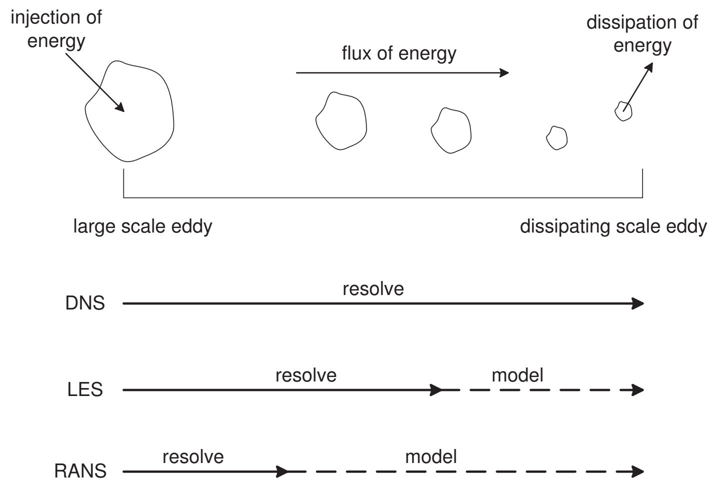

Fig. 3.4 Production and dissipation of turbulence.

In CFD (computational fluid dynamics) three main approaches are developed over the years to solve and predict the turbulent flows computationally. The first method is the Direct Numerical Simulation (DNS), where Navier-Stokes equations are directly solved. The second method resolves the large eddies and models the smaller ones, which is known as the Large Eddy Simulation (LES). The LES is less computational demanding than the DNS. The third approach is based on the Reynolds-averaged Navier-Stokes equations. The Reynolds stresses obtained from the averaging process (as will be discussed shortly) are modeled by a constitutive relationship with the mean flow. These three methods will be discussed in details in the following sections.

Most of the fluid flows found around the glob are turbulent in their nature and are very special in the sense that they have special characteristics. These characteristics make the turbulent flow extremely difficult to be described mathematically; and hence to be solved in CFD tools. This difficulty arises from several factors. For instance, the turbulent flow is not one dimensional or two dimensional, as expected in laminar case, rather it is inherently three dimensional and inherently unsteady. This means that it is highly fluctuating and very rapid in time. The rapidness fluctuation in time leads to select very small time step Δt in order to capture these fluctuations. In addition, the rapidness fluctuation in spacial dimension leads to select a very small grid spacing Δx to capture and measure these fluctuation.

In the mid-1890s O. Reynolds has proposed a decomposition of the velocity at a particular point. The primitive variable of interest is decomposed into a time averaged quantity and an instantaneous quantity. By using the decomposition technique, Reynolds came up with an averaging approach that is well known in the CFD community as the Reynolds Averaged Navier-Stokes Equation RANS. The RANS approach well be discussed in the following section.

3.3.1 Reynolds-Averaged Navier-Stokes Equation

The Reynolds-Averaged Navier-Stokes Equations (RANS) are the time-averaged of the equations of motion for fluid flow. This set of equations, as O. Reynolds firstly proposed [105], is nowadays the backbone of many turbulence modeling. To understand the concept of the RANS approach, let u be the x-component of the velocity and it is a function of time $u(t)$ as shown in Figure 3.5.

The averaging method decomposes the velocity in the example above into a fluctuating quantity and a mean value at a fixed point in space. So that the velocity is written as:

$$u(t) = \overline{u} + u'(t) \tag{3.5}$$

where $\overline{u}$ is the time average quantity which is independent of time, and $u'(t)$ is the fluctuation quantity. The mean value is averaged over a time span that is large enough to be independent

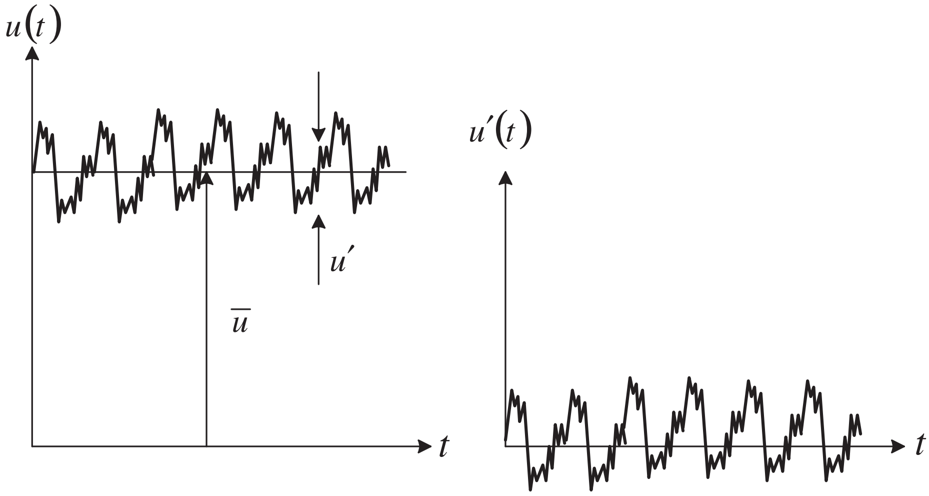

Fig. 3.5 Turbulent velocity fluctuation as a function of time.

of time, and presented as follows:

$$\overline{u} = \frac{1}{T}\int_a^b u(t)\,\mathrm{d}t \tag{3.6}$$

Before proceeding, a brief of some properties of averaging notation shall be given:

summation of two time averaged quantities

$$(\overline{u+g}) = \overline{u} + \overline{g} \tag{3.7}$$

product of scalar by time averaged quantity

$$(\overline{s.u}) = s.\overline{u} \tag{3.8}$$

production of two time averaged quantities

$$(\overline{u.g}) = \overline{u}.\overline{g} + \overline{u'g'} \tag{3.9}$$

The fluctuation term $\overline{u'g'}$ arises from the product of two time averaging quantities can be zero, negative or positive value. The quantity $\overline{u'g'}$ is zero occurs only and only if the fluctuations arising out of u are not related and independent of the fluctuations arising out of g. In case of turbulent, the product of any two fluctuating quantities can never be zero. This is because the fluctuating parameters of the velocity components are highly dependent and related to each other. The strong relation of the fluctuating parameters will be discussed shortly when we decompose the Navier-Stokes equation. In the case of incompressible flow, the continuity equation can be written as:

$$\frac{\partial u}{\partial x}+\frac{\partial v}{\partial y}+\frac{\partial w}{\partial z}=0 \tag{3.10}$$

By Applying the time averaging for both LHS and RHS:

$$\overline{\frac{\partial u}{\partial x}+\frac{\partial v}{\partial y}+\frac{\partial w}{\partial z}}=\overline{0} \tag{3.11}$$

Applying the summation of time averaging quantities role will result in the last form:

$$\frac{\partial \overline{u}}{\partial x}+\frac{\partial \overline{v}}{\partial y}+\frac{\partial \overline{w}}{\partial z}=0 \tag{3.12}$$

If the flow is steady, the quantities $\overline{u}$, $\overline{v}$ and $\overline{w}$ will not fluctuate in time and that is the definition of steady flow in turbulent quantities. Therefore, if the flow is steady in the turbulent flow sense, there is no need to solve for fluctuating parameters u', v', and w', which makes it computationally easier. The x-component of the momentum equation is given by:

$$\frac{\partial u_i}{\partial t}+\frac{\partial}{\partial x}(u^2)+\frac{\partial}{\partial y}(uv)+\frac{\partial}{\partial z}(uw)=-\frac{1}{\rho}\frac{\partial p}{\partial x_i}+\nu\nabla^2 u_i \tag{3.13}$$

Equation (3.13) is expressed in terms of the instantaneous quantities u, v, w and p each of which is fluctuating, and hence can be decomposed into $\overline{u}+u'$, $\overline{v}+v'$, $\overline{w}+w'$ and $\overline{p}+p'$. The time averaging of the x-momentum equation is written as:

$$\frac{\partial \overline{u}}{t}+\frac{\partial}{\partial x}(\overline{u^2})+\frac{\partial}{\partial y}(\overline{uv})+\frac{\partial}{\partial z}(\overline{uw})=-\frac{1}{\rho}\frac{\partial \overline{p}}{\partial x}+\nu(\frac{\partial^2 \overline{u}}{\partial x^2}+\frac{\partial^2 \overline{u}}{\partial y^2}+\frac{\partial^2 \overline{u}}{\partial z^2}) \tag{3.14}$$

It can be seen that the LHS of the above equation contains production terms of two time averaging quantities. Applying role (3.9) to the second, the third and the fourth term of equation (3.14) will produce new terms as follows:

$$\frac{\partial}{\partial x}(\overline{u^2}) = \frac{\partial}{\partial x}(\overline{u}^2 + \overline{u'u'}) \tag{3.15}$$

$$\frac{\partial}{\partial y}(\overline{uv}) = \frac{\partial}{\partial y}(\overline{u}\,\overline{v} + \overline{u'v'}) \tag{3.16}$$

$$\frac{\partial}{\partial z}(\overline{uw}) = \frac{\partial}{\partial z}(\overline{u}\,\overline{w} + \overline{u'w'}) \tag{3.17}$$

The only difficulty arises from the time averaging process is the appearance of the extra terms (the product of the two fluctuating quantities). Substituting equations (3.15), (3.16) and (3.17) into equation (3.14) and moving the fluctuating terms to the RHS will form the time averaging of the x-component of the momentum equation:

$$\begin{aligned} \frac{\partial \overline{u}}{\partial t} + \frac{\partial}{\partial x}(\overline{u}^2) + \frac{\partial}{\partial y}(\overline{u}\,\overline{v}) + \frac{\partial}{\partial z}(\overline{u}\,\overline{w}) \quad = \quad & -\frac{1}{\rho}\frac{\partial \overline{p}}{\partial x} + \nu(\frac{\partial^2 \overline{u}}{\partial x^2} + \frac{\partial^2 \overline{u}}{\partial y^2} + \frac{\partial^2 \overline{u}}{\partial z^2}) \\ & -\frac{\partial}{\partial x}(\overline{u'u'}) - \frac{\partial}{\partial y}(\overline{u'v'}) - \frac{\partial}{\partial z}(\overline{u'w'}) \end{aligned} \tag{3.18}$$

In a similar fashion, the other two components of the momentum equations are derived. The decomposition of the continuity and momentum equations form the full set of the RANS system. By applying the Einstein summation convention, equations (3.18) can be rewritten in one a simple equation as follows:

$$\rho\frac{\partial \overline{u_i}}{\partial t} + \rho\frac{\partial \overline{u_i u_j}}{\partial x_j} = -\frac{\partial \overline{p}}{\partial x_i} + \frac{\partial}{\partial x_j}\left(2\mu S_{ij} - \rho\overline{u_i' u_j'}\right) \tag{3.19}$$

where the term S_{ij} is the time averaged quantity of the strain-rate tensor:

$$S_{ij} = \frac{1}{2}\left(\frac{\partial \overline{u_i}}{\partial x_j} + \frac{\partial \overline{u_j}}{\partial x_i}\right) \tag{3.20}$$

The appearance of the additional term ($\tau_{ij} = -\rho\overline{u_i' u_j'}$) is known as Reynolds stress tensor. Figure. 3.6 illustrates the Reynolds stresses acting on a control volume. The normal stresses associated with the turbulence fluctuations ($\rho\tau'_{xx}$, $\rho\tau'_{yy}$ and $\rho'\tau_{zz}$), are the perpendicular momentum fluxes per unit area across the zy, zx and xy planes respectively. While the turbulent shear stresses are given by ($\rho\tau'_{yx}$, $\rho\tau'_{zx}$ and $\rho\tau'_{yz}$). The system of the equations has to be closed in order to get a solution for the mathematical problem. This can be achieved by postulating a specific term of τ_{ij} in a framework of designing a turbulence model.

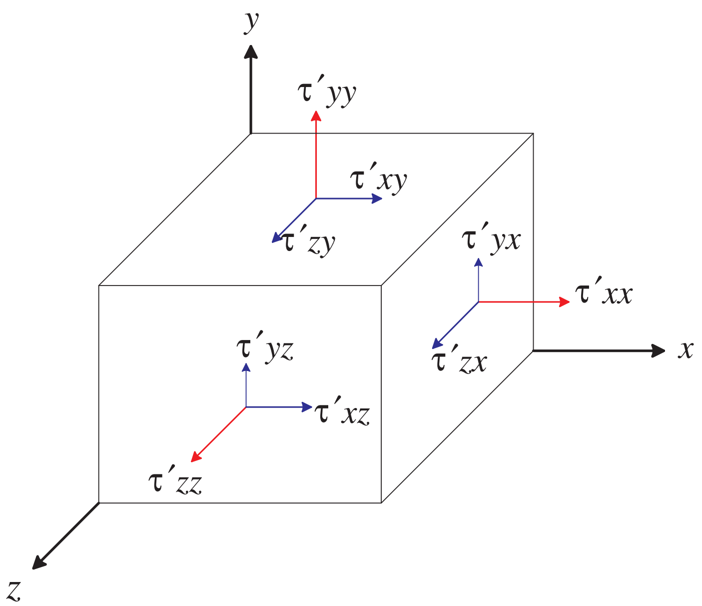

Fig. 3.6 Reynolds stresses arise from decomposing Navier-Stokes equations.

3.3.2 Closure Problem and Turbulence Modeling

The right hand side of equation (3.19) is actually the sum of the laminar and the turbulent stresses, which can rewritten as follows:

$$\rho\frac{\partial\overline{u_i}}{\partial t}+\rho\frac{\partial\overline{u_i}\overline{u_j}}{\partial x_j}=\underbrace{-\frac{\partial\overline{p}}{\partial x_i}+\mu\left(\frac{\partial\overline{u_i}}{\partial x_j}+\frac{\partial\overline{u_j}}{\partial x_i}\right)}_{\text{laminar stresses}}+\underbrace{\frac{\partial}{\partial x}\left(-\rho\overline{u'_iu'_j}\right)}_{\text{turbulent stresses}} \tag{3.21}$$

In case of laminar flow, the last term of equation (3.21) can be neglected. Therefore, the solution of the governing equation is not complicated. The turbulent flow, on the other hand, contains the Reynolds stresses term that presents a significant difficulty in solving the equation. The direct numerical solution of the Navier-Stokes equations without using any turbulence model is known as the Direct Numerical simulation (DNS). Despite the exponential growth of modern computing power, the DNS is still limited to simple low Reynolds number cases. The limitations are due to the grid resolution and the CPU time. For a sufficient DNS simulation, the number of grid points is needed to be scaled as $Re^{2.25}$, and the computational time as Re^3. Consequently, the DNS in not practical for the Re numbers encountered in most industrial applications.

The first level of approximating turbulence is presented by the Large Eddy Simulation (LES) technique. The foundation of the LES is based on the implication of Kolmogorov's theory [12]. The turbulent energy is transported from the larger to the smaller eddies. At the large scale, the motion of fluid particles are inhomogeneous and anisotropic. These characteristics are lost as the energy cascaded, which in turn lead to a universal characteristic of the eddies at smaller scales. The concept of the LES approach is to resolve the large eddies accurately, and implement a relative simple sub-grid scale model (SGS) to approximate the small scale eddies. Therefore, the LES is more feasible than DNS for high Re flows because the grid points it requires is significantly less than the DNS. However, the LES remains computationally intensive and thus still far from being an engineering approach.

The other level of approximating turbulence is the RANS modeling technique. The derivation of the RANS approach is presented in section (3.3.1). The additional net surface forces that appear in the turbulent stress term of equation (3.21), are the molecular momentum transport associated with the turbulence fluctuations. The laminar stresses are related to the laminar viscosity, while the turbulent stresses are related to the fluctuating components of the velocity. The erratic behavior of these fluctuating components with time are very complex to be described in an exact mathematical formula. What make matters worse, is that there are no explicit governing differential equations of these additional unknowns. Therefore, modeling the Reynolds stresses provide an alternative approach to close and hence solves the RANS equations. The ground bases of the turbulence modeling is to relate the

Reynolds stresses to the mean flow velocity gradient. For example, in 1877 Boussinesq [15] assumed that the stresses caused by the turbulent eddies can be modeled by using a an eddy viscosity μ_t [134].

$$\tau_{ij} = 2\mu_t S_{ij} - \frac{2}{3}\rho k \delta_{ij} \tag{3.22}$$

The turbulence models are classified according to the number of the additional transport equations that need to be solved. Table. 3.1 listed the commonly used models to close and solve the RANS equations, which include: the first order eddy viscosity models, and the second order Reynolds stress transport model.

Table 3.1 Turbulence modeling of RANS equations.

No. of extra equations	**name of the model**
Zero equation	mixing length.
One equation	Spalart and Allmaras.
Two equations	Standard $k-\varepsilon$ model RNG $k-\varepsilon$ model Realizable $k-\varepsilon$ model $k-\omega$ model.
Seven equations	Reynolds stress model.

3.3.2.1 $k-\varepsilon$ model

The $k-\varepsilon$ turbulence model is by far the most prominent and widely used two equations model. It has been improved and tested over the years. For example, the earliest improvements are those of Chou [22], Davydov [29] and Harlow and Nakayama [60]. The standard version of the $k-\varepsilon$ model is named and widely spread after the development of Launder and Sharma [80]. The kinematic eddy viscosity ν_t, the turbulence kinetic energy k and the turbulence dissipation rate ε of the standard $k-\varepsilon$ model are respectively specified as follows:

$$\nu t = C_\mu \frac{k^2}{\varepsilon} \tag{3.23}$$

$$\frac{\partial k}{\partial t} + \overline{u_j}\frac{\partial k}{\partial x_j} = \frac{\partial}{\partial x_i}\left[\frac{\nu_t}{\sigma_k}\frac{\partial k}{\partial x_i}\right] - \varepsilon + \tau_{ij}\frac{\partial \overline{u}_i}{\partial x_j} \tag{3.24}$$

$$\frac{\partial \varepsilon}{\partial t}+\overline{u_j}\frac{\partial \varepsilon}{\partial x_j}=\frac{\partial}{\partial x_i}\left[\frac{\nu_t}{\sigma_\varepsilon}\frac{\partial \varepsilon}{\partial x_i}\right]+C_{\varepsilon 1}\frac{\varepsilon}{k}\tau_{ij}\frac{\partial \overline{u}_i}{\partial x_j}-C_{\varepsilon 2}\frac{\varepsilon^2}{k} \tag{3.25}$$

where C_μ, $C_{\varepsilon 1}$, and $C_{\varepsilon 2}$ are standard model constants as fitted with benchmark experiments, and σ_k and σ_ε are the Prandtl numbers of k and ε respectively.

$$C_\mu = 0.09, \qquad C_{\varepsilon 1} = 1.44, \qquad C_{\varepsilon 2} = 1.92, \qquad \sigma_k = 1, \qquad \sigma_\varepsilon = 1.3$$

The Reynolds stresses are then calculated as follows:

$$-\rho\overline{u_i' u_j'} = -\frac{2\rho}{3}k\delta_y+\mu_t\left(\frac{\partial \overline{u_i}}{\partial x_j}\frac{\partial \overline{u_j}}{\partial x_i}\right) \tag{3.26}$$

3.3.2.2 The RNG $k-\varepsilon$ Turbulence model

The RNG $k-\varepsilon$ model, which is based on the Re-Normalisation Group theory, is a modified version of $k-\varepsilon$ model developed by Yakhot et al. [136]. The purpose of the modification is to allow the model to capture swirl flow regime and rotational system by modifying the coefficient $C_{\varepsilon 2}$. The mathematical formula of the RNG $k-\varepsilon$ turbulence model is similar to that of the $k-\varepsilon$ equations, but it includes additional terms in the ε equation to account for the interaction between turbulence dissipation and the mean shear.

$$\frac{\partial k}{\partial t}+\overline{u_j}\frac{\partial k}{\partial x_j}=\nu_t\left(S_{ij}\right)\frac{\partial \overline{u_i}}{\partial x_j}+\frac{\partial}{\partial x_i}\left(a_k\left(\nu+C_\mu\frac{k^2}{\varepsilon}\right)\frac{\partial k}{\partial x_i}\right)-\varepsilon \tag{3.27}$$

$$\frac{\partial \varepsilon}{\partial t}+\overline{u_j}\frac{\partial \varepsilon}{\partial x_j}=C_{1\varepsilon}\frac{\varepsilon}{k}\nu_t\left(S_{ij}\right)\frac{\partial \overline{u_i}}{\partial x_j}+\frac{\partial}{\partial x_i}\left(a_t\left(\nu+C_\mu\frac{k^2}{\varepsilon}\right)\frac{\partial \varepsilon}{\partial x_i}\right)-C_{2\varepsilon}\frac{\varepsilon^2}{k}-R \tag{3.28}$$

The standard values of all model constants are

$$C_\mu = 0.0845, \qquad C_{1\varepsilon} = 1.42, \qquad C_{2\varepsilon} = 1.68, \qquad a_k = 1.39, \qquad a_\varepsilon = 1.68$$

3.3.2.3 $k-\omega$ Turbulence model

This model is based on a modified version of the k equation used in $k-\varepsilon$ model and on the transport equation for the dissipation rate per unit kinetic energy (ω). The equations for k and ω are as follows:

$$\frac{\partial k}{\partial t}+\overline{u_j}\frac{\partial k}{\partial x_j}=\frac{\partial}{\partial x_j}\left[\nu+\frac{\nu_1}{\sigma_k}\frac{\partial k}{\partial x_j}\right]+\nu_t\left(\frac{\partial \overline{u_i}}{\partial x_j}+\frac{\partial \overline{u_j}}{\partial x_i}\right)\frac{\partial \overline{u_i}}{\partial x_j}+\beta^* k\omega \tag{3.29}$$

$$\frac{\partial \omega}{\partial t}+\overline{u_j}\frac{\partial \omega}{\partial x_j}=\frac{\partial}{\partial x_j}\left[\nu+\frac{\nu_1}{\sigma_\omega}\frac{\partial \omega}{\partial x_j}\right]+\nu_t\left(\frac{\partial \overline{u_i}}{\partial x_j}+\frac{\partial \overline{u_j}}{\partial x_i}\right)\frac{\partial \overline{u_i}}{\partial x_j}+\beta_1\omega^2 \tag{3.30}$$

The standard values of all model constants are:

$$\beta_1=0.075, \qquad \beta^*=0.09, \qquad \nu_1=0.553, \qquad \sigma_k=2.0, \qquad \sigma_\omega=2.0$$

The eddy viscosity is calculated from:

$$\mu_t=\rho\frac{k}{\omega}$$

3.3.2.4 Reynolds Stress Model RSM

The Reynolds Stress Model closes the Navier-Stokes equation by solving additional transport equation for the six independent Reynolds stresses and one for turbulent dissipation. The exact equation for the transport of the Reynolds stresses $R_{ij}=\overline{u_i'u_j'}$ is as follows

$$\frac{DR_{ij}}{Dt}=\frac{\partial R_{ij}}{\partial t}+C_{ij}=P_{ij}+D_{ij}-\varepsilon_{ij}+\Pi_{ij}+\Omega_{ij} \tag{3.31}$$

This yield to solve additional five transport equations for two dimensional flow and seven additional equations for three dimensional flow.

3.3.3 Large Eddy Simulation LES

In case of RANS, understanding and modeling the large eddies are considered as the most difficult and challenging aspects. The importance of these aspects arises from the fact that the largest eddies account for the most of the transport properties in turbulent flows. The size of the eddies get smaller and smaller at the regions near the wall and the RANS dealing with these smaller scale by using viscus damping functions. To model the small dissipating scale, RANS uses simplified assumptions and hence it is impossible for a single model to represent all turbulence features. In addition, it may also require fine-tuning of model constants to obtain better results for a given test case.

The Large eddy simulation tracks the behaviour of the larger eddies. It involves space filtering of the unsteady Navier-Stokes equations prior to the computations. This filters act in a way to pass the larger eddies and reject the smaller eddies. Most of the anisotropic is associated by the larger eddies while more or less the isotropic is associated by the smaller eddies. The interaction effects between the larger, resolved eddies, and the smaller, unresolved or modeled, eddies gives rise to sub grid scale stress which is described by means of an SGS model. The unsteady space filtered equations are solved on a grid of control volume with the SGS model to the unresolved stresses.

In CFD to get high quality results all the space-time scales must be taken into account when solving the unsteady Navier-Stokes equations. This implies that the discretization has to be very fine in order to represent all the scales numerically. In other words, the spacial and temporal discretisation of the domain has to be smaller than the characteristic length and the characteristic time encountered with the smallest scale of the exact solution. These solution criterion are extremely constrictive when the solution to the exact problem contains scales with wide range of sizes.

For the case of homogeneous and isotropic flow, which is the simplest turbulent flow case, the relation between the large scale , the characteristic length of the most energetic scale L, and the smallest scale, the smallest dynamically active scale η, is expressed as

$$\frac{L}{\eta} = O(Re^{3/4})$$

This relation is based on the Kolmogorov's theory which describes the transfer of the energy from the larger scales to the smaller scales. There are three main turbulent length scale as shown in Figure 3.7 which are the integral scale, the Taylor scale and the Kolmogorov scale.

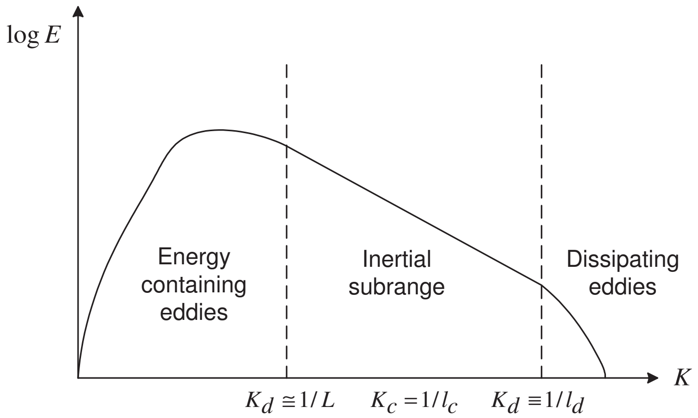

Fig. 3.7 Turbulent energy cascade.

The large eddies are unstable and they continue braking up into smaller eddies while transferring their energy to these smaller eddies. The smaller eddies braking up and transferring energy to even smaller eddies this process is referred to energy cascade. The energy cascade process continue until the $Re(l) \equiv u(l)l/\nu$ is sufficiently small that the eddy motion is stable, and molecular viscosity is effective in dissipating the kinetic energy. At these small scales, the kinetic energy of turbulence is converted into heat.

The integral length scale is defined as the length scale of the largest eddies in the energy spectrum. The size of these eddies is constrained by the geometry of the flow and they gain their energy from the main flow and from each other. The length scale of the largest eddies l_o can be derived based on the characteristic velocity u_o and the time scale $\tau_o \equiv l_o/u_o$. The characteristic velocity is on the order of the rms turbulent intensity $u' \equiv (2k/3)^{1/2}$. The equation of the integral length scale can be expressed as follows.

$$l_o \propto \frac{k^{3/2}}{\varepsilon} \tag{3.32}$$

The Reynolds number associated with these large eddies is called the turbulence Reynolds number Re_L.

$$Re_L = \frac{k^{1/2} l_o}{\nu} = \frac{k^2}{\varepsilon \nu} \tag{3.33}$$

3.3.4 Detached Eddy Simulation DES

According to Spalart [119] "*A pure LES of an airborne or ground vehicle would use well over* 10^{11} *grid points and close to* 10^7 *time steps, which is estimated to be possible in approximately 2045*". So a need for a hybrid RANS-LES technique arises to combine the advantages of the less computational cost in RANS with the advantages of the accuracy in the LES. The RANS-LES method divided the domain into two main parts, the near wall region where the turbulent boundary is solved and the outer region where the LES is performed.

DES is considered to be the most common hybrid RANS-LES type. DES was first introduced in 1992 by Spalart and Allmaras, the key idea behind DES is that the RANS model acts in the attached boundary layer and turns or witch to LES in the region far from the near wall. The grid resolution plays an important role in switching between the two models. For instance, the one equation model, well known as Spalart-Allmaras, is reformulated in DES by replacing the distance function d by a limiter function defined as:

$$l_{DES} = min\{d, C_{DES}\Delta\} \tag{3.34}$$

Where l_{DES} is the model length scale, d is the distance to the closest surface, $C_{DES} = 0.65$ is empirical derived constant and $\Delta = max(\Delta_x, \Delta_y, \Delta_z)$ is the largest dimension of the local grid scale.

The area where $d < C_{DES}\Delta$ which is a region in the vicinity of the wall, the model will behave as a RANS model, while in the area where $d > C_{DES}\Delta$ the model behave in an LES manner. Although DES turbulence model is a very promising tool, comprehensive practical application have been done on this approach and addressed potential failures . The phenomena known as modelled stress depletion (MSD) which occurs when the LES length scale activates within the limit of the attached boundary layer. The rise of (MSD) leads to a reduction in the eddy viscosity and as a result a reduction in the modelled Reynolds Stresses.

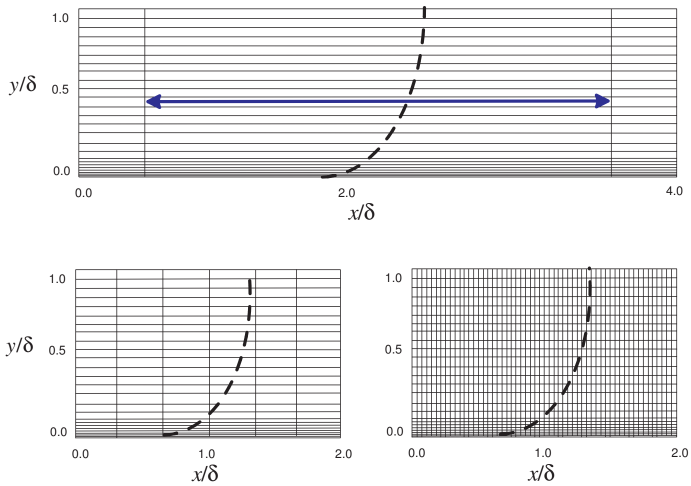

Fig. 3.8 DES different grid design.

3.4 Turbulence Models and Swirling Flow within Cyclone

The behaviour of the flow in the cyclone separator is described as an anisotropic turbulence with high swirl motion. Since the cyclone device operates at a high Reynolds number, a boundary layer will be formed on the wall of the cyclone, where the viscous forces balance the inertial forces, while an imbalance takes place between the pressure and the inertial stresses. This imbalance is due to two factors: 1) the pressure is constant across the boundary layer, and, 2) the spinning motion inside the boundary layer is attenuated by the effect of the fluid viscosity. Therefore, the estimations of the turbulence model should account for the high curvature of the streamlines, the dominance of swirl velocity and strong shear, and the adverse pressure gradients.

A large number of numerical and experimental studies have been conducted to investigate the flow within the cyclone. The vast majority of these numerical simulations were performed by using either the turbulent resolving approaches (LES or DES) or the Reynolds stress model (RSM). It should be noted that the flow within the cyclone is characterized as a swirling flow with a strong streamline curvature. In this scene, the conventional eddy viscosity turbulence models (EVMs) fail to predict the effects of strong streamline curvatures. This is unfortunate, as the robustness and computational cost of the EVMs are superior to the RSM as well as the LES [115].

It is well known that a major drawback of the EVMs is their incapacity to capture the effects of the streamline curvature and the system of rotation. More specifically, if the flow exhibits a swirl motion, EVMs fail to represent the near wall region "free-vortex" part of the Rankine vortex. This is attributed to the use of the Boussinesq hypothesis, that assumes that the eddy viscosity is an isotropic scalar which is not strictly true. In order to handle this weakness, many modifications aimed at the sensitization of EVMs to rotation and curvature have been suggested (see Refs. [54, 71, 99]). These attempts are limited and not universal, especially when dealing with 3D flows. Moreover, these corrections are not Galilean-invariant. In 1997, Spalart and Shur proposed an empirical alteration to EVMs to account for the system of rotation and streamline curvature [118], which in a sense is close to an idea of Knight and Saffman [77]. The former is more efficient as it measures the extra influence of the invariant contributor to the turbulence. It is also relatively easy to apply to 3D flows and unifies the description of the curvature and rotation effects in the mathematical model. By 2009, Smirnov and Menter [115] had adapted the rotation-curvature correction function proposed earlier by Spalart and Shur [118] to the shear stress transport $k-\omega$ model (SST $k-\omega$). The correction function is applied to the production term in both the k and the ω transport equations. As a result, the corrected model, denoted as the SSTCC, becomes more accurate, computationally efficient and robust than its predecessor. In 2013, a new simpler rotation and curvature correction method for the S-A model was proposed by Qiang et .al [138]. The Qiang modification avoids the calculations of the components of the Lagrangian derivatives of the strain rate tensor (DS_{ij}/Dt) by implementing the Richardson number (Ri). The model is denoted as SARCM, where the M stands for modified.

Chapter 4

Finite Volume Discretisation

4.1 Introduction

The principle objective of the CFD approach is to solve the governing partial differential equations numerically, and this can be done by utilising a discretisation method. The purpose of the discretisation process is to transform the governing equations into a corresponding system of algebraic equations, which can then be solved computationally. The solution of the algebraic equations produces a set of values which corresponds to the flow variables at the grid points within the flow domain. The partial differential equations represent the conservation in terms of the rate of change of a particular property within a control volume as being balanced. This balance arises from three causes; one is the convective flux, the second is the diffusive flux and the third is the source or the sink term (or the source and the sink term together). For example, in case of turbulent kinetic energy, there is a production term associated to the large eddies and then there is a sink term associated to the very small eddies and together they determine the overall level of a particular quantity which is being conserved. The Finite Volume Method (FVM)is one of the most popular discretisation approaches that is used to solve fluid flow problems. The FVM can be summarised into the following three major steps:

1. The domain is subdivided into a number of finite sized sub-domains, these sub-domains are called the control volumes. Each sub-domain is represented by some

grid points.

2. The governing equations, which describe the flow physics, are integrated over the control volumes.

3. A profile assumption for the dependent variable (the interpolation function) has to considered for evaluating the integral in order to express the results in terms of algebraic quantities at the grid points.

4.2 Discretisation of the Solution Domain

The general concept of the discretisation of the solution domain is that the computational domain is subdivided into a net of points in space-time dimensions. This will produce a computational grid on which the governing equations are subsequently solved. Hence, the discretisation of the domain can be split into temporal discretisation and spatial discretisation. For instance, in transient cases, the temporal discretisation is simply the division of the computational time (T) into a set of time steps Δt.

The spatial discretisation is the division of the physical domain into finite control volumes in a such a way that the volumes completely cover the entire domain without overlapping with one another. Each control volume is closed by a set of faces, where the faces shared by two volumes are called internal faces and the faces coinciding with the domain boundary are called boundary faces.

Figure 4.1 illustrates typical two neighbouring cells, where the surface integral of the vector position of the centre of the surface S is defined as:

$$\int_{cs} (x - x_s)\, dS \tag{4.1}$$

Each control volume is represented by a certain grid point. In order to facilitate the calculations, this grid point has been chosen to be located at the centroid of the control volume

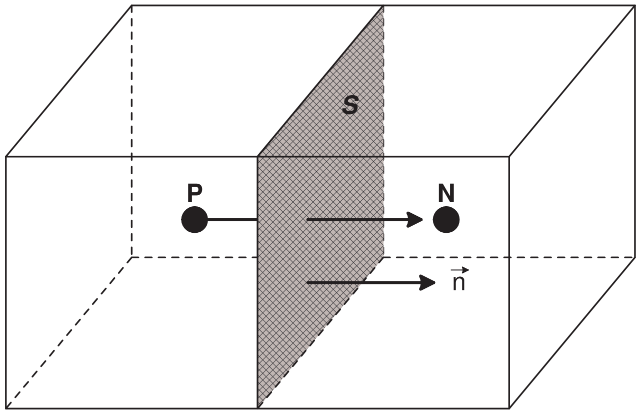

Fig. 4.1 Control volumes used in the finite volume method.

so that:

$$\int_{cv} (x - x_p)\, dV \tag{4.2}$$

The dependent variables are stored in the computational point P in the owner cell. During the computational process, these variables are transferred to the neighbouring cell through the internal face. For example, in Figure 4.1 the centroid of the owner cell is point P and the face area vector $\vec{n}$ of the shaded face is pointed out of the owner cell towards the centroid of the neighbouring cell N.

4.3 Discretisation of the Governing Equations

The standard convection-diffusion equations of variable of interest ϕ may be written as :

$$\underbrace{\frac{\partial \rho \phi}{\partial t}}_{\text{transient term}} + \underbrace{\frac{\partial}{\partial x_i}(\rho u_i \phi)}_{\text{convection flux}} = \underbrace{\frac{\partial}{\partial x_i}\left(\Gamma_\phi \frac{\partial \phi}{\partial x_i}\right)}_{\text{diffusion flux}} + \underbrace{\delta_\phi}_{\text{source term}} \tag{4.3}$$

For the sake of simplicity, let the convection flux be $F_{\phi c}$ and the diffusion flux be $F_{\phi d}$, where the net flux is $F_\phi = F_{\phi c} + F_{\phi d}$. Then equation (4.3) can be rewritten as follows:

$$\frac{\partial \rho \phi}{\partial t} + \nabla \cdot F_\phi = \delta_\phi \tag{4.4}$$

equation (4.4) represents the governing equation which is valid at every point within the discretised domain. In finite volume method, equation (4.4) is integrated over every control volume around each grid point at which we want to evaluate the dependent variables.

$$\int_{cv} \frac{d}{dt}(\rho\phi)\, dV + \int_{cv} \left(\nabla \cdot F_{\phi}\right) dV = \int_{cv} \delta_{\phi} dV \tag{4.5}$$

In order to convert the volume integral into a closed surface integral, the Gauss's law is applied to the integral of the net flux term:

$$\int_{cv} \frac{d}{dt}(\rho\phi)\, dV + \int_{cs} \left(\vec{n} \cdot F_{\phi}\right) dS = \int_{cv} \delta_{\phi} dV \tag{4.6}$$

equation (4.5) is the conservation form of the governing partial differential equation given by equation (4.3). The vector $\vec{n}$ appears in the surface integral is the normal vector associated with the surface that the flux transfer through during the computational process.

4.3.1 Profile Assumptions (*Interpolation schemes*)

The profile assumption, which is represented by the function ϕ, is responsible to interpolate the cell-centred values to the face-centered values and can be determined by utilising various types of differencing schemes. For one dimensional steady state problem with source term $\delta = 0$, equation (4.3) boils down to the following format:

$$\frac{d}{dx}(\rho u_x \phi) = \frac{d}{dx}\left(\Gamma \frac{d\phi}{dx}\right) \tag{4.7}$$

The first step to solve equation (4.7) using the finite volume method, is to integrate the governing equation over the control volume of size Δx that spans from west wall interface w to the east wall interface e on the grid layout shown in Figure 4.2. The corresponding formula resulting from integrating equation (4.7) from w to e with respect to x will be as follows:

$$(\rho u \phi)_e - (\rho u \phi)_w = \left(\Gamma \frac{d\phi}{dx}\right)_e - \left(\Gamma \frac{d\phi}{dx}\right)_w \tag{4.8}$$

Recall that for any fluid flow, the corresponding velocity field must satisfy the continuity equation. The integration of the continuity equation implies that:

$$(\rho u)_e - (\rho u)_w = 0 \tag{4.9}$$

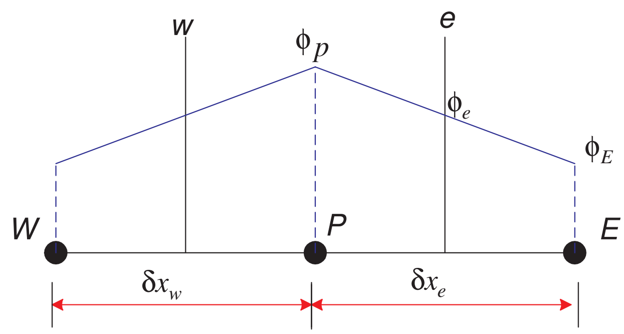

Fig. 4.2 A one dimensional control volume.

Where the quantity ρu represents the mass flux, which is the rate of mass flow per unit area normal to the direction. This physically means that the mass flux out is the same as the mass flux in, so that the mass flux $(\rho u \phi)$ is the rate of transport of the variable ϕ with the fluid flow. All the quantities in equation (4.8) have to be expressed in terms of algebraic values of the variable ϕ at the centroid grid points of the discretised domain, namely at points $(W, P$ and $E)$.

4.3.1.1 Central differencing scheme

For the sake of simplicity, let the convection and the diffusion terms be expressed in the following symbolic forms:

$$\begin{aligned} F &= \rho u \\ D &= \frac{\Gamma}{\delta x} \end{aligned} \tag{4.10}$$

Where F and D represent the conviction and the diffusion flux appearing in equation (4.7) respectively. From this perspective, the general form of the discretised equation of the control volume shown in Fig. 4.2 will be as follows:

$$a_P\phi_P = a_W\phi_W + a_E\phi_E \tag{4.11}$$

If the internal faces of the control volume are midway between the neighbouring cells and if the profile of the variable ϕ is assumed to be piecewise-linear, then equation (4.8) may rewritten as:

$$\frac{1}{2}F_e\left(\phi_E+\phi_P\right)-\frac{1}{2}F_w\left(\phi_P+\phi_W\right)=D_e\left(\phi_E-\phi_P\right)-D_w\left(\phi_P-\phi_W\right) \tag{4.12}$$

It should be noted that, the convection flux F depends on the flow direction, so it could have negative or positive value, also it indicates the strength of the flow or the so called (strength of convection). On the contrary, the diffusion flux (D) is independent of the flow direction and always remains positive and it indicates the diffusion conductance. By solving equations (4.11) and (4.12), the coefficients of the variables at cell-centred grid points using central differencing scheme will be:

$$a_E = D_e - \frac{F_e}{2} \tag{4.13a}$$

$$a_W = D_w + \frac{F_w}{2} \tag{4.13b}$$

$$a_P = a_E + a_W + \left(F_e - F_w\right) \tag{4.13c}$$

From the continuity equation, the last term in equation (4.13c) is zero. The ratio between the convection and the diffusion is a dimensionless quantity which is known as the Peclet number (Pe). Therefore, the dimensionless expression of equations (4.13a) and (4.13b) can be obtained by dividing both sides by D.

$$\frac{a_E}{D_e} = 1 - \frac{1}{2}(Pe) \tag{4.14a}$$

$$\frac{a_W}{D_w} = 1 + \frac{1}{2}(Pe) \tag{4.14b}$$

This particular scheme is called the **Central Differencing** scheme (CD). Ferziger and Peric [41] showed that the CD is the simplest second order accurate scheme. As the order of accuracy is higher than one, this scheme may produces oscillatory solutions for convection dominated problems where the local Reynolds number ($Re_c >> 1$) [63, 100]. This in turns violates the boundedness of the solution. More specifically, the possibility of the unboundedness in the CD scheme arises from the possibility of the variable coefficients in the discretised equation to be in different signs. For instance, if Pe is bigger than 2, it is obvious from equation (4.14) that the coefficients a_E and a_W are different in sign. However, many alternative schemes have been proposed to overcome the disadvantages of the CD scheme, including but not limited to, the Upwind Differencing schemes (UD), Total Variation Diminishing (TVD) and Normalised Variable Diagram (NVD). In this study two UD schemes are tested, namely; the first order UD and the second order Linear Upwind (LU). Also, the limited linear upwind (LLU), which is belongs to the (TVD) family and the Self Filtering Central Differencing (SFCD) which is based on the NVD. The next section discusses the UD secheme, for further information about the TVD and NVD schemes the interested reader can refer to [3, 13, 100, 111, 133].

4.3.1.2 Upwind differencing scheme

One of the alternative schemes which guarantee the boundedness of the solution is the well-known **Upwind Differencing** scheme (UD). The UD scheme was first proposed by Courant, Isaacson and Rees [26] and then reinvented by Gentry et al. [49], Barakat et al. [7] and Runchal et al. [109]. In the UD scheme, the variable ϕ at the wall interface is equal to the value of ϕ at the centroid grid point on the upwind side of that face, for this reason it is given the name upwind scheme. The concise form of the UD scheme which is illustrated in

Fig. 4.3 may be written as follows:

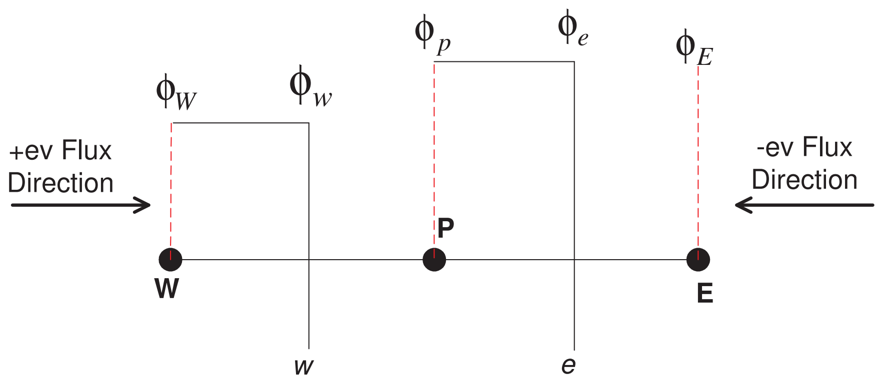

Fig. 4.3 Upwind scheme for positive (left) and negative (right) flow direction.

$$
\begin{aligned}
F_w\phi_w &= \phi_W \mathrm{max}(\mathrm{F}_w,0) \text{ - } \phi_P \mathrm{max}(\text{-}\mathrm{F}_w,0) \quad \text{flux through surface } w \\
F_e\phi_e &= \phi_P \mathrm{max}(\mathrm{F}_e,0) \text{ - } \phi_E \mathrm{max}(\text{-}\mathrm{F}_e,0) \quad \text{flux through surface } e
\end{aligned}
\tag{4.15}
$$

The variable coefficients of the discritiazed equation can be written as:

$$a_E = D_e + max\left(-F_e, 0\right) \tag{4.16a}$$

$$a_W = D_w + max\left(F_w, 0\right) \tag{4.16b}$$

$$a_P = a_E + a_W + \left(F_e - F_w\right) \tag{4.16c}$$

As the UD scheme considers the flux direction, this ensured that the variable coefficients in the discretised equation have the same signs, and hence it solved the dilemma of the unboundedness appearing in the CD scheme. Moreover, the UD is expected to behave in a more physical consistent way than the CD scheme for any arbitrary Reynolds number at cell level. However, the UD is first order accurate scheme and for highly conviction flow, it overpredicts the diffusion term.

4.3.1.3 Non-orthogonality and diffusion terms discretisation

Each of the aforementioned discretisation schemes has its own limitations. For instance, the CD scheme is closely related to the cell Peclet number (or cell Re), i.e., if the cell Peclet number $Pe > 2$, then the CD scheme no longer behaves in a stable manner and unboundedness appears in the solution. This limitation of the second order accurate CD scheme opens the way to the first order accurate UD scheme to some extent. As highlighted in the previous section, the UD scheme overpredicts the diffusion term which resulted in a severe false diffusion. For more explanation, consider the variable coefficient a_W in equation (4.16b), if the diffusion coefficient Γ is replaced by $\Gamma + \rho u \delta x/2$, then the coefficient a_W can be rewritten as:

$$a_W = \left(\frac{\Gamma}{\delta x} + \frac{\rho u}{2} \right) + max\left(F_w, 0\right) \tag{4.17}$$

The diffusion term in the above equation $\left(\frac{\Gamma}{\delta x} + \frac{\rho u}{2}\right)$ is nothing but the variable coefficient a_W in the CD scheme, precisely equation (4.13b). Therefore, it can be seen that the true diffusion coefficient in the UD scheme is incremented by a false diffusion coefficient $(\rho u \delta x/2)$. Although the false representation of the diffusion term leads to an inaccurate predictions, it corrects the wrong implications that arise from the CD scheme at large Peclet number (by keeping in mind that the diffusion term in the UD scheme is discretised using CD scheme, as shown in equation (4.17),).

The next section addresses the assessments of each scheme in terms of three main properties, the conservativeness, the boundedness and the transportiveness.

4.3.1.4 Assessments of CD and UD schemes

In terms of conservativeness, both schemes utilise consistent expressions to calculate the fluxes through the cell interface (A proof and more discussion can be found in [41, 83, 130]). As mentioned earlier, the UD accounts for the flow direction which is in stark contrast to the CD scheme for high Peclet number, thus CD cannot identify the flow direction in convection-dominated problems. In addition, it has been discussed in details that for (*Pe*

$>$ 2), the variable coefficients in CD will be in different signs and thus does not satisfy the boundedness criteria. This leads to a solution which is never converge or produces a converged-solution with 'wiggles' [130]. However, for low Peclet number, the second order accurate scheme (CD) is still the preferable choice for many CFD applications. To come up with a conclusion, it can be seen that the key factor, at least at this stage, to determine the proper choice between CD and UD scheme is the value of the cell Peclet number, which is defined as:

$$Pe = \frac{convection flux}{diffusion flux} = \frac{\rho u \delta_x}{\Gamma} \tag{4.18}$$

where ρ is the density of the fluid , u is the velocity of the fluid, δ_x is the cell size and Γ is the diffusion coefficient. Therefore, smaller value of *Pe* can be obtained by decreasing the velocity or refining the mesh to get smaller δ_x. Both options are not preferable for many CFD applications.

On the other hand, the UD scheme is indeed a better choice for high *Pe*, but it remains conditionally stable in terms of the mesh orthogonality. For instance, if the resultant velocity of the flow is approximately perpendicular to the control volume faces, the discretisation of the convection fluxes resulting with the UD scheme is comparably good. This is due to the negligibly small value of the approximated diffusion flux resulting with the UD scheme. For non-orthogonal meshes, the UD scheme does not take into account grid/flow direction inclination, which in turn leads to what is called 'False diffusion'. However, in 1972 Vahl Davis and Mallinson [128] proposed an approximate solution for the false diffusion coefficient for a two dimensional problem, as follows:

$$\Gamma_{diffusion} = \frac{\rho u \Delta x \Delta y \sin 2\theta}{4\left(\Delta y \sin^3 \theta + \Delta x \cos^3 \theta\right)} \tag{4.19}$$

where θ is the angle between the velocity vector and the x direction. It is obvious from the above equation that for $\theta = 0$ or 90^o, the false diffusion is zero, and the worst case occurs at $\theta = 45^o$. Therefore, the effect of the false diffusion can be minimised by refining the mesh (using smaller Δx and Δy) or by adjusting the mesh in such a way that it aligns with the mesh lines. Neither the refining nor the adjusting of the grid is practical for complex three dimensional CFD problems.

Unfortunately, the overwhelming majority of the CFD problems are experiencing a sort of meshing non-orthogonality and the orthogonal mesh is more an exception than a rule [74]. To limit the effect of the non-orthogonality, some correction approaches are introduced which aimed at preserving second order accuracy of the diffusion term discretisation. An intensive study of these different approaches can be found in [74, 95]. All numerical simulations in this study have adapted the over-relaxed approach by Jasak [74].

4.3.1.5 Over-relaxed approach

As noted from the previous section, the appearance of the false diffusion term is strongly related to grid non-orthogonality, which is not avoidable in many complex CFD cases. In this study, the over-relax approach proposed first by Jasak [74] is used. The main concept of this approach is to divide the face normal gradient $\vec{n} \cdot (\nabla\phi)_f$ into two components. Firstly, consider a general non-orthogonal face f within a discretised domain as shown in Fig. 4.4. Using the linear assumption of the variable ϕ and applying the volume integral to

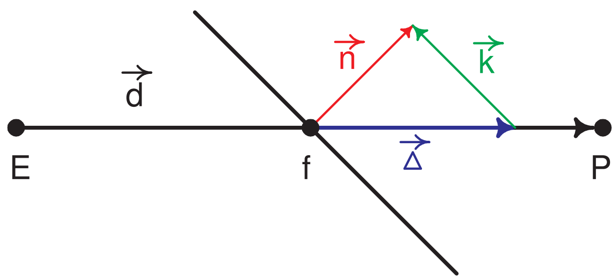

Fig. 4.4 Over-relaxed approach treatment of non-orthogonal mesh.

the diffusion flux in equation (4.3) will result the following discretised diffusion equation:

$$\int_{cv} \frac{\partial}{\partial x_i}\left(\Gamma_\phi \frac{\partial \phi}{\partial x_i}\right) dV = \Gamma_f \vec{n} \cdot (\nabla\phi)_f \tag{4.20}$$

In the fully orthogonal mesh the vector $\vec{n}$ is parallel to the vector $\vec{d}$, and thus the face normal gradient can be expressed as follows:

$$\vec{n} \cdot (\nabla\phi)_f = |\vec{n}| \frac{\phi_P - \phi_E}{|\vec{d}|} \tag{4.21}$$

In case of non-orthogonality, the term $\vec{n} \cdot (\nabla\phi)_f$ can be decomposed into two parts: orthogonal contribution and non-orthogonal correction [74].

$$\vec{n} \cdot (\nabla\phi)_f = \underbrace{\vec{\Delta} \cdot (\nabla\phi)_f}_{\text{orthogonal contribution}} + \underbrace{\vec{k} \cdot (\nabla\phi)_f}_{\text{non-orthogonal correction}} \tag{4.22}$$

The sum of the vectors $\vec{k}$ and $\vec{\Delta}$ must equal to the face area vector $\vec{n}$. Since the vector $\vec{\Delta}$ is parallel to $\vec{d}$, the orthogonal contribution part can be discretised in the following way:

$$\vec{\Delta} \cdot (\nabla\phi)_f = \left|\vec{\Delta}\right| \frac{\phi_P - \phi_E}{|\vec{d}|} \tag{4.23}$$

while the non-orthogonal part cannot be treated any further. So, the last form of the face normal gradient discretisation using the over-relaxed approach can be written as:

$$\vec{n} \cdot (\nabla\phi)_f = |\vec{\Delta}| \frac{\phi_P - \phi_E}{|\vec{d}|} + \vec{k} \cdot (\nabla\phi)_f \tag{4.24}$$

4.3.2 Source Term

The source term appeared in equation (4.3) cannot be written in a temporal, convection or diffusion expression. Therefore, it is treated as a general function of ϕ. Before discretising the source term, its collaboration with the other terms and its influence on the boundedness and accuracy should be taken into consideration. Some general comments on the treatment of source terms are given in [34, 100, 126].

The linearization of the source term can be written in the following expression:

$$\delta_\phi(\phi) = \delta_u + \delta_p \phi \tag{4.25}$$

where δ_u and δ_p may also depend on the variable ϕ, and the volume integral of the above equation will be as follows:

$$\int_{cv} \delta_\phi(\phi)\, dV = \delta_u V_p + \delta_p V_p \phi_p \tag{4.26}$$

4.3.3 Temporal Discretisation

For transient fluid flow problems, the spatial discretisation of the governing equations has to be also discretised in time. Since the mathematical behaviour of the governing partial differential equation is hyperbolic/parabolic in time, the solution marches forward in time and depends upon its history. For simplicity, the discretised convection, diffusion and source term are treated as one non-transient term. Therefore, equation (4.3) can be rewritten as follows:

$$\underbrace{\frac{\partial \rho \phi}{\partial t}}_{\text{transient term}} = \underbrace{-\frac{\partial}{\partial x_i}(\rho u_i \phi) - \frac{\partial}{\partial x_i}\left(\Gamma_\phi \frac{\partial \phi}{\partial x_i}\right) + \delta_\phi}_{\text{non transient term } \ell(\phi)} \tag{4.3}$$

Integrating the above equation over a control volume P yields:

$$\frac{\partial \rho \phi}{\partial t} V_P = L(\phi) \tag{4.27}$$

It should be noted that the temporal discretisation method of the transient term is not necessarily the same as the discretisation method applied to the non-transient term. However, the integration of equation (4.27) from t to $t+\Delta t$ with respect to time will be:

$$\frac{(\rho\phi)^{t+\Delta t} - (\rho\phi)^t}{\Delta t} V_P = \left(f L_\phi^{t+\Delta t} + (1-f) L_\phi^t \right) \Delta t \tag{4.28}$$

where the left hand side is the temporal discretisation of the transient term, and the right hand side is the discretisation of the non-transient term. If the discretisation of the transient term is left unchanged, then the new time-level convection, diffusion and source terms can be determined according to the weight factor f. For example, f is weighing between 0 (fully explicit scheme) and 1 (fully implicit scheme). While the well-known Crank-Nicholson scheme is resulted when f equals to 0.5.

4.3.3.1 Fully explicit scheme

In the fully explicit scheme, the new value of the variable ϕ and its gradient are determined only from the old values. For instance, if the weight factor f is zero, then the temporal discretised equation (4.28) will be written as:

$$(\rho\phi)^{t+\Delta t} = (\rho\phi)^{t} + \frac{\Delta t}{V_P}\left(L_{\phi}\right)^{t}\Delta t \tag{4.29}$$

The explicit scheme is only first order accurate in time, and it is unstable due to the Courant number limit (Courant et al. [25]). The Courant number is directly proportional to the size of the time step Δt and it is defined as:

$$Co = \frac{U_f \Delta t}{\Delta x} \tag{4.30}$$

where Δx is the characteristic length size of the cell. If the Co is bigger than unity, the explicit system behaves in an unstable manner. Hence it is conditionally stable. This is one of the major drawbacks of the explicit scheme, especially when it is used to solve a steady-state problem.

4.3.3.2 Fully implicit scheme

As in the explicit scheme, the implicit scheme is also first order accurate in time. But, it is superior over the explicit scheme as it guarantees the boundedness of the solution. The implicit scheme is resulted when the weight factor f is equal to 1. Therefore, the temporal discretised equation (4.28) for implicit scheme will be written as:

$$(\rho\phi)^{t+\Delta t} = (\rho\phi)^{t} + \frac{\Delta t}{V_P}\left(L_{\phi}\right)^{t+\Delta t}\Delta t \tag{4.31}$$

Equation (4.31) shows that the face variable (ϕ) at the new time-level ($t+\Delta t$) is determined from the old time-level variable (ϕ^t) and from the new time-level of the non-transient term. As a result, the coupling between the old and new time-level in the implicit scheme is much stronger than the explicit one, which guarantees its stability even if the Co number is bigger than one [62].

4.3.3.3 Crank-Nicholson scheme

The Crank-Nicholson scheme is a second order accurate in time, where the cell variable at new time-level $\phi_P^{t+\Delta t}$ is determined from both the old and the new time-levels of the faces' variables (ϕ_f^t and $\phi_f^{t+\Delta t}$), and from the old time-level of the cell variable ϕ_P^t as well. The temporal discretisation form of the Crank-Nicholson scheme is resulted when the weight factor f in equation 4.28 is equal to 0.5. Therefore, Crank-Nicholson scheme can be written as:

$$(\rho\phi)_P^{t+\Delta t} = (\rho\phi)_P^{t} + \frac{\Delta t}{2V_P}\left(L_{\phi}^{t+\Delta t} + L_{\phi}^{t}\right)_f \tag{4.32}$$

In order to write the full form of the discretised equation using Crank-Nicholson scheme, the sum of the fluxes through the faces surrounding the centroid P of a given cell has to be considered. Figure 4.5 shows a typical two dimensional cell surrounded by four faces.

Therefore, the full form of the Crank-Nicholson scheme applied to the given cell can be written in terms of the convection, diffusion and the source term in the following way:

$$\begin{aligned}\frac{\rho_p\phi_p^{t+\Delta t} - \rho_p\phi_p^{t}}{\Delta t}V_p + \frac{1}{2}\sum_f F\phi_f^{t+\Delta t} - \frac{1}{2}\sum_f\left(\rho\Gamma_{\phi}\right)_f\vec{n}\cdot(\Delta\phi)_f^{t+\Delta t}\\ +\frac{1}{2}\sum_f F\phi_f^{t} - \frac{1}{2}\sum_f\left(\rho\Gamma_{\phi}\right)_f\vec{n}\cdot(\Delta\phi)_f^{t}\\ = \delta_u V_p + \frac{1}{2}\delta_p V_p\phi_p^{t+\Delta t} + \frac{1}{2}\delta_p V_p\phi_p^{t}\end{aligned} \tag{4.33}$$

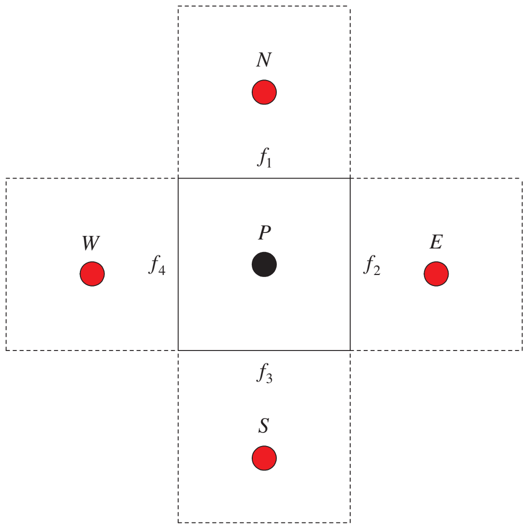

Fig. 4.5 Two dimensional control volume cell.

As shown in Fig. 4.5, the faces (f_1, f_2, f_3 and f_4) are shared with the neighbouring cells. Hence, the face variables ϕ_f and the gradient $(\nabla\phi)_f$ depend on the variable ϕ of the surrounding cells. Consequently, equation 4.33 can be written in an algebraic form to solve for $\phi_p^{t+\Delta t}$:

$$a_p\phi_p^{t+\Delta t} + \sum_N a_N\phi_N^{t+\Delta t} = R_p \tag{4.34}$$

It can be noticed from the last equation that the value of variable $\phi_p^{t+\Delta t}$ depends on the neighbouring cells. Therefore, the value of the cell variable at the new time-level $\phi_p^{t+\Delta t}$ can be obtained by solving the following system of algebraic equation:

$$[A]\,[\phi] = [R] \tag{4.35}$$

where the coefficient matrix $[A]$ is a sparse matrix, which consists of coefficients a_p on the diagonal and a_N elsewhere. The column vector $[\phi]$ contains all the cell variables ϕ-s that is needed to be solved, and $[R]$ is the source term vector. Solution techniques for the systems of linear algebraic equations will be discussed later.

4.3.4 Implementation of Boundary Conditions

The boundary conditions are applied to the faces coinciding with the physical boundary of the domain, which are known as the boundary faces. The boundary condition as a whole is a combination of physical and numerical boundaries. In fluid dynamics, the physical boundaries consist of walls, inlet, outlet and plane symmetry. At each single physical boundary, a numerical boundary condition should be specified.

4.3.4.1 Numerical boundary Conditions

The numerical boundary conditions are conventionally divided into two types. Dirichlet (fixed value) boundary conditions, at which the value of the dependent variables on the boundaries of the flow domain is specified. The other type is Von Neumann (fixed gradient) boundary conditions. For this type, the gradient of the dependent variables normal to the boundaries of the flow domain is specified.

Let's consider a cell within the domain which has one face coinciding with a physical boundary, as shown in Fig. 4.6. The face area vector **d** is the vector between the cell-centroid **P** and the centre of the boundary face **b**. As the area face vector is not perpendicular to the face, it is decomposed into orthogonal and non-orthogonal parts. The orthogonal part is represented by the vector $\vec{\Delta}$, which is equal to the face vector $\vec{n}$, but its location is not at the centre of the face. On the other hand, the contribution of the non-orthogonal part can be neglected because it is parallel to the boundary face. Therefore, the normal vector between the cell centre and the boundary face d_n can be written in the following way:

$$d_n = \frac{\vec{n}}{|\vec{n}|} \frac{d \cdot \vec{n}}{|\vec{n}|} \tag{4.36}$$

The numerical boundary can be divided into several primitive types; i.e., fixed value, fixed gradient and zero gradient, calculated and mixed primitive. In this study, the fixed value and fixed gradient primitive types are used.

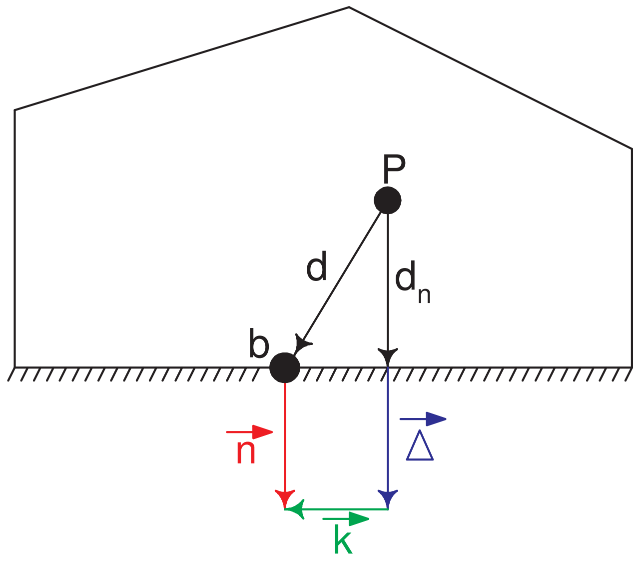

Fig. 4.6 A cell with one face coincide with boundary, adapted from [110].

- **Fixed Value boundary condition**

  In the fixed value boundary condition, the dependent variable ϕ is specified at the boundary face **b** and it is equal to ϕ_b. This condition should be taken into consideration when discretising the convection and the diffusion term at the boundary faces. The final discretised form of the transport equations are briefly introduced next. For more details, the interested reader can refer to [74, 110].

  - **Convection term**.

    The volume integral of the convection flux in equation (4.3) at the face boundary **b** is simply written as:

$$\int_{cv} \frac{\partial}{\partial x} F_{\phi c} dV = F_b \phi_b \tag{4.37}$$

  - **Diffusion term**.

    The discretisation of the diffusion flux given by equation (4.24) at the boundary face **b** can be written as:

$$\vec{n} \cdot (\nabla \phi)_f = |\vec{n}| \frac{\phi_b - \phi_P}{|\vec{d}_n|} \tag{4.38}$$

- **Fixed gradient boundary condition**

  In the case of fixed gradient type, the gradient of the variable ϕ normal to the boundary face is specified, which is the dot-product of the gradient and the outward pointing unit normal to the boundary face [74]:

$$\left(\frac{|\vec{n}|}{\vec{n}} \cdot \nabla\phi\right)_b = g_b \tag{4.39}$$

  - **Convection term**.

    The value of the variable ϕ at the boundary face is calculated from the variable at the cell centroid ϕ_P and the normal gradient given by equation (4.30).

$$\phi_b = \phi_P + |d_n| g_b \tag{4.40}$$

  - **Diffusion term**.

    The discretisation of the diffusion flux at the fixed gradient boundary condition is given by:

$$\left(\rho\Gamma_\phi\right)_b |\vec{n}| g_b \tag{4.41}$$

4.3.4.2 Physical boundary Conditions

In this section we limited the discussion of the physical boundary to only two types, namely, the patches (i.e. inlet and outlet) and the fixed wall boundary.

- **Inlet patch boundary**

  The most common way to specify the boundary conditions at the inlet patch is to prescribe the velocity field magnitude as a fixed value and the pressure gradient is set to zero. In case of turbulent flows, the turbulence variables are assigned also as a fixed value, where the value of these variables is calculated according to the selected turbulence model [98].

- **Outlet patch boundary**

  At the outlet boundary conditions, the pressure is assigned as a fixed value and zero gradient for the velocity and the turbulence variables.

- **Fixed wall boundary**
  A no-slip condition is specified at the fixed wall, where the velocity of fluid particles attached to the wall is equal to zero because the wall is stationary. The pressure gradient is also zero, while the turbulence variables is calculated according to the selected turbulence model or treated using various types of wall functions.

4.4 Solution Techniques for Systems of Linear Algebraic Equations

The most computationally demanding part of the CFD problems is the arithmetic solution of the linear algebraic equations that resulted from the discretisation process. Several methods can be used to solve the systems of the linear algebraic equations given, such as that by equation (4.35). A detailed discussion of these methods can be found in [53**?**]. In general, the existing solution algorithms can be classified into two basic categories. The first category is represented by direct methods. Theoretically, they give the exact solution of the system of algebraic equations in a finite number of steps. The other category, includes the iterative methods. In these methods, the solution starts with an initial guess, and then gradually improves until some solution tolerance is met. The direct methods are impractical for large system of equations, and that is due to two main reasons. The first is related to the number of operations that the direct methods require to reach the solution. For example, the total number of operations is proportional to the cube of the number of the equations of the system, and which is computationally expensive for large systems. The second reason is that the rounding error is magnified from the initial step to the next steps and then spreads in all following steps [23]. The iterative methods, on the other hand, are often more computationally effective as they require much less number of steps than the direct methods. Recall the system of the linear algebraic equations (equation (4.35)) resulting from the discretisation process:

$$[A]\,[\phi] = [R] \tag{4.35}$$

The above matrix is of sparse type, *i.e.*, most elements of the coefficient matrix are equal to zero. Hence, in order to significantly decrease the computer memory requirements, the selected solver should preserve the sparsity pattern of the matrix. One of the most attractive features of the iterative methods is the capability of these solvers to preserve the sparseness of the original matrix. Although the iterative solvers are superior over the direct solvers, in terms of computational demanding, they usually pose some requirements on the matrix. For example, they require the matrix to be diagonally dominant. The importance of this feature is that the convergence in iterative solvers is directly related to the diagonal pattern of the matrix.

In section (4.3), we discussed the effect of various discretisation methods on the boundedness of the solution. Both the boundedness and the convergence are closely related to the diagonal pattern of the matrix (the *diagonal equality* and the *diagonal dominance*).

- The diagonal equality is defined as; the magnitude of the diagonal coefficient is equal to the sum of the magnitude of the non-diagonal coefficients:

$$|a_P| = \sum_N |a_N| \tag{4.42}$$

- The diagonal dominance is defined as; the magnitude of the diagonal coefficient is equal to or bigger than the sum of the magnitude of the non-diagonal coefficients:

$$|a_P| \geqslant \sum_N |a_N| \tag{4.43}$$

Increasing the diagonal dominance of the system in iterative solvers leads to improvement towards the solver convergence. Table. 4.1 shows the contributions of each term in the discretised transport equation to the diagonality of the coefficient matrix $[A]$. For example, it shows that the temporal and the linear part of the source terms enhance the diagonal dominance unconditionally. While the diagonally equal matrix contribution is conditioned by the use of upwind differencing scheme in the discretised convection term, and on orthogonal meshes in the discretised diffusion term.

Table 4.1 Matrix contributions of discretised terms [87]

transport term	contribution to matrix		
	diagonal	off-diagonal	source
temporal	$a_p = \frac{\rho P^{t+\Delta t}}{\Delta t} V_P$	-	$R_P = \frac{\rho P^t \phi_P^t}{\Delta t} V_P$
convective	$a_P = f_x F$	$a_N = (1 - f_x) F$	-
diffusive	$a_P = -(\Gamma_{\phi,d})_f \frac{\lvert\vec{n}\rvert}{\lvert d\rvert}$	$a_N = -(\Gamma_{\phi,d})_f \frac{\lvert\vec{n}\rvert}{\lvert d\rvert}$	-
source	$a_p = \begin{cases} \delta_p V_p & \text{if } \delta_p < 0 \\ 0 & \text{if } \delta_p \geq 0 \end{cases}$	-	$R_p = \delta_u V_p + \begin{cases} 0 & \text{if } \delta_p < 0 \\ \delta_p V_p \phi_p^t & \text{if } \delta_p \geq 0 \end{cases}$
	(implicit treatment)		(explicit treatment)

Chapter 5

Cyclone and Swirling Flow

5.1 Swirling Flow

Vortex and swirling flow occur in a span range of different mechanical apparatus, for instance, in dust collection devices, spray dryers, vortex tubes and combustion chambers. Generally speaking, swirl behaviour can be defined as a combination of the tangential velocity component with the axial velocity component.

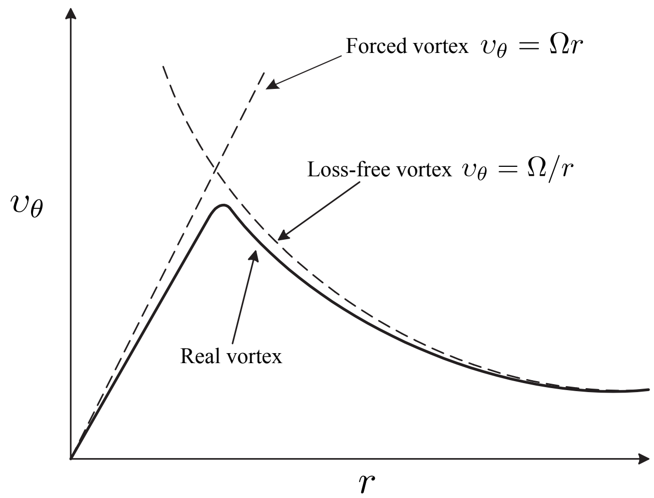

Fig. 5.1 Tangential velocity distribution of the two extremes vortex flows and a real vortex flow.

In real swirling flows, the tangential velocity distribution goes between two extreme swirling flows, namely, the solid-body rotation and the free vortex [67]. The earlier mentioned type is also known as forced vortex flow. By assuming that the fluid behaves like a solid body or has an infinite viscosity, the angular velocity of a fluid element remains constant at different radial positions. Hence, the swirling flow with constant angular velocity is called forced vortex flow or, in another context, solid-body rotation; so that:

$$\upsilon_t = \Omega r \tag{5.1}$$

Where υ_t is the tangential velocity, Ω is the angular velocity and r is the radial position.

The second extreme is in contrast with the forced vortex flow, where the fluid has no viscosity. In this case, the motion of the fluid elements at all radial positions has no influence on each other. For such a fluid, the relationship between the radial position and the tangential velocity is inversely proportional, so as the fluid element moves toward the centre of the circulation its tangential velocity increases. This relationship is referred as the conservation of the moment-of-momentum (mass times tangential velocity times radius of rotation: $m\upsilon_t r$). Since the moment-of-momentum is conserved, the quantity $mv_\theta r$ is constant, while the mass of the fluid element is constant this implies that $\upsilon_t r = constant$, so that:

$$\upsilon_t = \frac{constant}{r} \tag{5.2}$$

This type of extreme is called 'loss free' or 'frictionless'. From equation 5.2, the tangential velocity increases as the fluid element moves towards the centre of the rotation, or as the radial position decreases.

As shown in Fig 5.1, the real swirl flow intermediates between the solid-body rotation and the loss free vortex [85]. In real fluid, there are two main sources that cause the transportation of the moment-of-momentum between fluid elements at different radii, namely; the viscose effect and the presence of turbulent. Thus, in the inner core region, the tangential velocity of the real swirling flow nearly matches the one of the solid-body rotation, this inner core is surrounded by a nearly loss free vortex. The tangential velocity distribution which intermediates the two extremes is known as 'Rankine vortex'. Also it could be described in a general equation as follows:

$$v_t r^n = constant \tag{5.3}$$

where the value of the vortex exponent n determines the shape of the vortex. Some theoretical models of the flow pattern within cyclone estimated the value of n between 1 and -1 [84, 108]. According to other workers, the more frequent reported value of n was approximately 0.5 [5]. For instance, this value was obtained experimentally by Shepherd and Lapple[113]. Figure 5.2 shows the vortex exponent n as a function of cyclone diameter and at different gas temperatures.

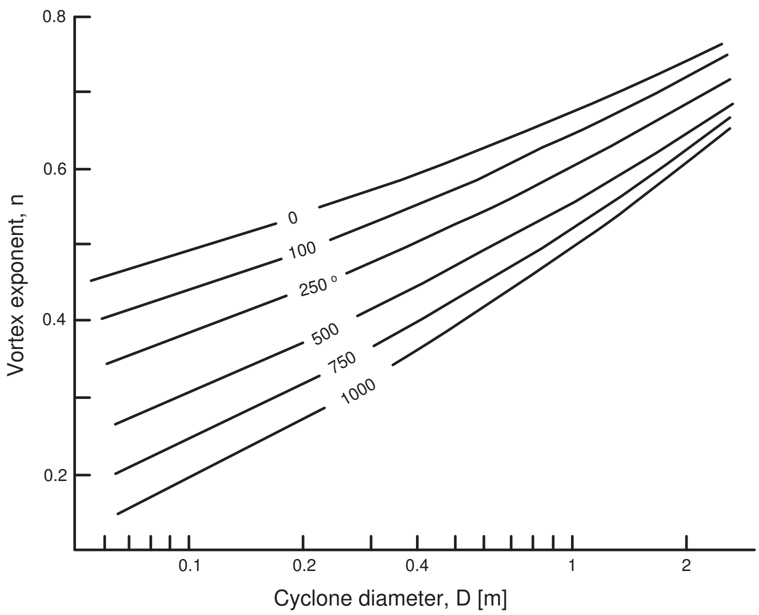

Fig. 5.2 Vortex exponent n as a function of cyclone diameter and gas temperature, adapted from [81].

To fully understand the mechanism of the cyclone, it is necessary to understand the flow behaviour of the gases within it. The flow pattern in the cyclone has been intensively investigated over the last few decades. For instance, in 1939 Shepherd and Lapple[113], investigated experimentally the velocity profile of the flow inside the cyclone. Their investigation has shown that the flow within the cyclone consists primarily of two flow regimes. The first regime is an outer downward spiral while the other is an inner upward spiral with lower velocity and smaller diameter as shown in Figure 5.3. The outer downward flow is

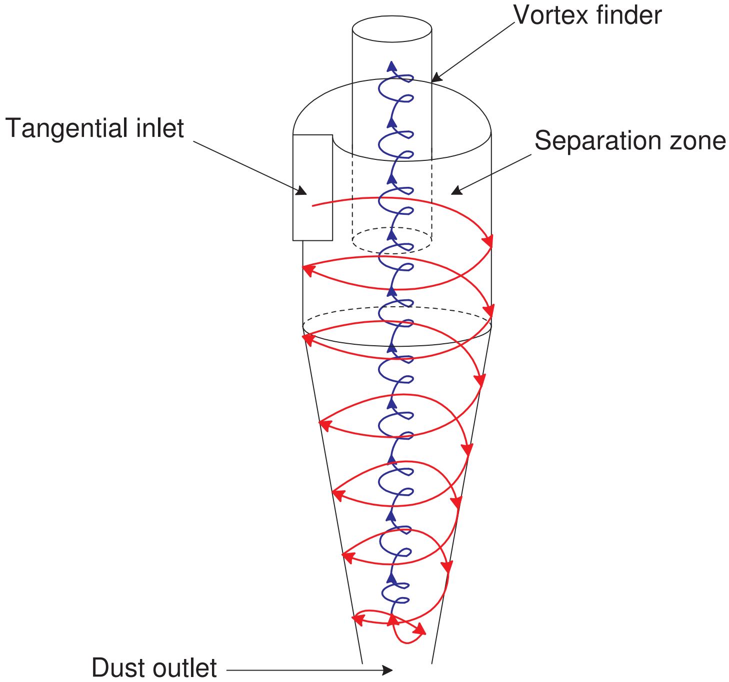

Fig. 5.3 Sketch of the flow pattern inside the cyclone separator.

of a great importance as it is responsible for transporting solid particles to the wall. This flow pattern is known as 'the outer vortex and the inner vortex'. The fluid transfers from the outer vortex to the inner vortex. The transferring process starts just below the vortex finder down through the conical part to a point close to the apex of the cyclone. The measurement of the Ter Linden [124] showed that in the upper part of the cyclone, the cylindrical part, the inner and the outer vortex interface at a radius are approximately equal to the radius of the vortex finder. The gas flow in the cyclone is, by nature, a three dimensional flow, the velocity components can be resolved into tangential, axial and radial components. The flow within the cyclone is dominated mostly by the tangential velocity and the strong shear [102, 127, 135].

The second velocity component which plays a major role in the reverse flow cyclone is the axial velocity component of the continuance phase flow. The transportation of the solid particles towards the apex of the cyclone are influenced by the axial velocity, but not by the gravitational force. In the outer vortex region (the near wall region), the direction of the axial velocity is downward and the gas moves towards the apex. At the inner vortex region (the near centre line region), the direction is upward and the gas moves towards the vortex finder [102]. Figure 5.4 shows a sketch of the axial velocity profile where the near wall is presented in negative direction to indicate that the flow is moving downward. Near the centre or the core of the cyclone, it is in positive direction to indicate that the flow is moving upward.

The pattern of the axial velocity profile was investigated over the years, see table 5.1. It is argued that the vortex finder diameter has a major influence on the axial velocity profile. Figure 5.5 shows the axial velocity profile of two different patterns, namely; the inverted V pattern to the left and the inverted W pattern to the right. Both profiles are at the same horizontal position of 0.125 m below the vortex finder, the one on the left of $D_e/D = 0.3$ and 0.375 for the one on the right.

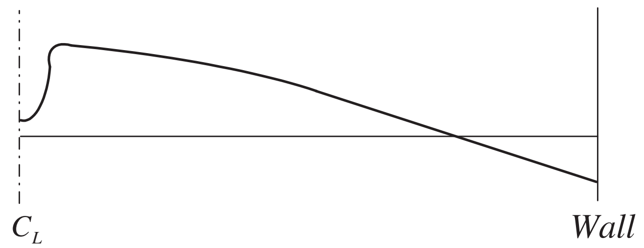

Fig. 5.4 Sketch of the axial velocity profile in cyclone separators.

The phenomenon of shifting the axial velocity profile in the inner vortex region from the inverted V to the inverted W was investigated by Horvath et al. [70]. They studied the effect of the vortex finder diameter on the axial velocity profile. They observed that when non-dimensional length D_e/D is less than 0.45, the V pattern profile is more stable. For higher D_e/D (bigger than 0.53), a low pressure occurs at the core of the vortex leading to what is called an increase of the back flow and the air from outside flows to the core and hence a *W* pattern is more stable.

Table 5.1 List of studies on the axial velocity pattern[59].

Class V		Class W	
Simulation	**Experiment**	**Simulation**	**Experiment**
Griffiths & Boysan.[57], Yoshida.[137], Frank & Yu.[45], Ma et al. .[86]	Kim & Lee.[76], Solero & Coghe.[117]	Slack et al. . .[114], Peng et al. . .[101]	Hoekstra .[64]

However, the vortex finder diameter is not the only factor that affects the flow pattern of the axial velocity within the cyclone. The apex shape and dimensions at the downstream exit have major influence on the whole internal flow, and therefore affect axial velocity profile of the reversed flow. For instance, Hoffmann et al. [66] showed that for a cyclone with a hopper section at the apex, the axial flow pattern is more likely a *V* patterned velocity profile. These findings are also agreed by Velilla [129].

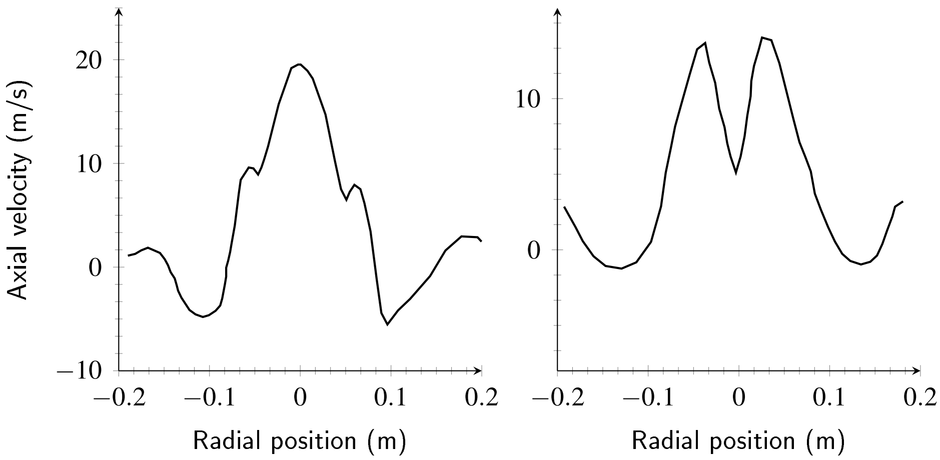

Fig. 5.5 Axial velocity profile in cyclone separators V pattern on the left and W pattern on the right [70]

5.2 Pressure Drop

The pressure drop in the cyclone is defined as the difference in the static pressure between the inlet and the outlets of the device [68, 81, 91, 94]. The performance of the cyclone separator, in terms of the operational cost, is directly linked to the pressure drop. Therefore, the geometrical dimensions of the inlet section and the outlet sections (the apex and vortex finder diameters) are significant variables, as they are directly related to the energy requirement. The tangential inlet causes the flow to swirl and spin around the longitudinal axis of the cyclone body. The spinning motion produces a field of pressure gradient in the radial direction, which provides a curvature for the gas flow (see section 1.5). However, the calculation of the pressure drop can be grouped into three main model approaches, theoretical and empirical models, statistical models and computational fluid dynamics (CFD) models [37].

Many empirical and theoretical models have been developed to predict the cyclone pressure drop (i.e. [1, 6, 20, 43, 75, 139]). For instance, Shepherd and Lapple [113], expressed the head loss in the cyclone from the Bernoulli equation:

$$\Delta H_v = F_{cv} + F_{ev} - 1 + \left(\frac{A}{A_e}\right)^2 \tag{5.4}$$

where F_{cv} is the friction loss associated to the cyclone proper and F_{ev} is the loss associated to the exit duct work. According to Shepherd and Lapple, the frictional loss F_{cv} consists of the following elements:

- Loss due to inlet expansion.
- Kinetic energy loss due to the rotational motion in the cyclone body.
- Wall frictional losses.

Whereas the value of F_{ev} can be computed from the Fanning equation:

$$F_{ev} = \frac{4fL_e}{e}\left(\frac{A}{A_e}\right)^2 \tag{5.5}$$

where f is the wall friction factor and it is a function of the Reynolds number (Re). Shepherd and Lapple model uses a wall friction factor, f, equal to 0.0055, while in both models of Barth and Stairmand, a value of 0.02 was used [8, 121]. From Fig. 5.6, the pressure drop decreases as the wall friction factor increases. In addition, Muschelknautz and Krambrock [94] measurements showed that the friction factor in the low *Re* flow regime sharply decreases as *Re* increases, and this is due to the decrease in the laminar boundary layer thickness. On the contrary, in the turbulent flow regime, the boundary layer thickness decreases to a smaller extent; therefore, a fractional decrease in the f value occurs as the *Re* increases. The explanation of the fact that the pressure drop decreases as the wall friction factor increases is illusory.

From the mechanical energy balance, it is not only the static pressure that is being lost, in fact, the viscous dissipation plays a crucial role in the determination of total pressure. One may define the viscous dissipation as the destruction term of the fluctuation velocity gradients by the action of the viscous stress. Thus, it leads to a reduction in the quantity $(p + 0.5\rho v^2)$. Some of the early semi-empirical models considered the energy losses in the pressure drop expression. For instance, this trend was adapted by Barth [8] to define the pressure drop as the subtraction of the total pressure between the inlet and the outlet. In this case, the total pressure at the inlet is the sum of the dynamic pressure $(0.5\rho v^2)$ and the static pressure. While a superficial exit velocity was used to formulate the velocity head at the outlet.

Similarly, Stairmand splitted the energy losses into three contributions: (1) the energy loss due to the velocity head at the inlet; (2) the energy loss due to the velocity head at the exit; and (3) the energy loss due to the centrifugal head of the cyclone vortex [121].

In 1992, Hoffmann et al. showed that the continuation existence of the swirl in the gas flow has a major influence on the total pressure loss, and hence the prediction of the pressure drop is more difficult to measure than it appears to be [69]. They explained that the total pressure is the sum of the static pressure and the tangential component of the dynamic pressure $(0.5\rho v_t^2)$, while the axial component is neglected as the radial distribution

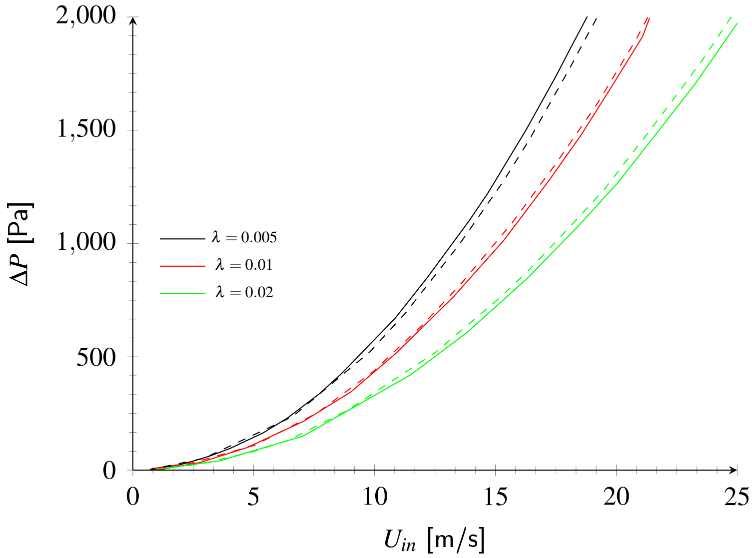

Fig. 5.6 Pressure drop, ΔP, of Stairmand high efficiency cyclone versus the inlet velocity, U_{in}, according to the models of (-) Stairmand (1949) and (- -) Barth (1956).

of the axial velocity profile in strong swirl is almost flat. To conclude, the viscous dissipation in the vortex finder has the most influence and dominates the total pressure loss in the cyclone device. Thus, the parameters that increase the value v_t also increases the pressure drop. This, in fact, explain the illusory of the relation between the pressure drop and the wall friction factor. In other words, an increase in the wall friction factor leads to a decrease in the magnitude of v_t, which in turn leads to a decreased losses in the vortex finder.

In addition, Hoffmann experiments reinforced the theory that the increase in the solid loading strongly decreases the pressure drop. This is in consistence with the predictions of Muschelknautz model. The explanation of this observation is that an increase in the solid loading lowers the tangential velocity and hence increases the wall friction which results in decreasing the pressure drop. Table 5.2 summarises different algebraic models of the pressure drop coefficient in cyclones.

The second approach to calculate the pressure drop is the statistical approach. For instance, in 1991, Ramachandran et al. [103] estimated the pressure drop based on a large

Table 5.2 Algebraic models of the pressure drop in cyclones

Model	Equation
Shepherd and Lapple [113]	$\xi_g = \frac{16ab}{D_e^2}$ (5.6)
Alexander [1]	$\xi_g = 4.62\left(\frac{ab}{D_c D_e}\right)\left[\left(\left(\frac{D_c}{D_e}\right)^{2\pi} - 1\right)\left(\frac{1-n}{n}\right) + f_g\left(\frac{D_c}{D_e}\right)^{2n}\right]$ (5.7) $f_g = 0.8\left[\frac{1}{n(1-n)}\left(\frac{4-2^{2n}}{3}\right) - \left(\frac{1-n}{n}\right)\right] + 0.2\left[\left(2^{2n}-1\right)\left(\frac{1-n}{n}\right) + 1.5\left(2^{2n}\right)\right]$ (5.8) n=1-$\left(0.67D_c^{0.14}\right)\left(\frac{T}{283}\right)^{0.8}$ (5.9)
Barth [8]	$\xi\left(\lambda = \lambda_g\right) = \left(\frac{ab}{\pi D_e^2/4}\right)^2\left(\xi_b + \xi_e\right)$ (5.10) Loss in the cyclone body $\xi_b = \frac{D_e}{D_c}\left(\frac{1}{\left(v_{ze}/v_{te} - ((H-S)/(0.5D_e))\lambda\right)^2}\right)$ (5.11) Loss in the vortex finder $\xi_e = K\left(\frac{v_{te}}{v_{ze}}\right)^{4/3} + \left(\frac{v_{te}}{v_{ze}}\right)^2$ (5.12)
Muschelknautz and Kambrock [94]	$\xi\left(\lambda = \lambda_g\right) = \left(\frac{ab}{\pi D_e^2/4}\left(\xi_b + \xi_e\right)\right)$ (5.13) $\xi_b = \lambda\frac{A_s}{0.9V}\frac{\rho_g}{2}\left(v_{te}v_{tw}\right)^{1.5}$ (5.14) $\xi_e = 2 + 3\left(\frac{v_{te}}{v_{ze}}\right)^{4/3} + \left(\frac{v_{te}}{v_{ze}}\right)^2$ (5.15)
Casal et al. [18]	$\xi_g = 11.3\left(\frac{ab}{D_e^2}\right)^2 + 2.33$ (5.16)

stets of different cyclone configurations, precisely on the cyclone dimensions (cylinder body diameter, inlet height and width, vortex finder diameter, separation zone height, total height and the apex diameter). The statistical findings of Ramachandran were more accurate than the empirical models of the 1940s and 1950s. Similarly, Casal et al. [19] statistical approach is based on a large data sets of pressure drop for various cyclone configurations [32].

Recently some studies used a CFD technique to calculate the pressure drop in cyclones. For example, Gimbun et al. presented a CFD calculation to predict and to evaluate the effects of temperature and inlet velocity on the pressure drop of gas cyclones [52]. The predictions of Gimbun were in consistence with Shepherd and Lapple model under different operational inlet velocity.

5.3 Collection Efficiency

The collection efficiency of cyclone determines its performance, and is considered as the basic purpose of such type of equipment. It is defined as the ratio of the inlet flow rate of solid particles to the collected particles. The physics behind the collection process is subjected to a list of forces that are applied to the particles. For instance, the literature lists centrifugal, gravitational, drag, particle-particle interaction and particle-wall interaction as the main forces that have a direct influence on the overall collection efficiency [51]. Among these different forces, the former is of great importance as it derives the solid particles to the body wall of the cyclone. Although the working principle of the collection process is simple to demonstrate, a tremendous effort had been put into developing mathematical models to predict the cyclone efficiency for a specific geometry under different operating conditions.

In general, cyclones collect particles with different diameters, and hence, the overall collection efficiency, $\overline{\eta}$, is indeed related to the particle size distribution of the particulate mass injected to the device. The variation of the collection efficiency with respect to the

Table 5.3 Formulae for the coefficient of solid loading effects ξ_s

Model	Equation
Briggs [17]	$\xi_s = \frac{1}{1+0.0086\left(C_{si}\rho_g\right)^{0.5}}$ (5.17)
Smolik [116]	$\xi_e = 1-0.02\left(C_{si}\rho_g\right)^{0.6}$ (5.18)
Baskakov et al. [9]	$\xi_s = \frac{1}{1+3.1C_{si}^{0.7}} + 0.67C_{si}$ (5.19)
	$\xi_s = \frac{\xi(\lambda=\lambda_s)}{\xi_g}$ (5.20)
Muschelknautz [93]	$\lambda_s = \lambda_g + 0.25\sqrt{\eta C_{si} Fr_e^{0.5} \frac{\rho_g}{\rho_s(1-\varepsilon_{str})}} \left(\frac{D_c}{D_c-b}\right)^{-0.625}$ (5.21)
	$\xi_g = 4.62\left(\frac{ab}{D_c D_e}\right)\left[\left(\left(\frac{D_c}{D_e}\right)^{2\pi}-1\right)\left(\frac{1-n}{n}\right) + f_g\left(\frac{D_c}{D_e}\right)^{2n}\right]$ (5.22)

particle size distribution is described as follows:

$$\overline{\eta} = \int_{0}^{\infty} f(x)\,\eta(x)\,dx \tag{5.23}$$

where $f(x)$ is the particle size distribution function (PSD) and $\eta(x)$ is the so called grade efficiency curve (GEC). It is assumed that the function $\eta(x)$ is independent of the (PSD). The analysis of Ontko [97] examined this assumption by experimental investigation of cyclone scaling using response surface technique, and no relation was found between $f(x)$ and $\eta(x)$.

The cyclone models of the grade efficiency curve presented in the literature could be grouped under two categories. Firstly, the models which estimate the grade efficiency as a function of the cyclone geometry and the operating conditions. The second; depends on the relationship between the characteristic particle size and the critical particle size or the so called cut-off size. The ideal or, the theoretical, grade efficiency describes the situation where all particles reaching the cyclone wall are fully captured and particles that are small enough not to reach the wall will not be captured and leave the device driven by the axial flow through the vortex exit pipe. This ideal situation is shown by the dotted line in Figure 5.7.

The theoretical calculation of the critical diameter can be determined by equating the centrifugal force and the drag force under steady state condition (see Figure 5.8). The forces acting on a particle of a density ρ_p and of a diameter d entering a cyclone of radius r at a tangential velocity υ_t and a radial velocity υ_r, are the centrifugal force and the drag force. The centrifugal force can be written as:

$$F_c = \frac{\pi d^3 \rho_p \upsilon_t^2}{6 r_{core}} \tag{5.24}$$

where r_{core} is defined in Figure 5.9, and the drag force can be written as:

$$F_d = 3\pi d \mu \upsilon_r \tag{5.25}$$

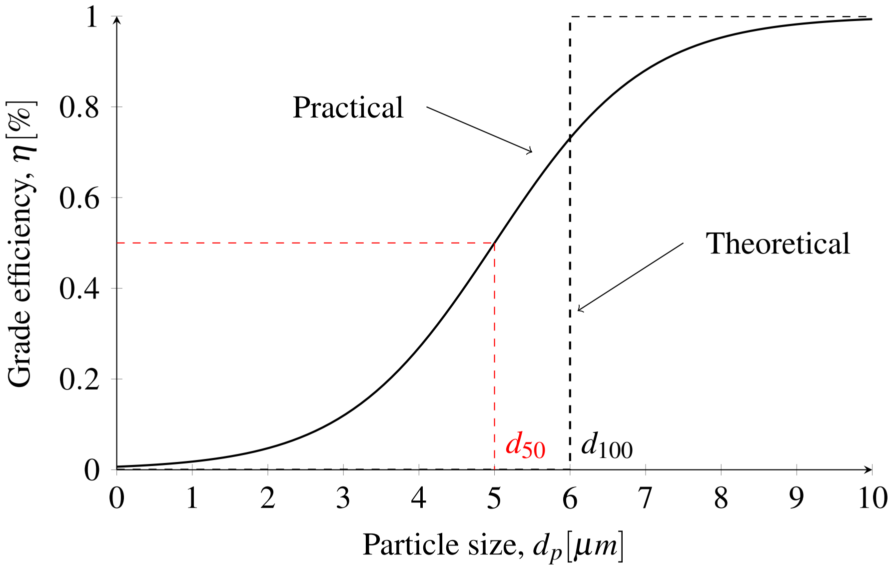

Fig. 5.7 Practical (-) and ideal (- -) grade efficiency curve of typical cyclone.

The value of the critical diameter d_p is inversely proportional to the collection efficiency,

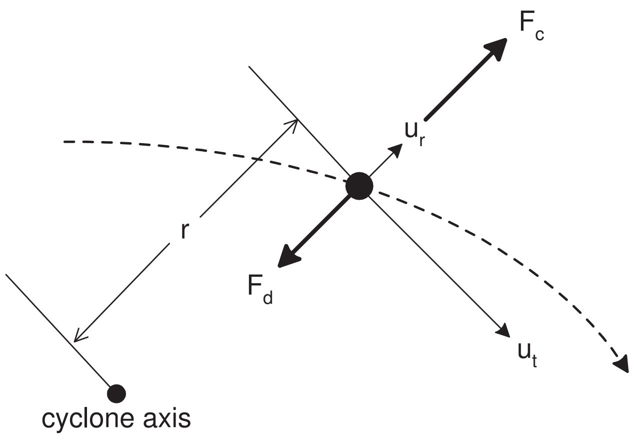

Fig. 5.8 Forces acting on a particle in a cyclone.

and hence, the cyclone efficiency will increase for:

- Higher tangential inlet velocity υ_t.
- Higher particle density ρ_d.
- Lower cyclone radius r.

In addition, the concept of the critical diameter d_{100} implies that the grade efficiency is zero for all particles smaller than d_{100} and 100% for all particles larger than d_{100}, which is not strictly true in practical situation [10, 106]. Moreover, the sharpness increase between the maximum and the minimum collection efficiency is not observed experimentally, and hence, it is very difficult to determine a specific critical diameter d_{100} for which all smaller particles will be escaped and larger ones will be collected. However, for the sake of design convenience, the critical diameter is replaced by a practical cut-off size d_{50} (shown by the dotted red line in Fig 5.7) for which all particles larger than this diameter will have a probability of 50% to be collected. Therefore, one could expect a collection curve distribution as shown by the solid line in Figure 5.7.

5.3.1 Critical Diameter: *The static particle or equilibrium-orbit approach*

Figure 5.9 shows the concept of the static particle or the equilibrium-orbit approach, where the dashed line represents the imagined cylindrical surface (*CS*) that is formed by continuing the vortex finder wall to the bottom of the cyclone [67]. The tangential velocity at the edge of the *CS* is at its maximum. The movement of the gas phase toward the central axis of the cyclone will past the *CS* with an averaged radial velocity given by:

$$\upsilon_r = \frac{Q}{2\pi r_{core}\,(H-S)} \tag{5.26}$$

where r_{core} is equal to the radius of the vortex finder, Q is the flow rate and H and S are defined in Table 1.1 and Figure 1.5. For the particles of critical diameter, the outwardly directed centrifugal force caused by their rapid rotation about the central axis is balanced against the inward drag force caused by the inrushing gas. As a result of this balance, these particles will theoretically remain suspended under static equilibrium state at the edge of the *CS*. Particles smaller than the critical diameter will be driven inside the (*CS*) region by the effect of the drag force and escape out the cyclone through the vortex pipe. On the contrast, particles larger than the critical diameter are centrifuged and spin out towards the cyclone wall and are collected. Under steady state condition, where the particle radial acceleration

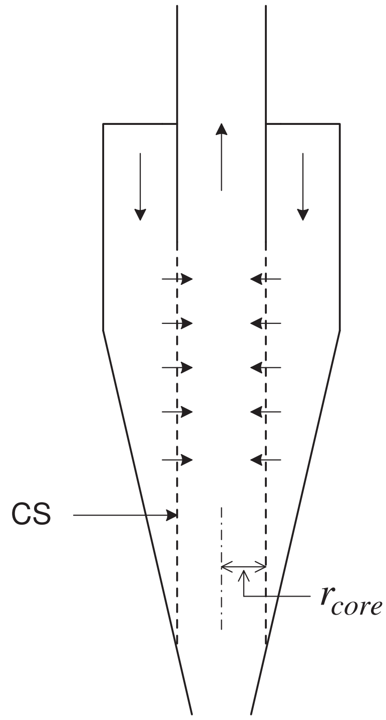

Fig. 5.9 Sketches showing the concept behind the equilibrium-orbit models.

and velocity is zero ($d^2r/dt^2 = dr/dt = 0$), the sum of the centrifugal and drag forces acting on the particle is zero:

$$\frac{\pi d^3 \rho_p \upsilon_t^2}{6 r_{core}} - 3\pi d \mu \upsilon_r = 0 \tag{5.27}$$

Then the critical particle diameter can be written as:

$$d_{100} = \sqrt{\frac{18 \upsilon_r \mu r_{core}}{\rho_p \upsilon_{max}^2}} \tag{5.28}$$

From equation 5.28, the critical diameter is related to the maximum tangential velocity and the averaged radial velocity of the gas phase. These velocity components depend on the cyclone physical geometry and the gas inlet velocity. Also, it is related to the physical properties of both the particle and the gas, *i.e.* the particle density and the gas viscosity. Table 5.4 shows three different approaches to estimate the critical diameter, Lappel and Barth used theoretical assumptions to develop the critical diameter equation, while Jones and Leith used experimental data to develop the critical diameter equation. The diameter of the cylindrical surface d_c appearing in the model of Jones and Leith is given by:

$$d_c = 0.25D\left(\frac{ab}{D^2}\right)^{-0.25} \times \left(\frac{D_e}{D}\right)^{1.53} \tag{5.29}$$

and the maximum tangential velocity υ_{max} is related to the inlet velocity υ_{in} and the dimensionless geometry parameter C_l and it is given by:

$$C_l = \left(\frac{ab}{D^2}\right)^{0.61}\left(\frac{D_e}{D}\right)^{-0.74}\left(\frac{H}{D}\right)^{-0.33} \tag{5.30}$$

The parameter z_c is limited by the apex diameter B and is given by:

$$z_c = \begin{cases} (H-S) - \frac{(H-h)(B-1)}{D} \times \left(\frac{d_c}{B} - 1\right) & \text{if } d_c > B \\ (H-S) & \text{if } d_c < B \end{cases} \tag{5.31}$$

Table 5.4 Formula for the cyclone critical diameter static particle approach [24].

Approach	Assumptions		Equation
Barth [8]	$r_{core} = D_e/2$	$\upsilon_{max} = \frac{4Q\theta}{\pi D_e^2}$	$\mathrm{d}_{100} = \sqrt{\frac{18\upsilon_r \mu r_{core}}{\rho_p \upsilon_{max}^2}}$ (5.32)
Stairmand [122]	$r_{core} = D_e/4$	$\upsilon_{max} = \frac{Q\phi}{ab}\sqrt{\frac{2\left(D-\frac{b}{2}\right)}{D_e}}$	$\mathrm{d}_{100} = \sqrt{\frac{9\upsilon_r \mu r_{core}}{\rho_p \upsilon_{max}^2}}$ (5.33)
Jones and Leith [72]	$r_{core} = d_c/2$	$\upsilon_{max} = 6.1u_{in} \cdot C_l$	$\mathrm{d}_{50} = \sqrt{\frac{9Q\mu}{\pi z_c \rho_p \upsilon_{max}^2}}$ (5.34)

5.3.2 Critical Diameter: *Time of flight approach*

The second approach to calculate the critical diameter is the time of flight approach. It is defined as the time that a single particle needs to travel from its initial position to the cyclone wall. For instance, if a particle with a critical diameter is injected from initial position r_i at the inlet velocity υ_{in} and it takes a time t to reach the wall, then the critical diameter can be written as:

$$d_{100} = \sqrt{\frac{9\mu D^2 \left(1 - \frac{2r_i}{D}\right)^{2n+2}}{4\left(n+1\right)\upsilon_{in}^2 \rho_p t}} \tag{5.35}$$

Some assumptions presented in the literature relate the residence time t to the empirical "number of turns," N, that the gas stream makes within the cyclone. Table 5.5 summarises different models to calculate the particle critical diameter by using the time of flight approach.

However, both critical particle approaches (the static particle approach and the time of flight approach) can be used as a rough estimator for the cyclone collection efficiency. Hence, none of these approaches can provide a full picture of the actual collection efficiency when a particular cyclone is injected with a range of different particles diameters. Consequently, the need for an alternative approach to estimate the overall cyclone efficiency influenced the emergence of what is known as the fractional, or the grade, efficiency curve, which is the subject of the next section.

5.3.3 The Fractional Efficiency Curve

In 1951, Lapple [78] developed a general curve to predict the entire fractional efficiency versus a range of dimensionless particles diameter. The diameters of the particle is normalized with the cut-off diameter given by equation (5.39). This curve is presented in Fig. 5.10. Theodore and DePaola [125] suggested an algebraic equation to relate the collection efficiency to the dimensionless diameter as follows:

$$\eta = \frac{1}{1 + a\left(d_{50}/d\right)^b} \tag{5.40}$$

Table 5.5 Formula for the particle critical diameter using time of flight approach [24].

Approach	Assumptions			Equation
Rosin et al. [108]	$n=0$	$t=\frac{\pi DN}{v_{in}}$	$r_i=\frac{D}{2}-b$	$d_{100}=\sqrt{\frac{9\mu b}{\pi\rho_p v_{in}}\left(1-\frac{b}{D}\right)}$ (5.36)
Lapple and Shepherd. [79]	$n=0$	$t=\frac{\pi DN}{v_{in}}\left(1-\frac{D_e}{2D}\right)$	$r_i=\frac{D-D_e}{2}$	$d_{100}=\sqrt{\frac{9\mu D_e}{2\pi\rho_p v_{in}N}}$ (5.37)
Davies. [28]	$n=1$	$t=\frac{H}{v_{in}}$	$r_i=\frac{D_e}{2}$	$d_{100}=\frac{9\mu D^2\sqrt{1-\left(\frac{D_e}{D}\right)^4}}{8\rho_p v_{in}H}$ (5.38)
Lapple. [78]	$n=0$	$t=\frac{\pi DN}{v_{in}}\left(1-\frac{D_e}{2D}\right)$	$r_i=\frac{D-b}{2}$	$d_{50}=\sqrt{\frac{9\mu b}{2\pi\rho_p v_{in}N}}$ (5.39)

where the values of the constant a and the logistic slope parameter b are 1 and 2 respectively. Iozia (Jones) and Leith [72, 73] estimated the logistic slope b from the cut-off diameter given by Equation 5.34 and the inlet dimensions as follows:

$$\ln(b)=0.62-0.87\ln(d_{50})+5.21\ln\left(\frac{ab}{D^2}\right)+1.05\ln\left(\frac{ab}{D^2}\right)^2 \tag{5.41}$$

In 1972 Leith and Licht [82] proposed a model that is based on several assumptions, i.e., the particles are spherical in shape, the drag force exerted on the particles is given by Stokes law, the acceleration of particles in the radial direction and the radial velocity of the continuous phase is zero. In addition, due to the existence of turbulence within cyclones, the Leith-Licht model assumes that all uncollected particles are completely mixed. Since then many other models have appeared to estimate the fractional efficiency curve. For instance, in 1981, Dietz [30] subdivided the flow domain into three zones, zone one covers the region between top cover of the cyclone to the inlet level of the vortex finder, zone two covers the annular region around the central core or (CS, see Figure 5.9) and zone three covers the core region inside CS. The purpose of these subdivisions is to account for the variation of the residence time and to comply more with axial reverse flow in the core region. This

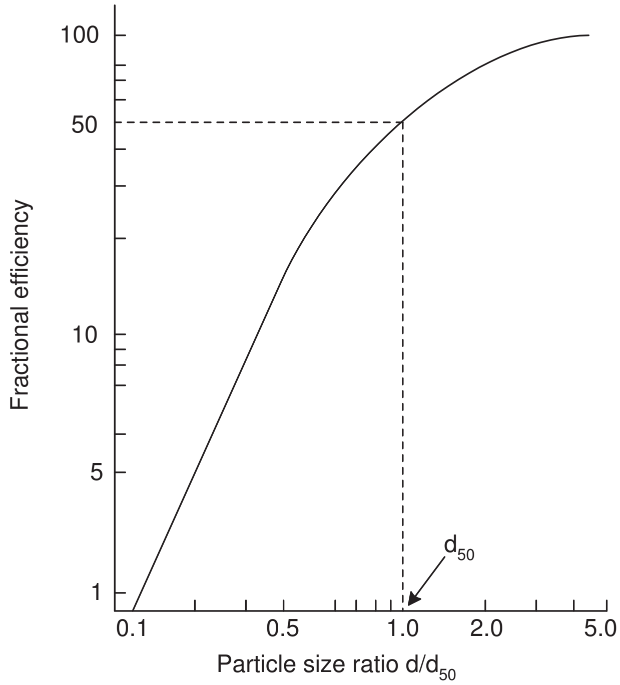

Fig. 5.10 Fractional efficiency versus d/d_{50} for Lapple design cyclone.

technique was adapted by Swaray and Hamdullahpur in their semi-empirical model [123].

Chapter 6

Numerical Implementation

6.1 Introduction

In this work, we build on the idea of Qiang which uses the Richardson number to avoid the calculation of the complex term (DS_{ij}/Dt), that appears in the non-dimensional argument $\tilde{r}$ (See Section 6.2.2). This leads to a simpler version of the SSTCC, which is realized by implementing the Ri number. As a result, the obtained numerical code needs less computational time and is also competitive in terms of accuracy when compared to the SSTCC model. The new formula for $\tilde{r}$ is applied to the Menter's SSTCC model and the modified model is denoted as SSTCCM. Then, the two altered models (namely; SARCM and SSTCCM) are implemented to study the flow within the cyclone. The swirl velocity components, characterized by the tangential and the axial velocity profile, are compared with the RSM and experimental data.

6.2 Mathematical Model

Cyclone separators operate normally at a range of $Re = 10^5$ to 10^6. Such a flow is considered to be fully turbulent. The fundamental physics of the fluid flow is described and governed mathematically by the Navier-Stokes equations. The conservation form of the incompressible Navier-Stokes equations are given by:

$$\frac{\partial u_i}{\partial x_i} = 0 \quad \text{continuity equation} \tag{6.1}$$

$$\rho \frac{\partial u_i}{\partial t} + \rho \frac{\partial u_i u_j}{\partial x_j} = -\frac{\partial p}{\partial x_i} + \frac{\partial}{\partial x_j}\left(2\mu s_{ij}\right) \quad \text{momentum equation} \tag{6.2}$$

where the term s_{ij} is the strain-rate tensor, which is written as:

$$s_{ij} = \frac{1}{2}\left(\frac{\partial u_i}{\partial x_j} + \frac{\partial u_j}{\partial x_i}\right) \tag{6.3}$$

To express equations (6.1) and (6.2) in the form of the **Reynolds averaged Navier-Stokes** (RANS) equations, the flow variables are decomposed into mean and fluctuating quantities. Then the time average process is applied, which yields the final form of RANS equations that can be written as follows:

$$\frac{\partial \overline{u_i}}{\partial x_i} = 0 \tag{6.4}$$

$$\rho \frac{\partial \overline{u_i}}{\partial t} + \rho \frac{\partial \overline{u_i u_j}}{\partial x_j} = -\frac{\partial \overline{p}}{\partial x_i} + \frac{\partial}{\partial x_j}\left(2\mu S_{ij} - \rho \overline{u_i' u_j'}\right) \tag{6.5}$$

where the term S_{ij} is the time averaged quantity of the the strain-rate tensor. The appearance of the additional term ($\tau_{ij} = -\rho\overline{u_i' u_j'}$) is known as **Reynolds stress tensor**. The system of the equations has to be closed in order to get a solution for the mathematical problem. This can be achieved by postulating a specific term of τ_{ij} in a framework of designing a turbulence model.

6.2.1 Standard Spalart-Allmaras (SA) model

The standard SA turbulence model is presented first by Spalart and Allmaras in 1992 [120]. It is a one equation eddy viscosity model. The SA model employs the Boussinesq hypothesis to relate the Reynolds stresses to the mean rate of deformation.

$$\tau_{ij} = -\rho\overline{u_i'u_j'} = 2\mu_t S_{ij} = \rho\tilde{\nu} f_{\nu 1}\left(\frac{\partial \overline{u_i}}{\partial x_j} + \frac{\partial \overline{u_j}}{\partial x_i}\right) \tag{6.6}$$

The transport equation for the viscosity-like variable $\tilde{\nu}$ is given by

$$\frac{\partial}{\partial t}(\rho\tilde{\nu}) + \frac{\partial}{\partial x_i}(\rho\tilde{\nu}u_i) = C_{b1}\rho\tilde{S}\tilde{\nu} + \frac{1}{\sigma_\nu}\left[\frac{\partial}{\partial x_j}\left\{(\mu+\rho\tilde{\nu})\frac{\partial\tilde{\nu}}{\partial x_j}\right\} + C_{b2}\rho\left(\frac{\partial\tilde{\nu}}{\partial x_j}\right)^2\right] - Y_\nu \tag{6.7}$$

where

$$\nu_t = \tilde{\nu} f_{\nu 1}, \qquad f_{\nu 1} = \frac{\chi^3}{\chi^3 + C_{\nu 1}^3}, \qquad \chi = \frac{\tilde{\nu}}{\nu}, \qquad \tilde{S} \equiv \Omega + \frac{\tilde{\nu}}{\kappa^2 d^2} f_{\nu 2} \tag{6.8}$$

Where $\Omega \equiv \sqrt{2\omega_{ij}\omega_{ij}}$ is the magnitude of the vorticity, d is the distance from the field point to the nearest wall and ω_{ij} is the mean rate-of-rotation tensor and is defined by:

$$\omega_{ij} = \frac{1}{2}\left(\frac{\partial u_i}{\partial x_j} - \frac{\partial u_j}{\partial x_i}\right) \tag{6.9}$$

The destruction of turbulent viscosity that occurs in the near-wall region due to wall blocking and viscous damping is given by:

$$Y_\nu = C_{w1}\rho f_w\left(\frac{\tilde{\nu}}{d}\right)^2 \tag{6.10}$$

The f_w function is used to accelerate the decaying behaviour of destruction and it is given by

$$f_w = g\left(\frac{1+c_{\omega 3}^6}{g^6 + c_{\omega 3}^6}\right)^{1/6} \tag{6.11}$$

In order to prevent a large value of f_w a limiter function g is used

$$g = r + c_{\omega 2}\left(r^6 - r\right) \tag{6.12}$$

Where r is defined as

$$r \equiv \frac{\tilde{\nu}}{\tilde{S}\kappa^2 d^2} \tag{6.13}$$

The eight closure coefficients of SA model are given in Table 6.1.

Table 6.1 Spalrt-Allmaras closure constants.

$\kappa = 0.41$	$c_{v1} = 7.1$	$c_{b1} = 0.14$	$c_{b2} = 0.62$
$\sigma = 2/3$	$c_{w1} = 3.21$	$c_{w2} = 0.3$	$c_{w3} = 2$

6.2.2 Spalart Allmars Rotation Curvature Turbulence Model (SARC)

As the standard SA model does not account for system rotation and streamline curvatures, Spalart and Shur [118] proposed an empirical alterations for this purpose. The formulation of SARC is similar to the original standard SA model except that the production term of turbulence viscosity in equation (6.7) is multiplied by a rotation function f_{r1}, which is given by:

$$f_{r1}(r^*, \tilde{r}) = (1 + c_{r1}) \frac{2r^*}{1 + r^*} \left[1 - c_{r3} tan^{-1}(c_{r2}\tilde{r})\right] - c_{r1} \tag{6.14}$$

Where the dimensionless quantities r^* and $\tilde{r}$ are given by:

$$r^* = \frac{S}{\Omega} \tag{6.15}$$

$$\tilde{r} = \frac{2\omega_{ik} S_{jk}}{D^4} \left(\frac{DS_{ij}}{Dt} + \left(\varepsilon_{imn} S_{jn} + \varepsilon_{jmn} S_{in}\right) \Omega_m \right) \tag{6.16}$$

Here

$$S_{ij} = 0.5 \left(\frac{\partial u_i}{\partial x_j} + \frac{\partial u_j}{\partial x_i} \right), \qquad \omega_{ij} = \left(0.5 \left(\frac{\partial u_i}{\partial x_j} - \frac{\partial u_j}{\partial x_i} \right) + 2\varepsilon_{mji}\Omega_m \right) \tag{6.17}$$

$$S^2 = 2S_{ij}S_{ij}, \qquad \Omega^2 = 2\omega_{ij}\omega_{ij}, \qquad D^2 = 0.5\left(S^2 + \Omega^2\right) \tag{6.18}$$

The term DS_{ij}/Dt in equation (6.16) is the components of the Lagrangian derivatives of the strain tensor as mentioned earlier. It should be noted that rotation rate Ω_m appears in equation (6.16) and (6.17) is used only if the reference frame itself is rotating. The empirical constants c_{r1}, c_{r2} and c_{r3} appear in equation (6.14) are given the values 1.0, 2.0 and 1.0 respectively.

6.2.3 Qiang and Yong Simpler SARCM

The calculation of the Lagrangian derivative of the strain rate tensor that exists in the SARC mode is a complex term and time consuming parameter to implement. Thus, in order to avoid the calculation of the higher order derivatives, Qiang and Yong [138] implemented the Richardson number Ri to account for the rotation-curvature effects. Hence, the term ($\tilde{r}$) is redefined as follows:

$$\tilde{r} = \frac{\Omega}{S}\left(\frac{\Omega}{S} - 1\right) \tag{6.19}$$

6.2.4 The Proposed SSTCCM Model

The proposed SSTCCM model is based on the shear stress transport model, which is an improved version of the two equations $k-\omega$ model. It was introduced in 1994 by Menter [89]. The model combines the two turbulence models ($k-\omega$ and $k-\varepsilon$). In the inner part of the boundary layer, the $k-\omega$ model is used and switches to the $k-\varepsilon$ in the free shear flow. The SST model employs the Boussinesq hypothesis to relate the Reynolds stresses to the mean rate of deformation as follows:

$$\tau_{ij} = -\rho\overline{u_i'u_j'} = \mu_t\left(2S_{ij} - \frac{2}{3}\frac{\partial u_k}{\partial x_k \delta_{ij}}\right) - \frac{2}{3}\rho k \delta_{ij} \tag{6.20}$$

The conservation form of the transport equations for both the turbulence kinetic energy k and the turbulent frequency ω can be written as:

$$\rho\frac{\partial(k)}{\partial t} + \rho\frac{\partial(u_j k)}{\partial x_j} = P_k - \beta^*\rho k\omega + \frac{\partial}{\partial x_j}\left[(\mu + \sigma_k\mu_t)\frac{\partial k}{\partial x_j}\right] \tag{6.21}$$

$$\rho\frac{\partial(\omega)}{\partial t}+\rho\frac{\partial(u_j\omega)}{\partial x_j}=P_k\frac{\rho}{\mu_t}-\beta\rho\omega^2+\frac{\partial}{\partial x_j}\left[(\mu+\sigma_\omega\mu_t)\frac{\partial\omega}{\partial x_j}\right]+2(1-F_1)\frac{\rho\sigma_{\omega 2}}{\omega}\frac{\partial k}{\partial x_j}\frac{\partial\omega}{\partial x_j} \tag{6.22}$$

The production term P_k is defined as:

$$P_k=\tau_{ij}\frac{\partial u_i}{\partial x_j}=\left[\mu_t\left(2S_{ij}-\frac{2}{3}\frac{\partial u_k}{\partial x_k}\delta_{ij}\right)-\frac{2}{3}\rho k\delta_{ij}\right]\frac{\partial u_i}{\partial x_j} \tag{6.23}$$

where the turbulent viscosity is defined as follows:

$$\mu_t=\frac{\rho a_1 k}{\max(a_1\omega,\Omega F_2)} \tag{6.24}$$

The blinding function F_1 in the freestream is zero ($k-\varepsilon$ model), and in the boundary layer is equal to one ($k-\omega$ model), given by:

$$F_1=\tanh\left(arg_1^4\right) \tag{6.25}$$

$$arg_1=\min\left[\max\left(\frac{\sqrt{k}}{\beta^*\omega d},\frac{500\nu}{d^2\omega}\right),\frac{4\rho\sigma_{\omega 2}k}{CD_{k\omega}d^2}\right] \tag{6.26}$$

$$CD_{k\omega}=\max\left(2\rho\sigma_{\omega 2}\frac{1}{\omega}\frac{\partial k}{\partial x_j}\frac{\partial\omega}{\partial x_j},10^{-20}\right) \tag{6.27}$$

$$F_2=\tanh\left(arg_2^2\right) \tag{6.28}$$

$$arg_2=\max\left(2\frac{\sqrt{k}}{\beta^*\omega d},\frac{500\nu}{d^2\omega}\right) \tag{6.29}$$

The constant closure coefficients of the SST model are given in Table 6.2.

The present model builds on the shear stress transport $k-\omega$ model (SST $k-\omega$) and also on the rotation function which was proposed in [115]. In the proposed model, the

Table 6.2 SST $k-\omega$ closure constants.

κ	σ_k	σ_ω	$\sigma_{\omega 2}$	β_1	β_2	β^*	a_1
0.4187	0.85	0.5	0.856	0.0785	0.0828	0.09	0.31

Richardson number Ri defined by Hellsten [61] is used to avoid calculating the terms D^4 and the complex Lagrangian derivatives. The modified rotation function is used to control the production term that appears in the transport equations. The incompressible form of the transport equations of the turbulent kinetic energy and its specific dissipation for the new SSTCCM model can be cast in differential form:

$$\rho\frac{\partial(k)}{\partial t}+\rho\frac{\partial(u_j k)}{\partial x_j}=f_{rot}P_k-\beta^*\rho k\omega+\frac{\partial}{\partial x_j}\left[(\mu+\sigma_k\mu_t)\frac{\partial k}{\partial x_j}\right] \tag{6.30}$$

$$\rho\frac{\partial(\omega)}{\partial t}+\rho\frac{\partial(u_j\omega)}{\partial x_j}=f_{rot}P_k\frac{\rho}{\mu_t}-\beta\rho\omega^2+\frac{\partial}{\partial x_j}\left[(\mu+\sigma_\omega\mu_t)\frac{\partial\omega}{\partial x_j}\right]+2(1-F_1)\frac{\rho\sigma_{\omega 2}}{\omega}\frac{\partial k}{\partial x_j}\frac{\partial\omega}{\partial x_j} \tag{6.31}$$

The production term P_k and the blinding function F_1 are given in equations (6.24) and (6.26), respectively. The rotation function f_{rot} is defined as

$$f_{rot}=max\{min(f_{r1},1.25),0.0\} \tag{6.32}$$

The term f_{r1} is the rotation function which is defined by Spalart in equation (6.14). Unlike the production term ($\tilde{S}$) in the SA model (equation (6.7)), which is based on the vorticity tensor Ω that characterizes the rotation, the production term P_k is based on the strain tensor rate S that characterizes the deformation. Therefore, P_k is higher than $\tilde{S}$, which justifies the use of the limiter in the rotating function f_{rot} [115]. The dimensionless quantities $\tilde{r}$ and r^* are defined as follows:

$$\tilde{r}=\frac{\Omega}{S}\left(\frac{\Omega}{S}-1\right) \qquad r^*=\frac{S}{\Omega} \tag{6.33}$$

The recommended boundary conditions for the farfield and at the wall for this model are given in Table 6.3.

6.3 File-based Structure of OpenFOAM Cases

OpenFoam CFD solver is a free, open source software package. The word OpenFOAM stands for Open Field Operation and Manipulation, it was released as an open source code in 2004. The code was written in a C++ object-oriented library to solve numerically the partial differential equations [132]. Recently, it gains popularity and spreads widely across both the engineering and the academic fields. As it was distributed under the General Public License (GPL) license, the use of OpenFoam is free of charge. In addition to that, the flexibility of the code allows the user to modify an exciting model or even implement his own model. These two features are the main reasons to use the OpenFoam code in this work, rather than many black-box commercial CFD platforms.

The basic structure of a file case in OpenFoam is illustrated in Fig. 6.1. The file case contains three basic directories; **system**, **constant** and **0** directories. The **system** directory consist of several dictionaries to control the simulation. The basic control dictionaries are the *controlDict*, the *fvSchemes* and the *fvSolution*. In the *controlDict* the user specifies the control parameters required for the simulation, such as the solver algorithm (Simple, Pimple, etc), the time step, the maximum Courant number, and the stop time. The temporal and the spatial discretization settings are specified in the *fvSchemes* dictionary. This dictionary is the most critical one, as it responsible for the accuracy and the stability of the discretized solution. The third basic control dictionary is the *fvSolution*, in this dictionary the user can specify the equation solvers, tolerances and algorithms for each primitive variables (the velocity, the pressure and the turbulence scalar quantities). In addition to these three dictionaries, the user can also include an extra dictionary to decompose the computational domain into several sub-domain. The decomposition process allows OpenFoam to be run in parallel on distributed processors. This feature is of great importance especially when solving complex cases; because it speeds up the computational time noticeably.

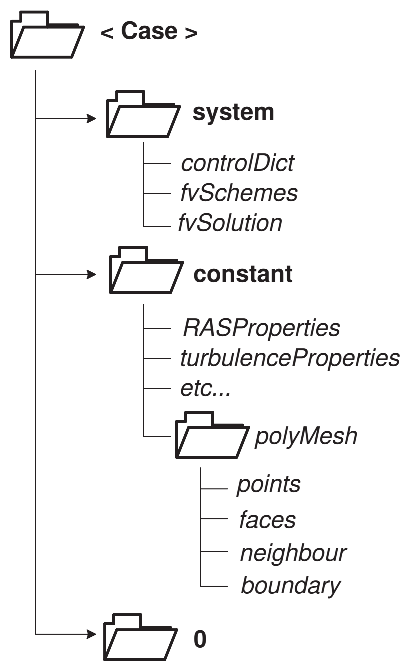

Fig. 6.1 Case file structure in OpenFoam.

The **constant** directory contains the mesh files, the physical properties of the fluid, *i.e.* the fluid density and dynamic viscosity. The choice of the turbulence model and the type of simulation RANS/LES are specified in the RASProperties file. The boundary and the initial conditions are both specified within the directory **0**. This directory contains files of the primitive and the turbulent scalar variables. The syntax of defining the scalar field type is differ when defining a vector field type.

6.4 Geometrical Domain and Grid Generation

Recent publications had studied the influence of cyclone separator geometry on the type of the flow patterns in cyclones. Although, these patterns are not yet fully understood, the basic features of the flow is well known. Horvath et al. [70] investigated experimentally and numerically the influence of the vortex finder diameter on the axial velocity profile. Two classes of the axial velocity profile were reported. An inverted W-shape profile was observed for vortex with diameter bigger than half of the cyclone body diameter. For smaller diameter (less than 0.45 of the body diameter) the profile takes an inverted V-shape pattern. The other geometrical parameter (the inlet width and height, the length of the cyclone body and vortex finder) have less influence on the overall flow structure. These findings are consistent with findings from other studies. The correct prediction of the gas flow inside the cyclone is a key factor to predict the pressure drop and the collection efficiency, which lies beyond the scope of this work.

The computational efforts as well as the accuracy of the solution highly depends on the mesh generation prior to the numerical analysis procedure. The grid can be fully structured, unstructured or hybrid. In structured grid type, the domain is decomposed into a regular hexahedral elements or squares. Therefore, the associated matrices that based on structured grid are highly organized and fast to assemble, and hence the resulting linear systems are also relatively easy to solve. In contrast, the unstructured mesh divides the domain into simple shapes, such as triangles or tetrahedrals, on an irregular basis. The influence of this mesh type yields matrices that are less organized and slower to assemble than the first type. The hybrid method is mainly used in complex geometry, where the regular parts of the domain are decomposed based on structured method, while the irregular parts can have unstructured grids. It is well known that the discretisation error arises from the size and the shape of the grid cells, while the numerical complexity is depend on the grid resolution (the number of cells) and the quality of the mesh. Consequently, it is all critically depends on the geometry of the physical domain. The body of the cyclone is considered as a highly complicated structure. This is because it consists of three unsimilar geometric shapes, which are a conical frustum, a circular cylinder and a rectangular prism. The way these shapes are attached to form the cyclone configuration, makes the meshing process extremely difficult. For example, even for coarse mesh, the fully structural hexahedral mesh yields a very dense grid area around the symmetry-axis, on one hand, and a high non-orthogonal faces on the other hand. For medium and fine grids, both the dense grid area and the level of the non-orthogonality increase dramatically. Unfortunately, these two major drawbacks of the structural meshes are unavoidable consequence. On the other hand, the hybrid mesh is more flexible and handle the problematics associated with the structural mesh type. In this work, the geometry of the cyclone body is decomposed by structural and hybrid techniques, while the unstructured grid method is eliminated due to high rate of convergence and CPU time it requires.

It is almost impossible to generate a structured mesh for the cyclone in any built-in mesh generation utilities available in OpenFoam. Alternatively, it provides a list of mesh conversion methods which helps in using a wide range of free mesh generation codes. Gmsh-2.8.6 code [50] was implemented for this purpose. The domain is partitioned into several blocks according to the geometrical shape of the cyclone body. For example, each colored part of the meshed cyclone shown in Fig. 6.2 represents a different geometrical shape. The shape of the inlet section (red color) is a rectangular prism, but with a curved edge at the free-stream end attached to the cyclone body. The other shapes, conical frustum, circular hollow and circular cylinder are colored with blue, green and white respectively. This particular mesh contains 141066 elements, which is considered as coarse to medium level. Most of the cells are condense in the core as shown in Fig. 6.3. As the mesh is refined further, the gradient in cell volume near the symmetry-axis will get higher and higher. In addition, the number of non-orthogonal faces in this example is 531 faces with a degree bigger than 80°. OpenFoam solvers recommends using mesh with orthogonal faces, but if it not possible, the non-orthogonal feces angle better not to exceed 60°. A detailed image of the non-orthogonal surfaces can be seen in Fig. 6.4, which is formed due to the tangential attachment of the inlet section with the main body.

In order to minimise the deficiencies of the structured grid to the lowest possible degree, both the inlet section and the central core has to be meshed independently with the wall edges. Only the unstructured and the hybrid methods are capable to perform this task. In this work the hybrid technique was used to preserve most of the structured mesh of the discretised domain. the Figure 6.5 shows the semi-structured mesh which is used in order to decrease the non-orthogonality on one hand, and to avoid the dense mesh in the core region,

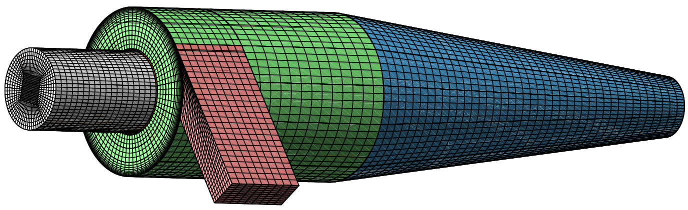

Fig. 6.2 Multi-block structured grid generated by Gmsh.

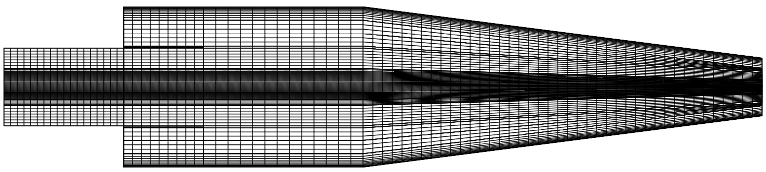

Fig. 6.3 High gradient in cell volume near the symmetry-axis occurs for structural grid type.

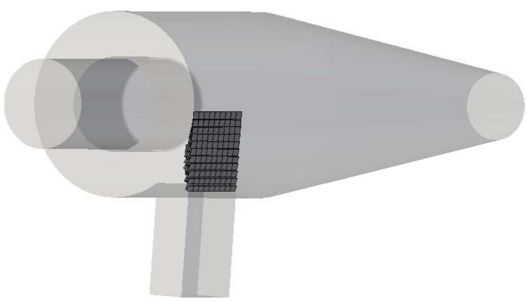

Fig. 6.4 Multi-block structured grid generated by Gmsh.

on the other hand. This mesh was created by using the snappyHexMesh utility provided by the OpenFoam. The y+ value is kept under 12, and a comparison between the two mesh styles are introduced in chapter 7.

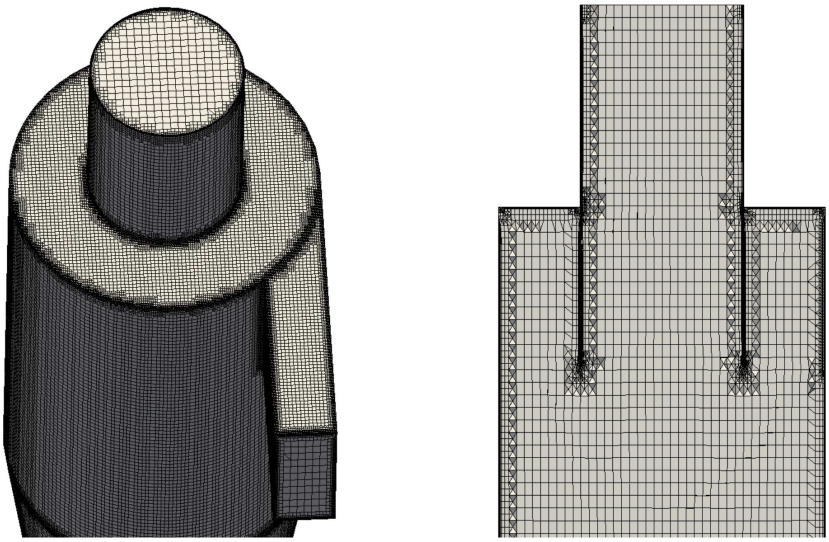

Fig. 6.5 Semi-structured mesh using snappyHexMesh utility.

6.5 Time-Marching Approach and Time Step

The numerical solution of a time dependent partial differential equations can be obtained by using either an explicit or an implicit approach. The properties of the solver algorithm critically rely on the choice between these approaches. In case of the implicit scheme, the current state of the linear system is obtained by solving the equations at the current and the next time steps. The implication of this technique lies in the additional computational efforts, and also the complexity of the programming code. However, the implicit schemes are always computationally stable, and hence no limitation for the Courant number is required to get a stable solution. On the other hand, the explicit scheme uses the current information of the variables to obtain the new variables at the next time step. Therefore, the stability condition highly dependents on the time step selection and hence the Courant number at the cell level. This reason causes the explicit schemes to be conditionally stable. But in comparison with stable implicit based solvers, the explicit schemes can be more reliable in terms of the storage requirements and the computational speed. The Fluent software is one of the most commonly used CFD solver that is based on implicit method, while the relatively new emerging code, OpenFoam, is based on the explicit solvers. So the time step selection directly affects the stability of the solution when using OpenFoam solvers, which is not true regarding to simulations that are performed by using the Fluent CFD kit.

A rough estimation of the time step selection when simulating cyclone can be represented by a small fraction of the average residence time (t_{res}) [39]. The t_{res} can be defined as the ratio of volume of the cyclone and the gas flow rate, $t_{res} = V/Q$. For example, the volume of the Stairmand high-efficiency cyclone can be calculated by summing the volumes of the four geometrical shapes shown previously in Fig. 6.2. If the gas flow rate is $0.08(m^3/s)$, and the volume of the cyclone is $0.02(m^3)$, then the $t_{res} = 0.02/0.08 = 0.25$. According to Elsayed [39], a proper time step Δt could be estimated as a tiny fraction of t_{res}, such as $\Delta t = 10e-3 \times t_{res}$. This estimation method could be valid for implicit solver based, but for explicit solver it is subject to monitoring the Courant number variation. Therefore for explicit schemes, the time steps are usually less than that of the implicit schemes by a fraction of $10e-1$.

6.6 Boundary Condition

The velocity inlet boundary condition is normalized to unity. Therefore the Re number can be adjusted by manipulating the kinematic viscosity.

$$Re = \frac{UL}{\nu} \tag{6.34}$$

normalizing the velocity to one enforces the Courant number to be at lower values. As the time step is inversely proportional to the Co number (See equation (4.30)), normalizing the inlet velocity will lower the possibility of the simulation to blow up. Standard wall functions are implemented in the near wall region to treat the boundary conditions of the turbulence quantities at the wall. In order to use the RANS turbulence models with wall functions effectively, the y+ value should not be exceed 20.

Table 6.3 Set up of the cyclone boundary conditions.

Boundary	**U** (m/s)	**p** (m^2/s^2)	**k** (m^2/s^2)	**omega** ($1/s$)	ν_t (m^2/s)
Inlet	(1, 0, 0)	zero gradient	$1.1\left(\frac{2}{3}(IU)^2\right)$	$\frac{\rho k}{\mu}\left(\frac{\nu_t}{\nu}\right)^{-1}$	$\nu\left(\frac{\nu_t}{\nu}\right)$
Top outlet	zero gradient	10^5	zero gradient	zero gradient	zero gradient
Bottom outlet	zero gradient	10^5	zero gradient	zero gradient	zero gradient
wall	(0, 0, 0)	zero gradient	0	$10\frac{6\nu}{\beta_1(\Delta y)^2}$	0

6.7 Numerical Schemes

The heads of the CFD balance triangle of any fluid mechanics problem, as one might say, are: the accuracy, the stability and the speed. The numerical schemes are used to construct the system of linear equations that approximates the CFD problem. There are different order of these schemes, first, second and higher orders. It is difficult, and even impossible in many cases, to have maximum accuracy with rock-solid stability at a minimum cost. For example, for high Re flow with complex geometry, the first order upwind scheme is stable but not accurate. To increase the accuracy, the order of the numerical scheme has to be at least second order, which in turn violates the stability of the solution.

The set up of the discretization schemes critically depends on the mesh generation. Therefore, accuracy , stability and speed of numerical solution are associated to some of the criteria that determine the quality of the mesh. For instance, the non-orthogonality is a key element, which should be treated under great care. The discretization of the diffusion and the gradient terms are determined according to the level of the non-orthogonality and the cell skewness, respectively. Therefore, the quality of the input data (mesh data) determines the reliability of the output, and hence the GIGO syndrome should always be avoided.

It should be noted that, for the turbulence quantities (*i.e.* k and ω), the preferable scheme is the first order upwind. This is because the convective terms inherent to the turbulent quantities are very sensitive to the respective higher order discretization schemes. In this work the first order upwind scheme was used in discretising the turbulence quantities. In order to increase the accuracy, the discretization of the velocity was gradually incremented from the first order upwind scheme (Gauss upwind) to the second order upwind scheme (Gauss linearUpwind) and finally to the self-filtered central differencing scheme (SFCD). The temporal discretization was set to the first order Euler scheme.

6.8 Solver Algorithm

There are two algorithms available in OpenFoam that deal with transient, incompressible flows. The default solver is the Pressure Implicit Splitting Operator (PISO) algorithm, which lies beyond the scope of this work. The other solver is based on the merged PISO-SIMPLE (PIMPLE) algorithm to solve the pressure-velocity coupling. The Semi-Implicit Method for Pressure-Linked equations(SIMPLE) algorithm is designed for stead-state conditions. It calculates the pressure after solving the velocity components from the momentum equation, hence it allows to couple by an iterative procedures. Figure. 6.6 illustrates the algorithm loop for one time step in the PIMPLE solver. The most attractive feature of this solver is its ability to calculate the momentum-pressure equations in a PISO mode, and using under-relaxation factor to correct the mass fluxes at the cell faces as a SIMPLE solver [21].

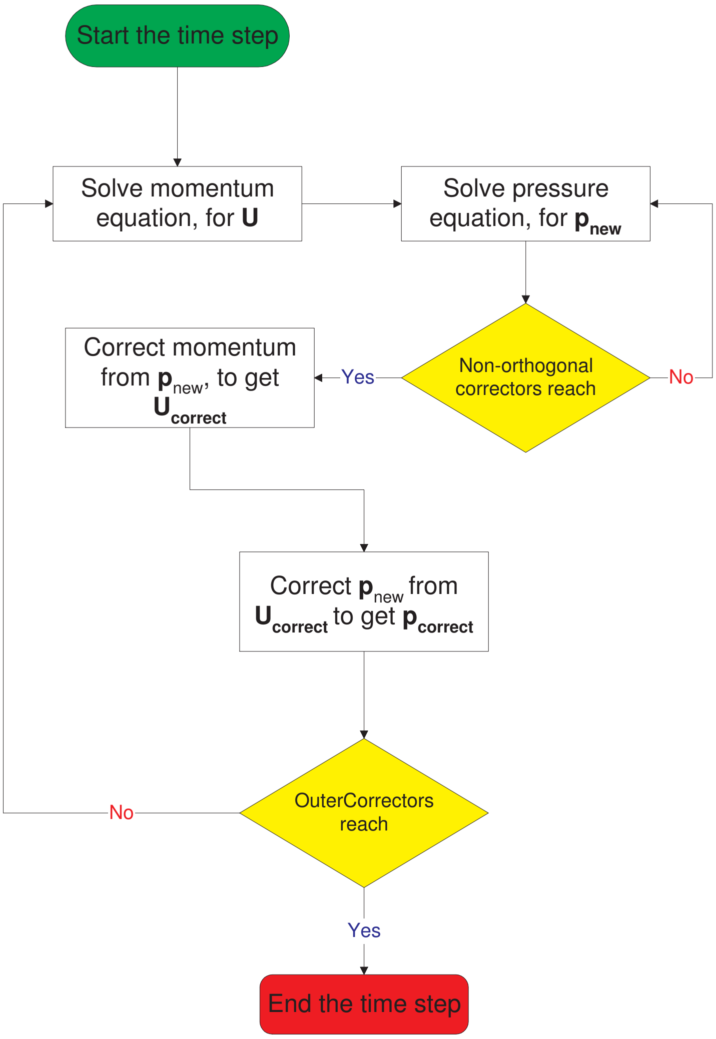

Fig. 6.6 PIMPLE algorithm loop for one time step.

Chapter 7

Results and Discussions

The obtained predictions are compared with the Laser Doppler Anemometry (LDA) experimental measurements and with the corresponding results of Reynolds stress model (RSM). Both the experiment and the RSM data were reported in [65]. In order to validate the new SSTCCM model, two simple benchmark problems were implemented and simulated first. The motivation behind these verification tests was to demonstrate the ability of the proposed model to tackle a swirl motion and a strong streamline curvature, which proved to be a challenge for EVM models. These tests has a relatively, as compared to cyclone, quicker turnaround time which allowed testing first a wider selection of turbulence models. As a result, the candidates models were identified for the following cyclone simulations.

7.1 Rotating-Lid in a Confined Cylinder

The confined cylinder with a rotating-lid case, that has been studied by Fujimura et al. [47], is chosen as a test case to validate the proposed model and to examine different numerical schemes outlined in the previous chapter. The computational domain is shown in Fig. 7.1a, which can be described as a confined cylinder, where the swirling flow is generated by a rotating-lid at the top end-wall of the pipe. Due to the shear forces, the flow in contact with the rotating-lid acquires a spinning motion. Consequently, the fluid particles are propelled radially outwards, while near the sidewall, the fluid spirals down. As it reaches the bottom end-wall, the fluid reverses its direction and moves from the sidewall towards the central axis before spiralling upwards. The characteristics of the flow pattern of this swirling motion depend mainly on two dimensionless parameters, i.e., the Reynolds number ($Re = R^2\Omega/\nu$), and the cylinder aspect ratio ($Ar = H/R$), where R is the radius of the cylinder, Ω is the angular velocity of the lid, and H is the height of the cylinder.

7.1.1 Computational Domain and Boundary Conditions

In order to facilitate the computational effort, an axisymmetric 2D simulation was performed. The computational domain of the 2D axisymmetric is shown in Fig. 7.1b. The numerical results are presented for aspect ratios of 1.5, 2.5 and 2.5 with the corresponding Re of 1290, 1010 and 2200, respectively. The mesh is refined according to the Re with a y+ value less than unity for all cases;

$$y+ = Re\left(\frac{\Delta y_1 u_\tau}{R^2\Omega}\right) \tag{7.1}$$

Where Δy_1 is the height of the first cell adjacent to the wall, and u_τ is the frictional velocity.

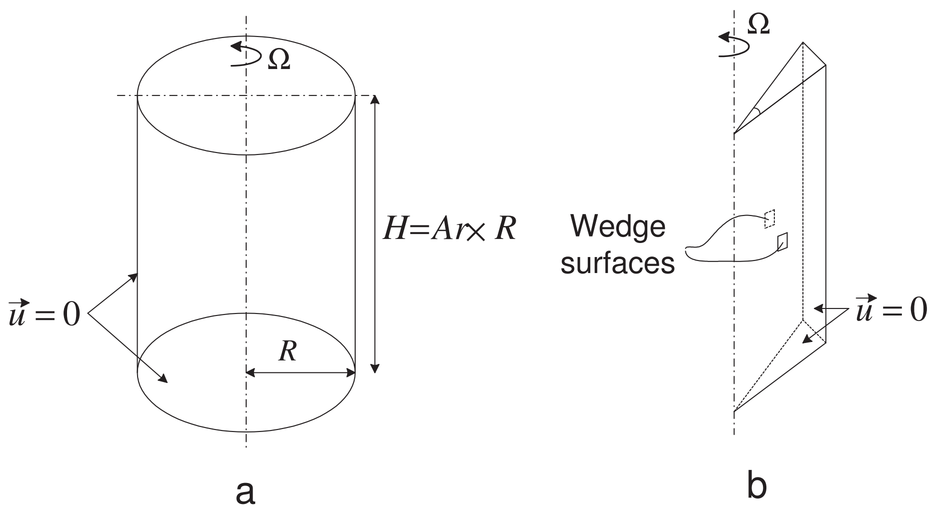

Fig. 7.1 a) Diagram of confined cylinder with rotating upper lid showing the different part of boundaries b) Axisymmetric 2D configuration.

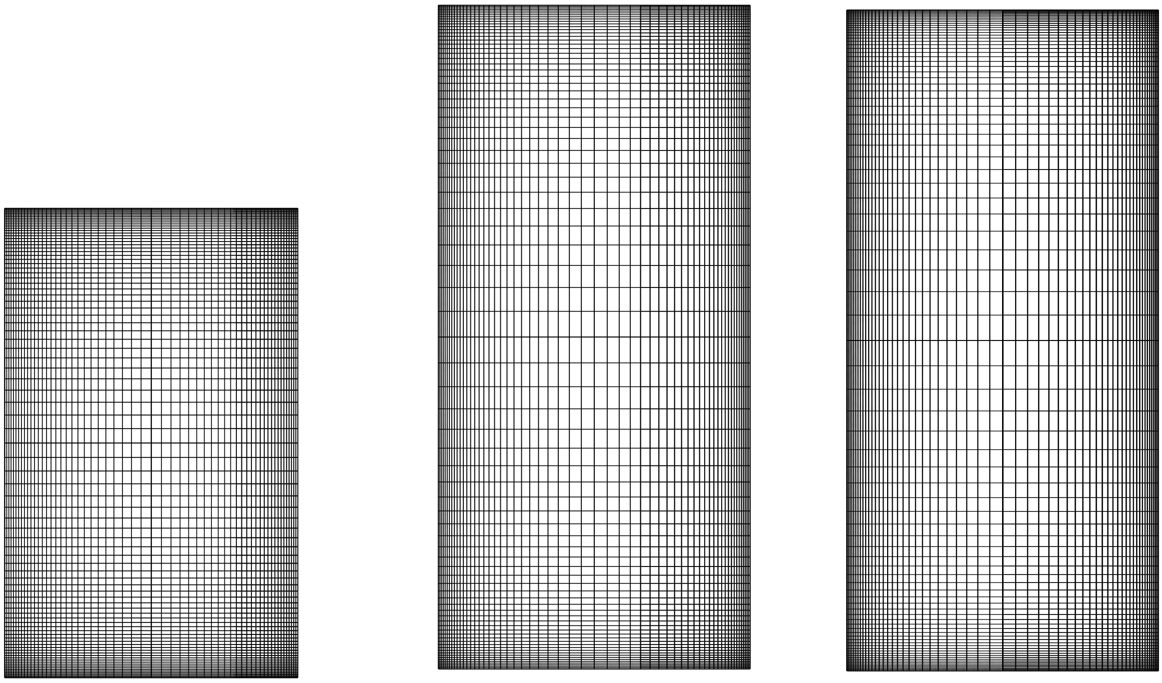

Fig. 7.2 Fine structured hexahedral mesh with y+ less than unity. From left to right case A, B and C.

7.1.2 Numerical Results

The relationship between the parameters (*Re* and *Ar*) and the number of vortex breakdowns was first observed by Escudier [40]. In this case study, three different regimes are considered, as indicated in Fig. 7.3. Cases A, B and C correspond to ($Re = 1920$ and $Ar = 1.5$), ($Re = 2200$ and $Ar = 2.5$) and ($Re = 1010$ and $Ar = 2.5$), respectively. Then, different numerical schemes are used to discretize the convective terms. The equations of the turbulence quantity variables (k and ω) are both discretised using the first order upwind scheme. For the velocity variables, two second order schemes are used, namely, Self-Filtering Central Differencing (SFCD) and Linear Upwind (LU), as well as the first order upwind scheme. Figure. 7.4 shows that the upwind scheme provides an erroneous streamlines for cases A and B. On the other hand, the second order schemes are both qualitatively in good agreement with the experimental measurements. Unlike the upwind scheme, the location and the number of the vortex breakdowns are accurately predicted by the second order schemes.

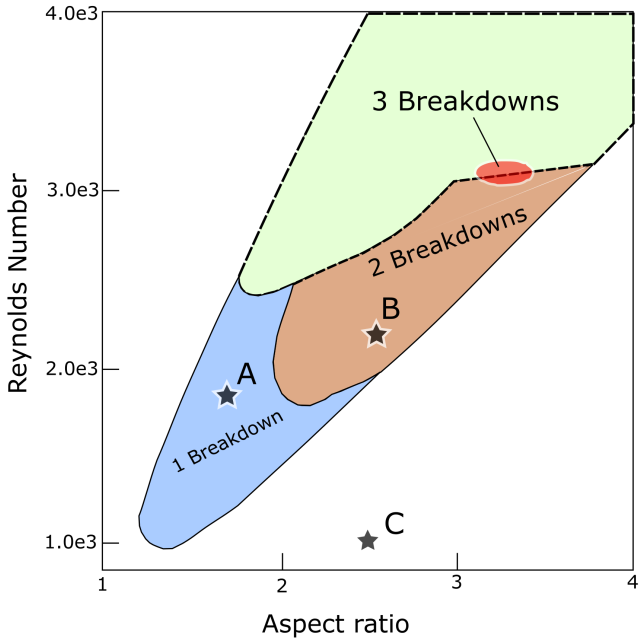

Fig. 7.3 Regime diagram of vortex breakdowns by Escudier.

Figure 7.5 shows that the SSTCCM model provides good predictions of the axial velocity profile along the longitudinal centreline when compared to experimental data. In terms of accuracy and reliability, the second order schemes are superior to the simple first order scheme. For example, Table. 7.1 shows that the upwind scheme for the fine mesh underestimates the maximum velocity by approximately 10% for case A and less than 1% for cases B and C. Although the upwind scheme seems to provide accurate predictions of the velocity profile, it cannot capture the formation of the vortex breakdown, as shown in Fig. 7.4. The results of the second order schemes demonstrate that the SFCD scheme provides insignificant improvement in terms of the grid refinement. On the contrary, the accuracy of the LU scheme is germane to the grid refinement (see Tables 7.3 and 7.2).

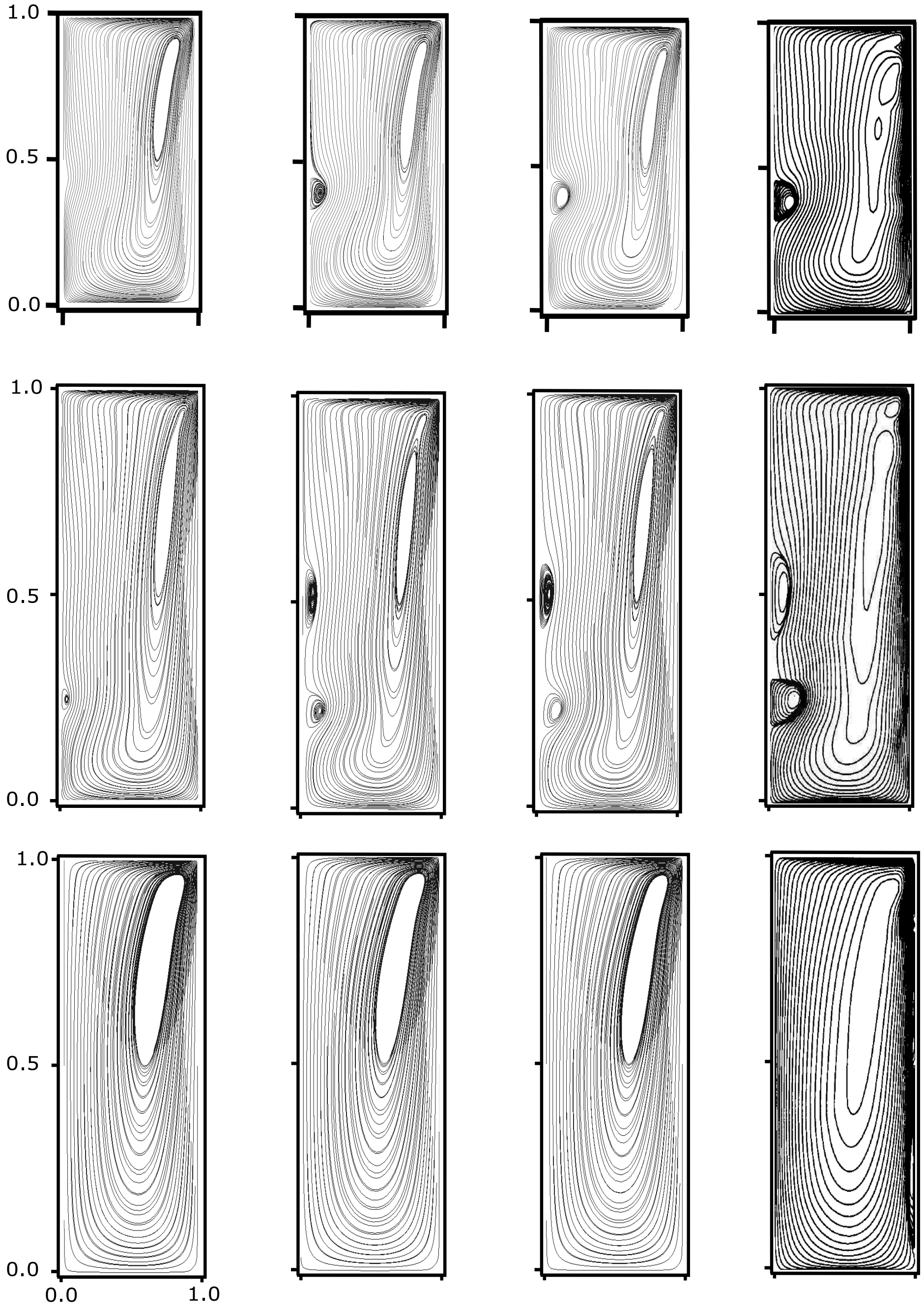

Fig. 7.4 Contour plot of the streamlines, from top to bottom, Case A ($Re = 1920$, $Ar = 1.5$), Case B ($Re = 2200$, $Ar = 2.5$) and Case C($Re = 1010$, $Ar = 2.5$), from left to right, upwind, SFCD, LU and experimental visualizations of Fujimura.

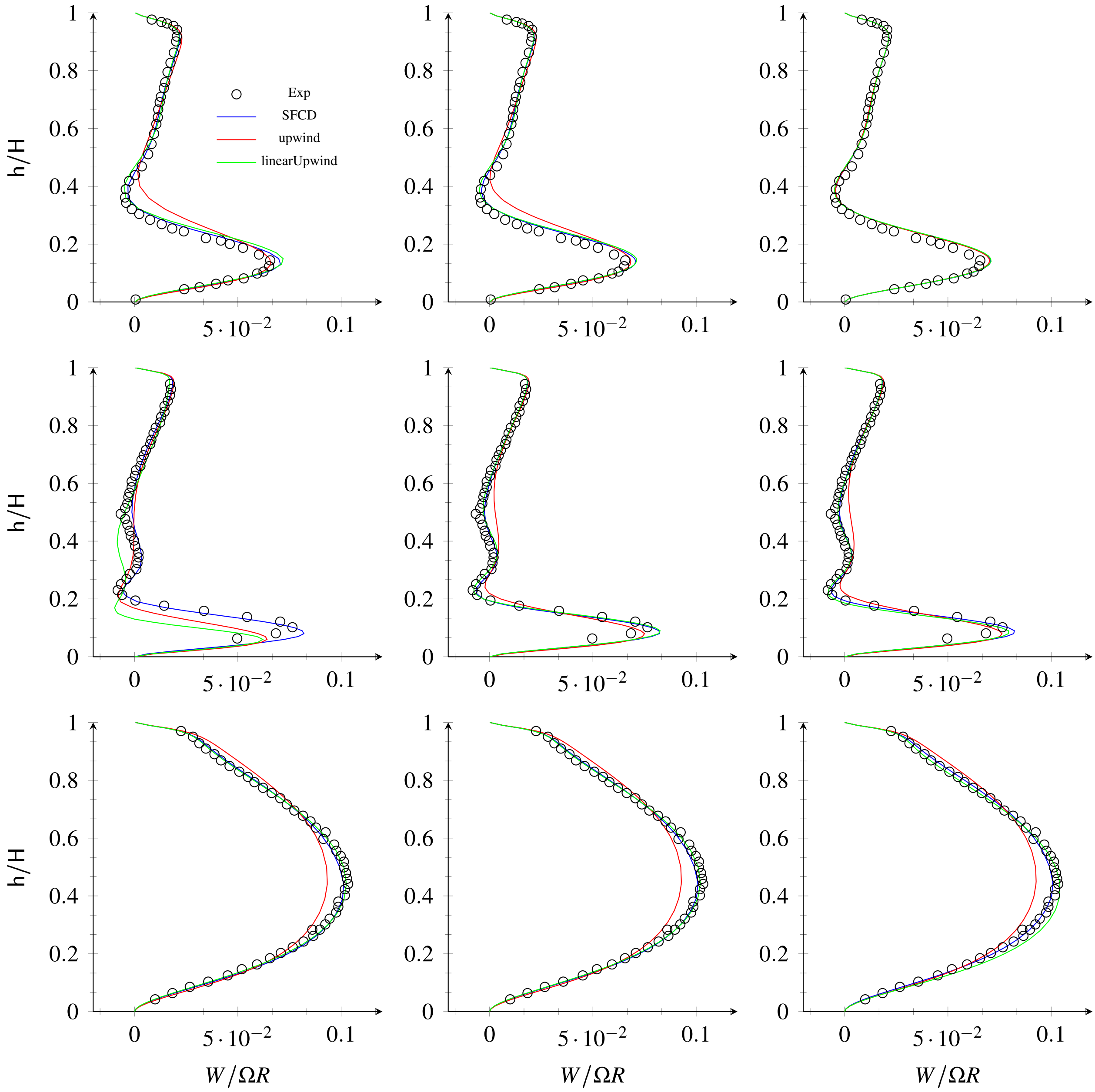

Fig. 7.5 Axial velocity along the centerline, from top to bottom, Case A, B and C. From left to right, coarse, medium and fine grid.

Table 7.1 upwind scheme.

Case	**Ar**	**Re**	**Grid size**	**Max velocity**	**Error %**	**Vortex breakdowns**
Exp_1	2.5	1010	-	0.103385	-	non
A_1	2.5	1010	1320	0.092695	10.3	non
A_2	2.5	1010	2352	0.092827	10.21	non
A_3	2.5	1010	4176	0.093279	9.78	non
Exp_2	1.5	1290	-	0.065676	-	1
B_1	1.5	1290	2204	0.070203	6.89	non
B_2	1.5	1290	2640	0.068319	4.02	non
B_3	1.5	1290	5104	0.065987	0.47	non
Exp_3	2.5	2200	-	0.076415	-	2
C_1	2.5	2200	2352	0.064115	16.096	non
C_2	2.5	2200	4640	0.074994	1.8595	non
C_3	2.5	2200	7800	0.076175	0.3140	non

Table 7.2 linearUpwind Scheme.

Case	**Ar**	**Re**	**Grid size**	**Max velocity**	**Error %**	**Vortex breakdowns**
Exp_1	2.5	1010	-	0.103385	-	non
A_1	2.5	1010	1320	0.10196	1.38	non
A_2	2.5	1010	2352	0.10251	0.846	non
A_3	2.5	1010	4176	0.10416	0.75	non
Exp_2	1.5	1290	-	0.065676	-	1
B_1	1.5	1290	2204	0.071912	9.50	1
B_2	1.5	1290	2640	0.071178	8.38	1
B_3	1.5	1290	5104	0.07086	7.89	1
Exp_3	2.5	2200	-	0.076415	-	2
C_1	2.5	2200	2352	0.062078	18.76	2
C_2	2.5	2200	4640	0.082545	8.02	2
C_3	2.5	2200	7800	0.079308	3.79	2

Table 7.3 SFCD Scheme.

Case	**Ar**	**Re**	**Grid size**	**Max velocity**	**Error %**	**Vortex breakdowns**
Exp_1	2.5	1010	-	0.103385	-	non
A_1	2.5	1010	1320	0.1012	2.54	non
A_2	2.5	1010	2352	0.10076	2.51	non
A_3	2.5	1010	4176	0.10079	2.11	non
Exp_2	1.5	1290	-	0.065676	-	1
B_1	1.5	1290	2204	0.070737	7.71	1
B_2	1.5	1290	2640	0.070666	7.60	1
B_3	1.5	1290	5104	0.070635	7.55	1
Exp_3	2.5	2200	-	0.076415	-	2
C_1	2.5	2200	2352	0.082251	7.64	2
C_2	2.5	2200	4640	0.082196	7.57	2
C_3	2.5	2200	7800	0.081964	7.26	2

7.2 Channel Flow in a U-Duct

The turbulent gas flows through a channel with a U-duct is characterized by a strong streamline curvature, which contains massive flow separation and reattachment on the inner wall of the duct. It is well known that the standard EVMs fail to accurately predict such flow features and thus this should also provide a severe test for the proposed model. Figure. 7.6 shows the computational domain used in the present study. Where the U-duct width is ($H = 0.0381m$), the inlet section is located at ($x = -10H$) and the outlet section at ($x = 12H$), with inner radius ($R_{inner} = 0.0191m$) and outer radius ($R_{outer} = 0.0572m$). This geometry is in accordance with the measurements of Monson et al. [90]. The grid is generated by using structured hexahedral elements, and a high resolution discretisation is applied near the wall with a y+ value less than 0.5. The total number of the grid cells is 40,600. A grid independence study was done on the mesh by doubling the number of grid points in each direction. This resulted in a negligible difference for all the primitive variables.

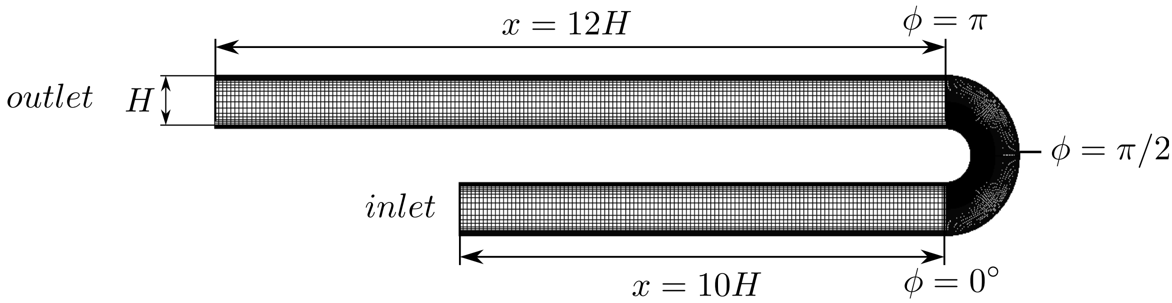

Fig. 7.6 Dimensional geometry of the channel duct with a U-turn.

7.2.1 Boundary Conditions and Numerical Scheme

The Reynolds number of the flow based on the channel width, H, and the mean flow velocity, U_m, is equal to $Re = 10^6$. The boundary conditions are specified as follows. At the inlet, the velocity profile is assumed to be fully developed turbulent velocity profile and zero gauge static pressure was specified at the outlet. No-slip conditions , $u = v = 0$, are specified at the solid wall boundaries. As the grid non-orthogonality is less than unity, a fully orthogonal scheme is used to discretize the diffusion terms, and second order linear scheme is used to discretize the convective terms.

7.2.2 Numerical Results

Along with the proposed model, the flow is also simulated with the use of the original and the modified one equation SA models, as well as with the two equations SST, $k-\omega$ and $k-\varepsilon$ models. The experimental measurements for the same geometry were reported in [90]. The data in Figs. 7.8-7.10 are presented using a local coordinate system where the x-axis is the streamwise direction, while the y-axis is the position in the direction normal to the walls. These data demonstrate the velocity profile and the turbulent quantities (Reynolds stresses and kinetic energy) within the U-duct at three cross-sectional positions; at the entrance of the bend $\theta = 0^o$, at the midway of the bend $\theta = \pi/2$ and at the end of the bend $\theta = \pi$.

As the flow passes the bend, the adverse pressure gradient is developed due to the curvature. At the upstream end of the bend, the lateral pressure gradient decreases, which in turn creates a massive separation zone near the inner wall. The prediction of this zone is challenging for the conventional EVMs turbulence models. The formation of the flow separation is visualized in Fig. 7.7 for different EVM models, with and without the rotation correction function. Table 7.4 summarizes the length of the separation zone which starts at the position π indicated in Fig. 7.6. Only the models sensitized to rotation-curvature corrections successfully capture the length of this separation zone.

The flow behavior encounters a dramatic changes as it passes through the bend. For example, in the first half of the bend, from $\theta = 0$ deg to $\theta = \pi/2$, the flow accelerates near the inner-wall and decelerates as it moves toward the outer-wall. As a result, the velocity profile at the entrance of the bend is more likely to take an asymmetric pattern. Figure. 7.8a shows that, all the EVM models accurately predict the velocity profile and it shows a lack of any significant advantages of the sensitized model over the conventional ones. Figure. 7.8b demonstrates the extreme situation of the asymmetric pattern of the velocity profile, where

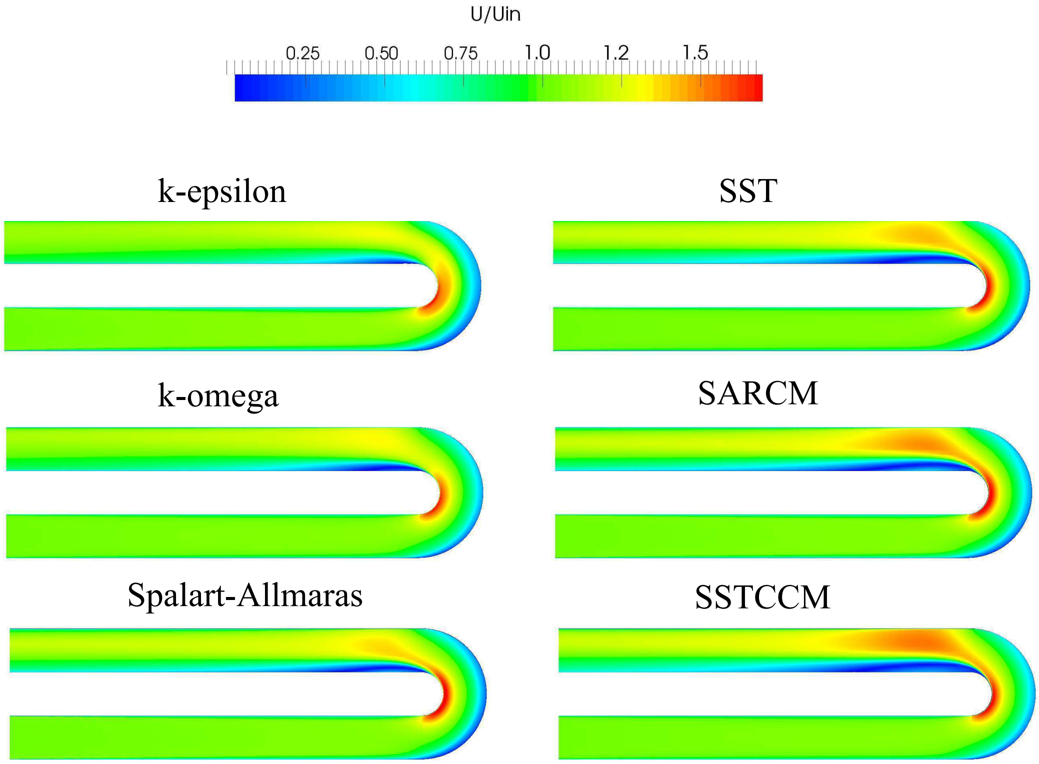

Fig. 7.7 Contour plots of the mean velocity of the flow within the u-duct for different EVM models.

the velocity reaches its minimum value near the outer wall and maximum value near the inner wall. In the second half of the bend, from $\theta = \pi/2$ to $\theta = \pi$, the curvature of the bend causes a tremendous impact on the turbulence. Moreover, flow pattern starts to reverse, and thus, the velocity decreases near the inner wall and increases near the outer wall. The effects of the curvature on the flow field cannot not be predicted by the conventional EVMs. This can obviously be observed in Fig. 7.8 (c), where the conventional EVMs underpredicted the velocity profile near the outer and the inner wall. On the other hand, the SSTCCM model accounts for the effects of the curvature of the inner and the outer walls better than the conventional models.

Figures. 7.9 and 7.10 show the Reynolds shear stress $\overline{u'v'}$ and the corresponding turbulent kinetic energy K, at the selected positions as in the velocity profile figures. It should be noted that K data is not given for both the standard and the modified SA models, since it is not explicitly computed in the SA turbulence model. The inner (convex) and the outer (concave) curvatures have had significant impacts on the turbulence quantities. While the convex curvature causes a reduction in the turbulence quantities, the concave surface causes opposite effects and increases both $\overline{u'v'}$ and K near the outer wall. This can be seen clearly at the 90 deg position midway of the bend. Although the velocity profiles at the this position for all the conventional EVMs are in a good a agreement with the data, none of the models predicts the turbulence quantities near the inner and the outer wall. On the hand, the SSTCCM model provide significant improvements and shows the ability to account for the strong curvature of both the inner and the outer wall. In addition to that, the sensitized models predict the location as well as the length of the separation zone better than some of the conventional EVMs. For example, from Fig.7.11 and Table.7.4, the most commonly used $k-\varepsilon$ model fails to capture the formation of the flow separation, the rest of the models underestimate the length as well as the height of the separation zone. However, both of the sensitized models (SARCM and SSTCCM) are the closest to the experimental data.

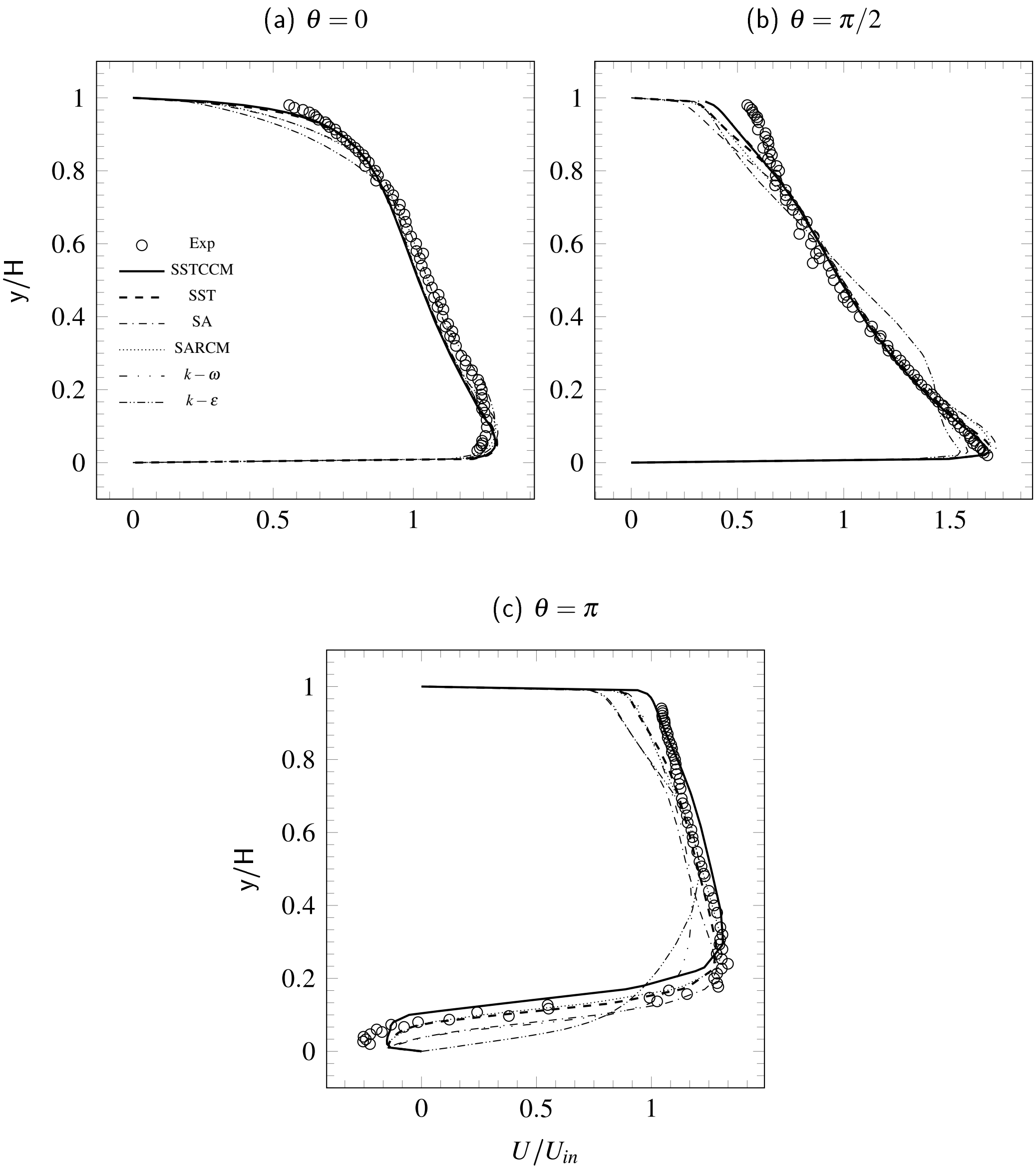

Fig. 7.8 Velocity profile at $\theta = 0$, $\theta = \pi/2$ and $\theta = \pi$; comparison between the EVMs simulation and the LDA measurements of Monson et al [90].

Table 7.4 Location and length of the flow separation in the duct with a u-bend

	$k-\varepsilon$	$k-\omega$	**SA**	**SST**	**SARCM**	**SSTCCM**	**Exp [90]**
location	-	π	π	π	π	π	π
length(x/H)	-	0.4	0.54	0.8	1.15	1.78	1.5

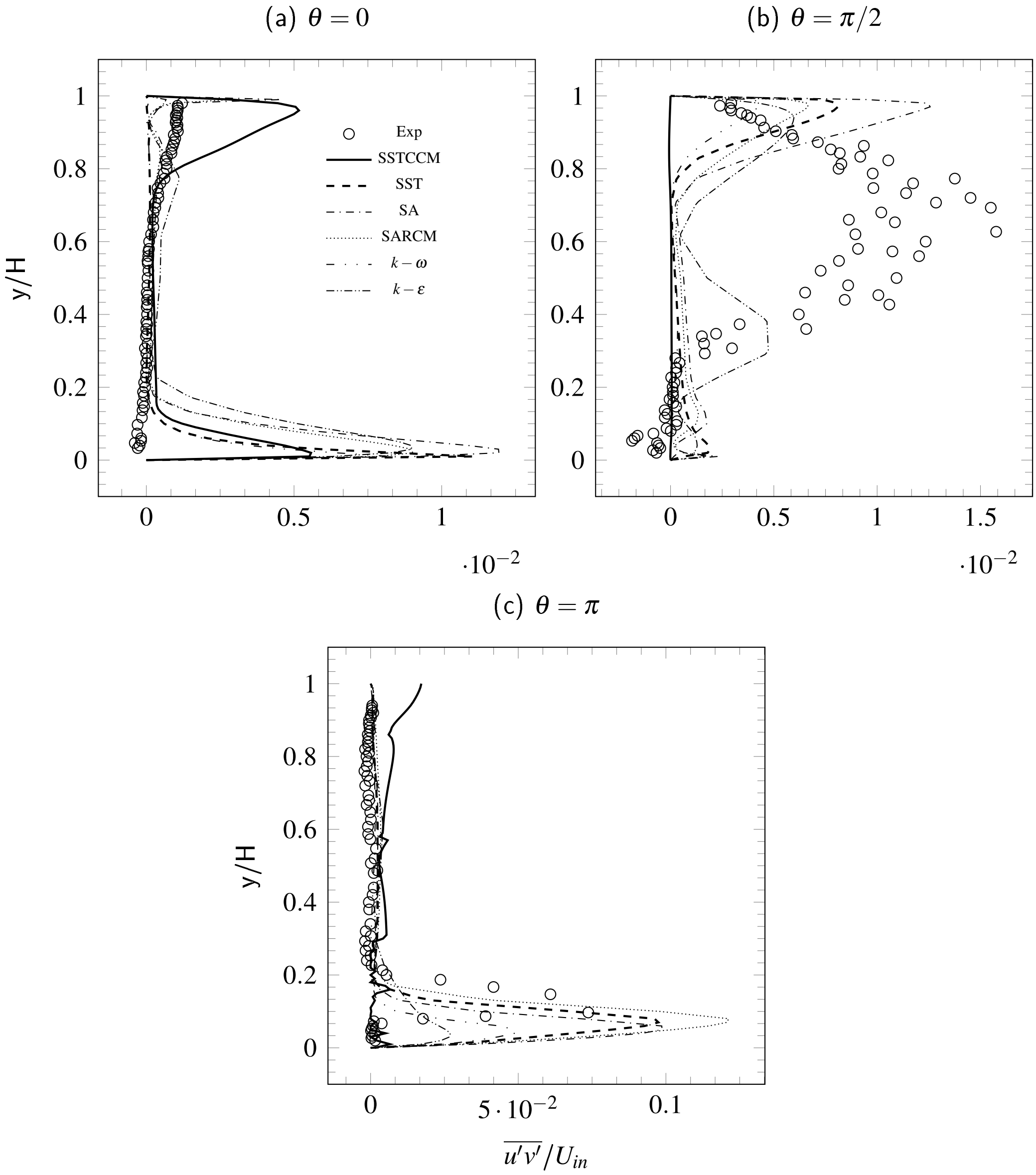

Fig. 7.9 Reynolds shear tresses profile at $\theta = 0$, $\theta = \pi/2$ and $\theta = \pi$; comparison between the EVMs simulation and the LDA measurements of Monson et al [90].

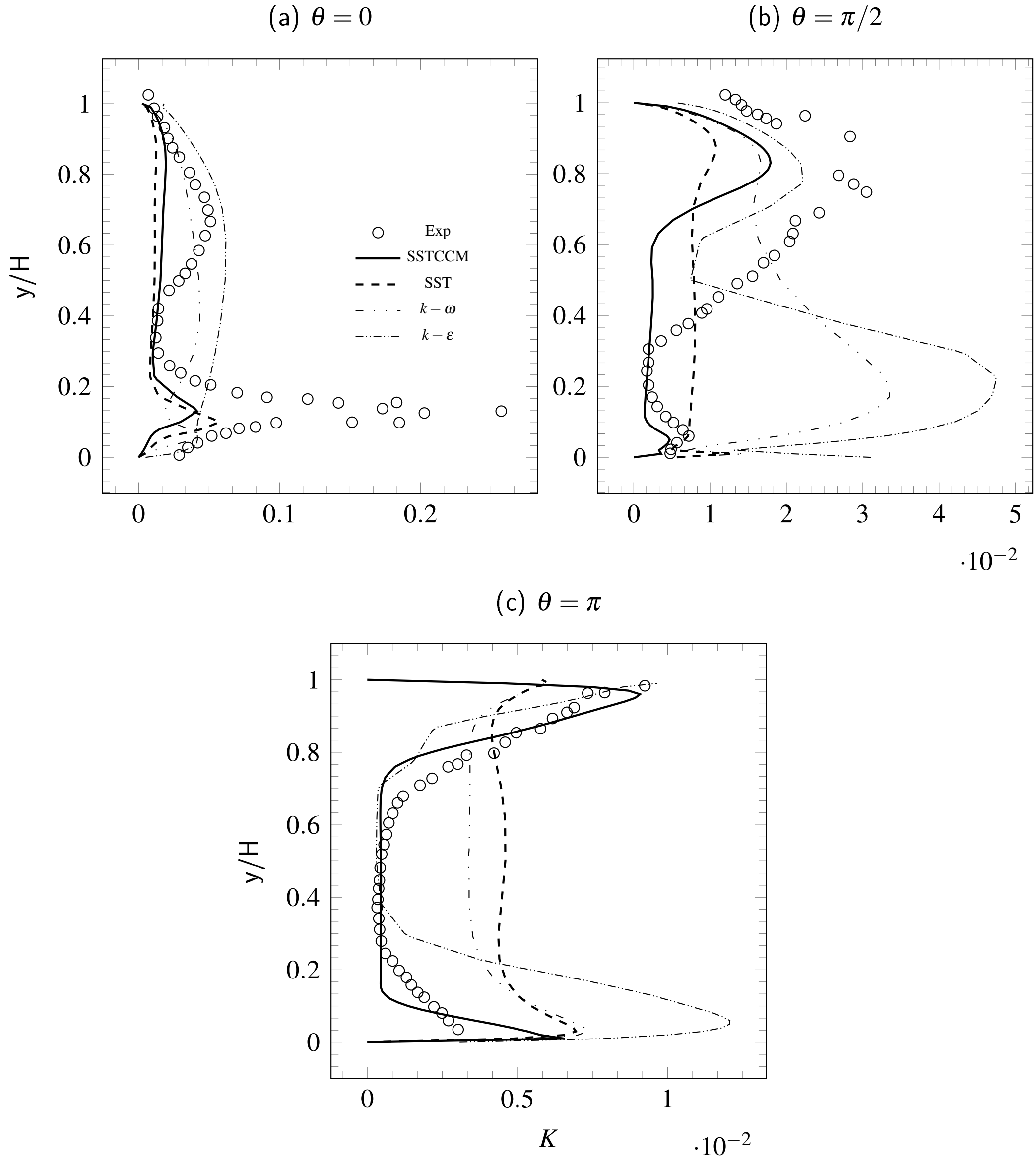

Fig. 7.10 Turbulent kinetic energy profile at $\theta = 0$, $\theta = \pi/2$ and $\theta = \pi$; comparison between the EVMs simulation and the LDA measurements of Monson et al [90].

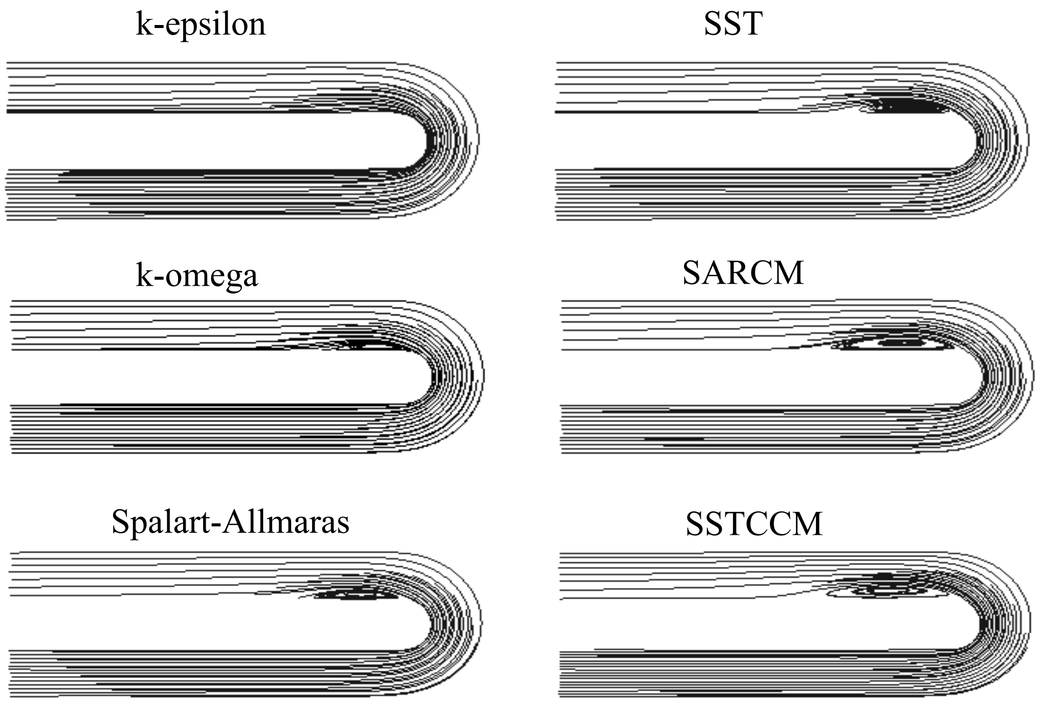

Fig. 7.11 Streamlines of the mean velocity of the flow within the u-duct for different EVM models.

7.3 Flow in the Cyclone Separator

The Stairmand cyclone design, which have been widely examined in the literature, is used to validate the ability of the proposed model to simulate high swirling flow. The calculations of the velocity field are compared to the experimental studies of Hoekstra [65], which is based on the Stairmand cyclone design. The numerical simulations are performed through the use of the SSTCCM model with four different numerical schemes and two grid types (structured and semi-structured). Both the top and apex outlets are extended to avoid large gradients normal to the outlet surfaces. The cyclone dimensions are given in Fig.7.12 and Table. 7.5.

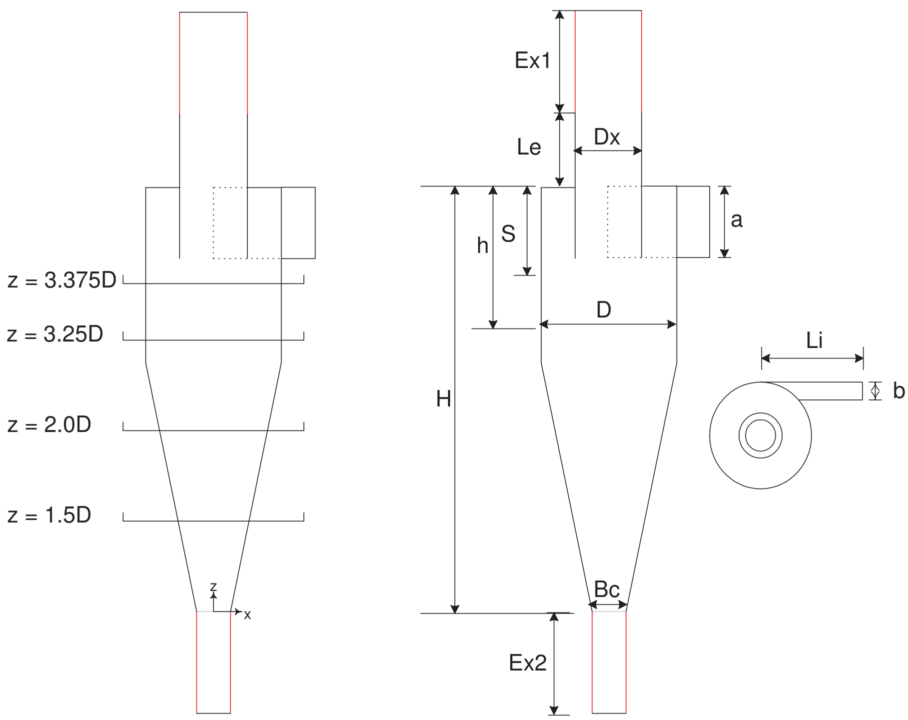

Fig. 7.12 Dimensional geometry of the cyclone design with the extended outlet shown in red.

Table 7.5 Geometrical dimensions of the tested cyclone

cyclone type	a/D	b/D	Dx/D	S/D	h/D	H/D	Bc/D	Ex1/D	Ex2/D	Li/D	Le/D
Stairmand	0.5	0.2	0.5	0.5	1.5	4.0	0.36	1	1	1	0.75

7.3.1 Grid generation

The computational cost as well as the accuracy of the solution depend on the quality of the computational grid. The meshing technique can employ a fully structured , unstructured or hybrid grid. The discretisation error arises due to the size and shape of the grid cells, while the numerical complexity depends on the grid resolution (the number of cells) and the quality of the mesh. The meshing of the complex geometries such as those representing cyclones is challenging and the fully structured grids which are generally preferred require some extra treatment. The body of a cyclone consists of three dissimilar geometrical shapes, which are a conical frustum, a circular cylinder and a rectangular prism. The way in which these shapes are attached to form the cyclone body, makes the meshing process using fully structural hexahedrals extremely difficult. For example, even for a coarse mesh, this would yield a very dense grid area around the symmetry-axis, on the one hand, and high non-orthogonal faces on the other hand. For medium and fine grids, both the dense grid area and the level of the non-orthogonality increase dramatically. To handle this problem in the simulations presented in the following sections, the non-orthogonal corrector which forms a part of PIMPLE algorithm is applied to rectify calculations and consequently to improve the accuracy (see Section 4.3.1.3). This procedure is realised on the mesh produced using an open source Gmsh-2.8.6 code [50].

Three numerical simulations were carried out based on different grid sizes. Table 7.6 summarizes the selection of meshes used for the gird independence study. The finest grid makes an insignificant improvement but produces a large number of non-orthogonal faces. These faces unnecessarily increase the computational effort as they require additional non-orthogonal correctors in the internal loop within each time step. All of the numerical results presented in Sections (7.3.3), (7.3.4) and (7.3.5) are performed through the application of the medium grid size.

Table 7.6 Dimensionless pressure drop of different grid sizes.

	Euler No	**No. elements**	**non-orthogonal faces**	**No orthogonal corrector**
Experiment	5.1	-	-	-
Coarse	3.48	131,308	501	1
Medium	4.88	203,414	599	2
Fine	4.968	328,868	1218	4

7.3.2 Boundary Conditions

As mentioned earlier, the cyclone operates at a range of $Re = 10^5$ to 10^6. The Reynolds number of the flow within the cyclone separator is based on the cyclone body diameter, D, the fluid dynamic viscosity, $\nu = 2.11 \times 10^{-5}$, and the inlet mean flow velocity , U_{in}, and is equal to $Re = 1.37 \times 10^5$. The flow was assumed to be fully developed, so, the corresponding inlet profiles of velocity and the turbulent flow quantities are obtained from preliminary computations of fully developed turbulent flow in a plane 3D channel. Dirichlet boundary conditions for the velocity are applied at the inlet and fixed walls, while Neumann boundary conditions are applied at both outlets [33]. The numerical set up of the boundary conditions is summarized in Table. 7.7.

Table 7.7 Set up of the cyclone boundary conditions.

Boundary	**U (m/s)**	**p** (m^2/s^2)	**k** (m^2/s^2)	**omega (1/s)**	ν_t (m^2/s)
Inlet	(10 0 0)	zero gradient	0.2413	11.4	2.11E-02
Outlet	zero gradient	0^5	zero gradient	zero gradient	zero gradient
Apex	zero gradient	0^5	zero gradient	zero gradient	zero gradient
wall	(0 0 0)	zero gradient	0	6.61112E+04	0

7.3.3 Swirling Flow and Turbulence Model

It was found that the ability to correctly reproduce the flow at a horizontal cross section is the most sever test for turbulence models and consequently important criterion for their selection. The models that passed the u-duct channel flow test were subsequently examined at this critical horizontal section. This assisted in identification the best candidates in terms of turbulence models in further detail studies. In this section the values of the calculated velocities in the 3D Cartesian coordinate system frame are transformed into the tangential and the axial velocity components and are presented.

The tangential velocity profile in a cyclone separator is generally described by the Rankine vortex structure, which is a combination of a solid-body and a free-vortex rotation (see discussion and Fig.5.1 in chapter 5). For instance, in the core region, the flow is dominated by the solid-body rotation, while the free-vortex type of rotation appears in the outer region. From previous studies on wall bounded swirling flows, the conventional EVMs are known of their inability to predict the Rankine vortex profile (see e.g. [92], [112] and [46]). Figure 7.13a demonstrates the radial distribution of the tangential velocity in a standard Stairmand cyclone at $Z = 3.25D$. It presents the results of the simulations which are performed using different turbulence models, i.e. the standard SST model, the SARCM model and the proposed SSTCCM model. The obtained results are compared with the experimental measurements of Heokestra [65]. It is seen that only the SSTCCM model is able to predict the Rankine vortex pattern in accordance with the experimental measurements.

The standard SST model underestimates the radial distribution of the tangential velocity over the entire diameter of the cyclone. As the SST model is based on the Boussinesq hypothesis, where the turbulent viscosity is of a scalar nature, it fails to predict the full structure of the Rankine vortex patterns.

The one-equation SARCM model shows some improvements over the standard SST model. This can be seen in the core region, where the solid-body type of rotation is accurately predicted. However, this model is still unable to represent the free-vortex type of rotation.

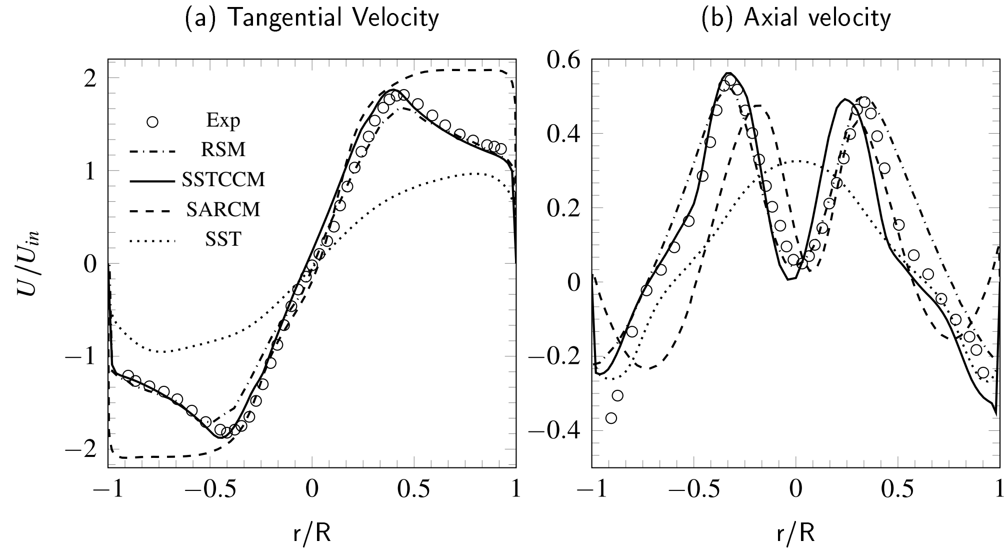

Fig. 7.13 Comparison of the tangential velocity profiles (a) and axial velocity profiles (b) between the LDA measurements, RSM and the EVMs simulations with and without the curvature correction.

Figure 7.13b demonstrates the radial distribution of the axial velocity profile. According to several publications ([70], [114] and [65]), the inverted W pattern of the axial velocity in cyclone cannot be predicted when the modeling assumptions are based on the EVMs. The SST model is consistent with these studies and fails to capture the axial velocity profile. On the other hand, both the SARCM and the proposed SSTCCM are capable of predicting the inverted W shape pattern. However, the shape of the axial velocity profile obtained with the SARCM model has a downward peak value located halfway between the vortex finder and the cyclone wall. This prediction is not confirmed by experimental results, which were reproduced using the proposed SSTCCM model. Also it underestimated the peak values of the upward axial velocity. On the contrary, the proposed model shows a significant improvement in predicting all three regions composing the axial velocity profile in cyclone. The downward direction which starts and ends at the edge of the vortex finder. The two upward direction regions which occur between the body wall and vortex finder wall. Both the locations and the magnitudes of these three profiles are accurately presented by the SSRCCM model.

7.3.4 Sensitivity of the Outlet Boundary Conditions on the Flow

The boundary conditions at the apex outlet affect the accuracy of the obtained solution significantly. This is a consequence of two key factors; 1) high possibility of large gradients zone in the direction normal to the apex outlet, 2) outlet back-flow which could interfere the flow inside the domain. Figure 7.14 shows the contour plots of the primitive variables (the velocity components and the static pressure) in the standard and the extended geometry. This alternative geometry is extended by attaching a cylindrical element of length twice the body diameter of the cyclone at the end of the apex. This extension is necessary so that the numerical results could be compare with the available experimental results in [65] The effects of the outlet boundary conditions in these two geometries are manifested in a different character of the flow variables. For instance, the tangential velocity contour shows that the standard and the extended geometry preserve the Rankine pattern of the swirl velocity throughout the cyclone body. On the other hand, there is a dramatic change in the contour of the axial velocity between these two geometries.

Figure 7.15 shows the tangential velocity profile at different longitudinal levels. The Z-locations of these levels are presented in Fig. 7.12 and are consistent with the measurements reported in [65]. The readings are taken at two cross-sectional levels inside the barrel portion and at two levels inside the conical portion. Although the application of the proposed model with the Neumann boundary conditions to the standard geometry preserves the Rankine pattern of the tangential velocity, the profile of the solid-body rotation is less accurate when compare to the extended one with the same boundary conditions.

In Fig. 7.16 the axial velocity profile of these two geometries are presented. It is found that the effect of the outlet boundary conditions on the axial profile is more significant in the conical portion. The obtained results presented in Fig. 7.16c and 7.16d show that both geometries inside the separation section are in a good agreement with the experimental data. However, the normal geometry provides an inverted V pattern profile in the conical section as shown in Fig. 7.16a and 7.16b. On the other hand, extending the outlet apex

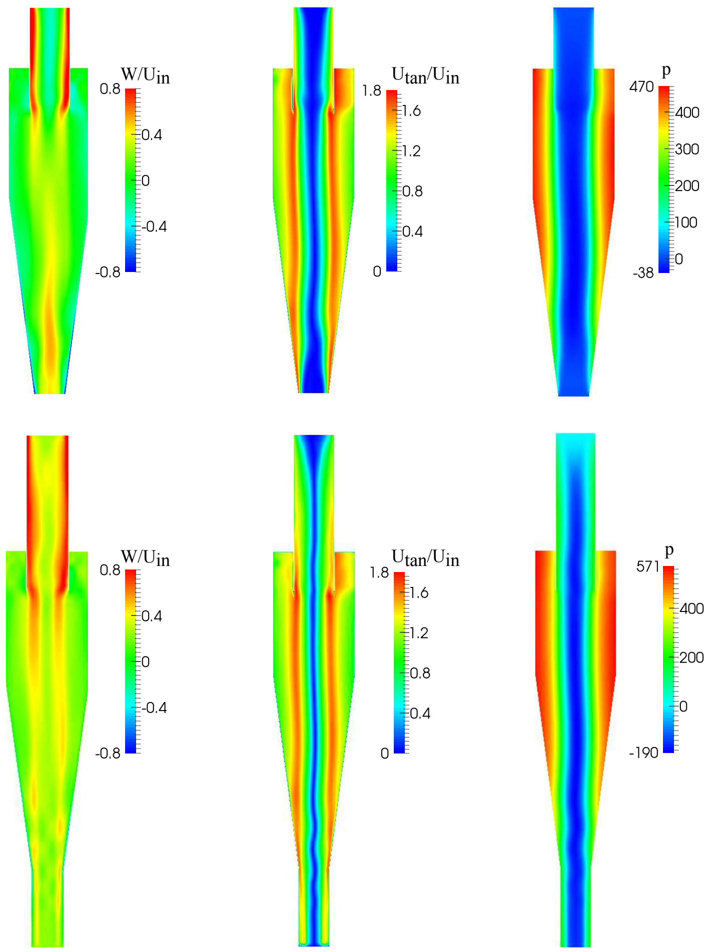

Fig. 7.14 Contour plots of the flow variables at sections Y = 0. At the top the standard Stairmand cyclone and at the bottom the extended outlet. From left to right; the axial velocity, tangential velocity and the static pressure.

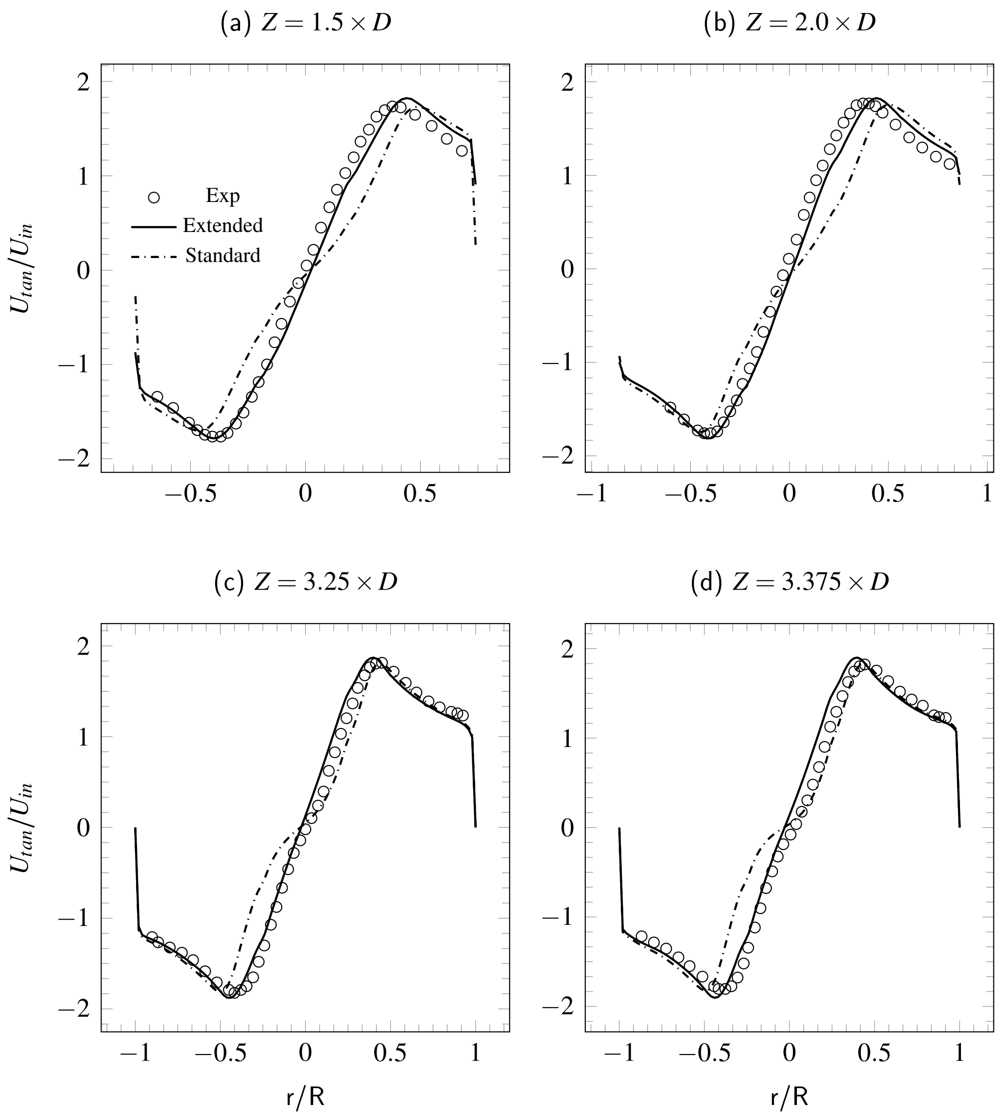

Fig. 7.15 Comparison of the tangential velocity profiles between the extended and standard geometry at different cross-sectional levels.

further reduces the effects of the applied boundary conditions at the apex surface. This is a necessary step to reduce the influence of the boundary conditions on the flow character and to assure that the same physical behaviour takes place both in experimental and numerical tests. This guarantees that the profile of the axial velocity component with the inverted *W* pattern is observed at both cross sections inside the conical part of the device.

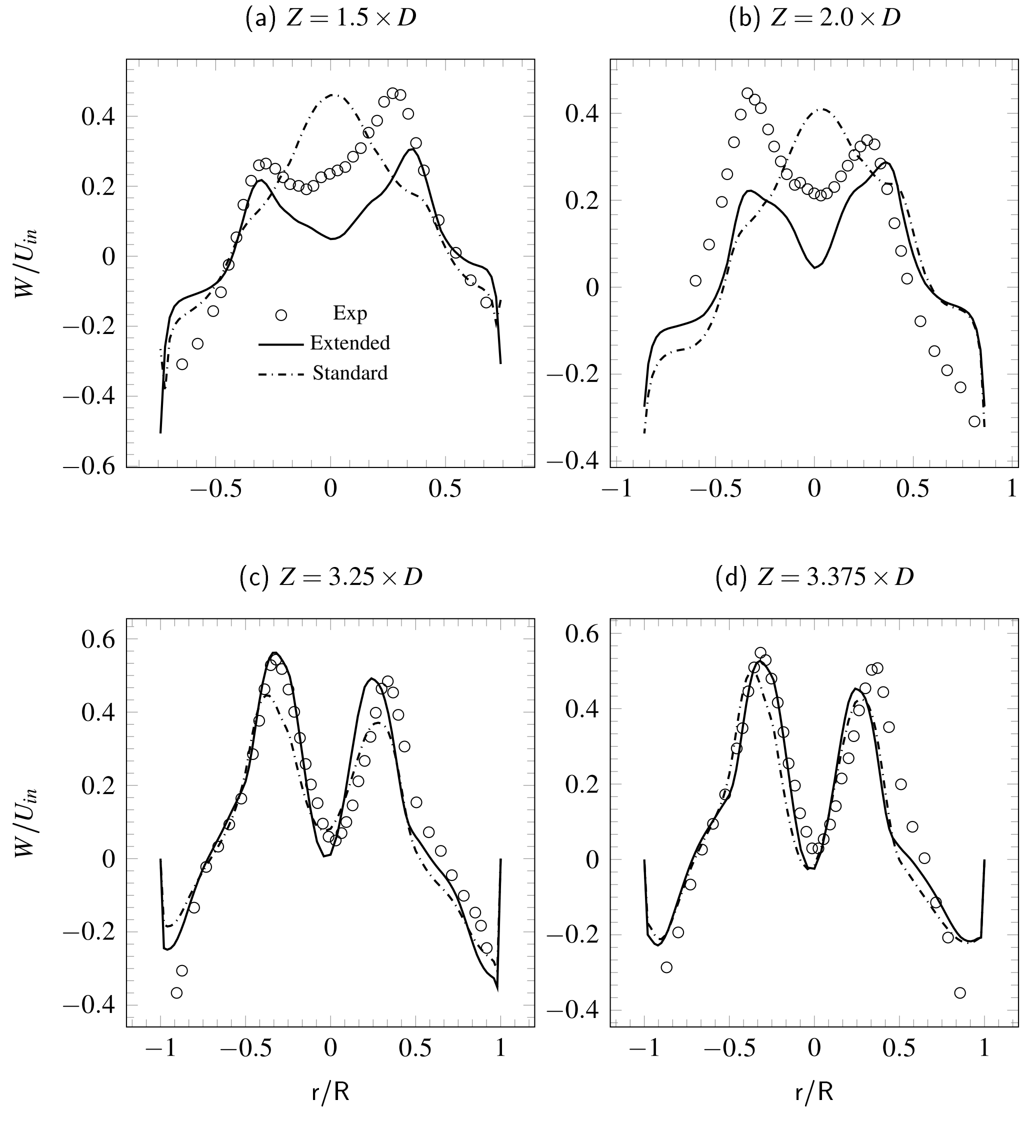

Fig. 7.16 Comparison of the axial velocity profiles between the extended and standard geometry at different cross-sectional levels.

7.3.5 Numerical Discretisation Schemes

Four numerical schemes are tested on the Stairmand cyclone design; namely, the LLU, the LU, the SFCD and the upwind schemes. The computational grid was based on structured hexahedral mesh with 203,414 elements. The results showed that the numerical scheme has significant effects on the accuracy of the solution. The contour plots presented in Fig. 7.18 show that only the LU scheme can predict the pattern of the tangential velocity profile throughout the longitudinal length of the cyclone. Then, comparisons of the velocity components at a horizontal cross-section below the vortex finder, at z = 3.25D, were made to assess the ability of the proposed model with regard to the flow character. The values of the calculated velocities in the Cartesian coordinate system frame are transformed into the tangential and axial velocity components and are presented in Fig. 7.17. The numerical simulations based on the second order LU scheme show a significantly improved prediction of the Rankine vortex profile when compared with the LDA measurement of Hoekstra [65]. However, in the conical part of the cyclone, the predictions of the axial velocity are less accurate than those for the tangential ones. The inaccurate prediction of the axial velocity profile may be linked to the sensitivity of the OpenFoam solvers to the face orthogonality. As discussed in section (6.4), the structured mesh suffers from a high level of non-orthogonal faces, which has a direct influence on both the stability and the accuracy of the flow field. Therefore, a semi-structured mesh is used to address how far the non-orthogonality faces affect the accuracy of the solution.

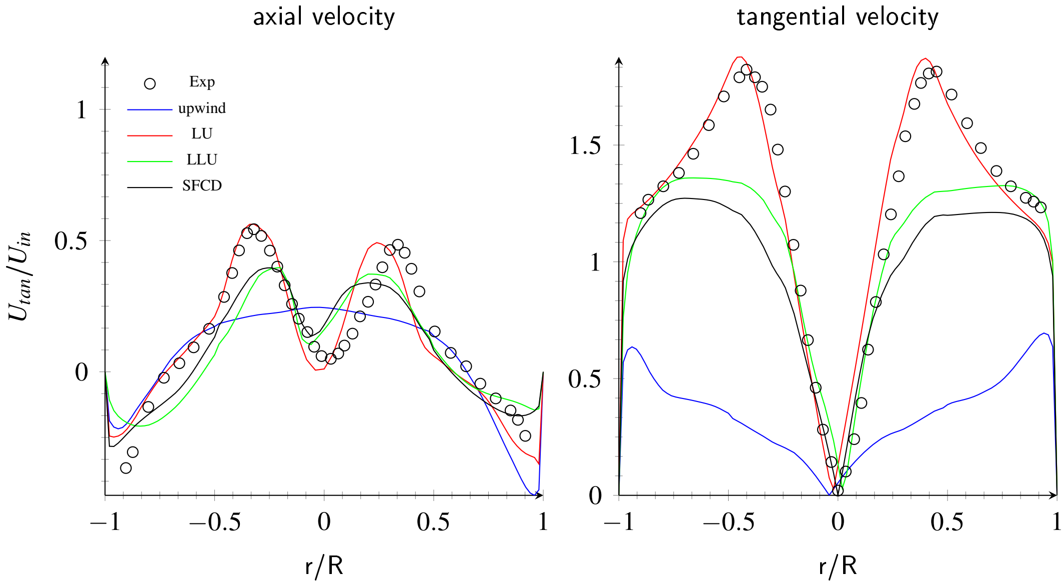

Fig. 7.17 Comparison of the axial and the tangential velocity profiles just below the vortex finder at $z = 3.25D$.

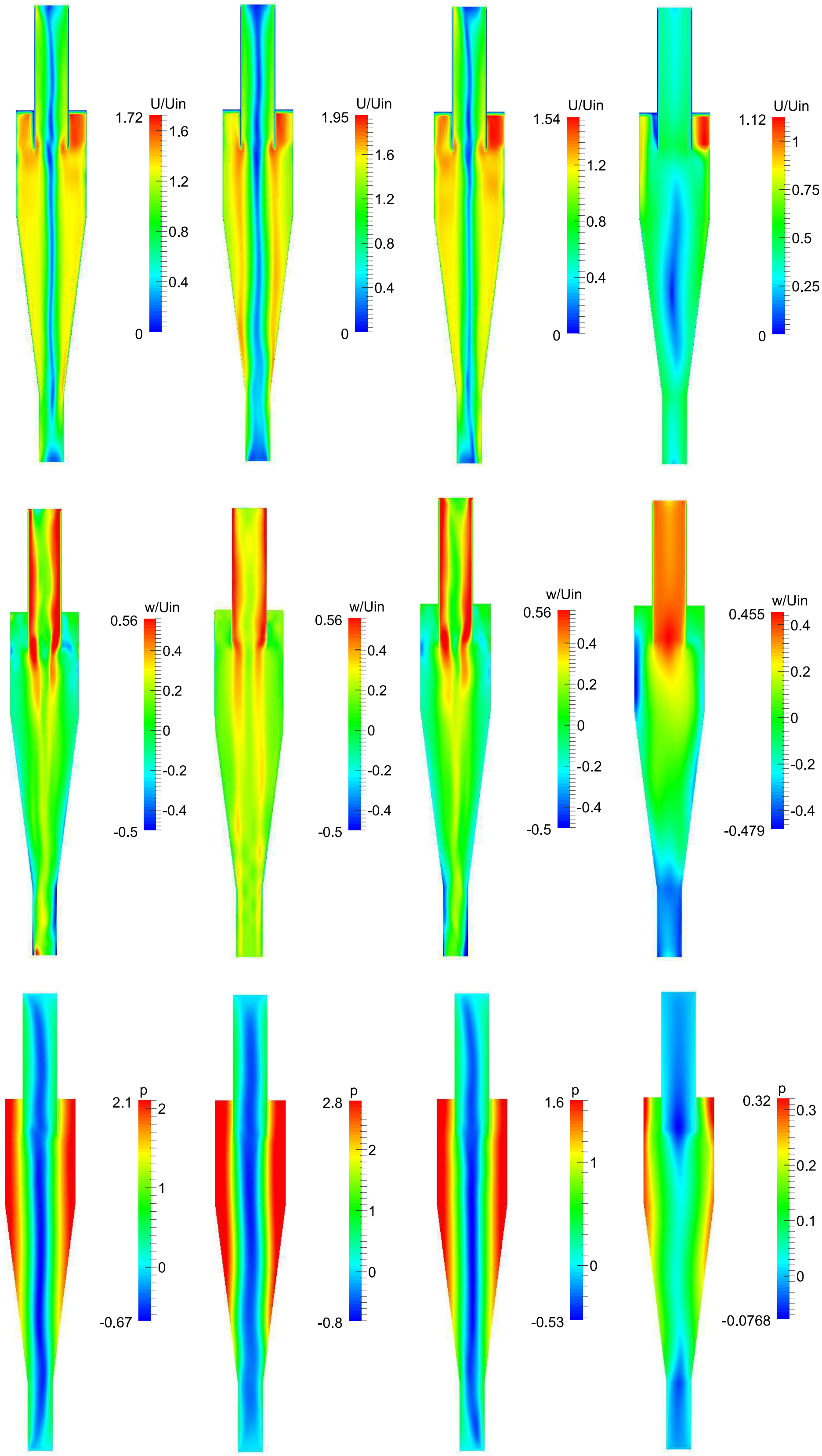

Fig. 7.18 Contour plots for the normalized time averaged flow variables at sections Y = 0. From top to bottom; tangential velocity, axial velocity and static pressure. From left to right; LLU, LU, SFCD and upwind scheme.

7.3.6 Structured Vs Semi-Structured Grid

Unlike the fully structured grid, the semi-structured type of grid is very difficult to generate, and tends to be quite complex and time consuming. However, the advantages of this grid type over the structured one are that: 1) it contains fewer non-orthogonal faces with a lower angle, and, 2) it is flexible so that the dense mesh around the central longitudinal axis is easy to control. Consequently, the number of the non-orthogonal corrector is lower, and hence less computational time is required. In addition, inside the core region, the structured grid produces very small elements (as shown in Fig. 6.3), which in turn lead to a very high Co number at the cell level in this area. The sudden expansion of the Co number eventually leads to a floating point that blows up the solver after a few time steps. In order to preserve the stability of the solver, a very small time step was used when implementing the structured type of grid. For instance, in order to keep the Co number below unity, a time step of 1.0E-5 was selected in the case of a structured grid, while a larger time step of 1.0E-4 is used for the semi-structured grid.

The Stairmand cyclone design was selected to test the aforementioned grid types. The first grid was generated by using the Gmsh open source code, which produces a fully structured hexahedral elements. On the other hand, a hybrid or semi-structured grid was generated by implementing the SnappyHexMesh method, which is a built-in utility available in OpenFoam package (see Section 6.4).

Table.7.8 summarizes the parameters and the corresponding specific dissipation of the turbulent kinetic energy ω at the wall boundary for both grid types of medium size.

Table 7.8 Grid parameters and the corresponding turbulence variables.

Grid type	**No. elements**	**first cell height**	**y+ value**	**ω near wall**
Structured	203,414	2.831E-04	10.8	6.61112E+04
Semi-structured	197,821	2.540078E-04	10	7.77814E+04

Figure 7.19 demonstrates the radial distribution of the tangential velocity profile at cross-sectional levels shown in Fig. 7.12. In this figure, the size of the structural grid is identical to the medium grid size given in Table 7.6. Three grid densities of a hybrid type were examined and compared with the structured grid as well as experimental measurements. The coarser grid contains 101,707 elements, while the medium and dense ones contain 197,821 and 412,580 elements, respectively. The hybrid meshes require less turnaround time, because they do not require any correctors within each time step, as explained in chapter 6. However, it is found that the hybrid mesh is less accurate when compared to the fully structured grid. For instance, in the conical part of the cyclone, Figs. 7.19a, b and 7.20a, b show that neither the tangential nor the axial velocity are not matches the expected profiles. The hybrid fails to represent the full Rankine pattern, especially the free-vortex type of rotation. Also, it fails to predict the W pattern of the axial velocity profile in the narrower region of the conical part.

However, in the barrel portion of the cyclone, both the Rankine and the inverted W patterns are well presented but underestimated at the peak values. Further investigations of the hybrid method needs to be considered in future work. Due to these deficiencies, the performance study in the next section is limited to the fully structured grid.

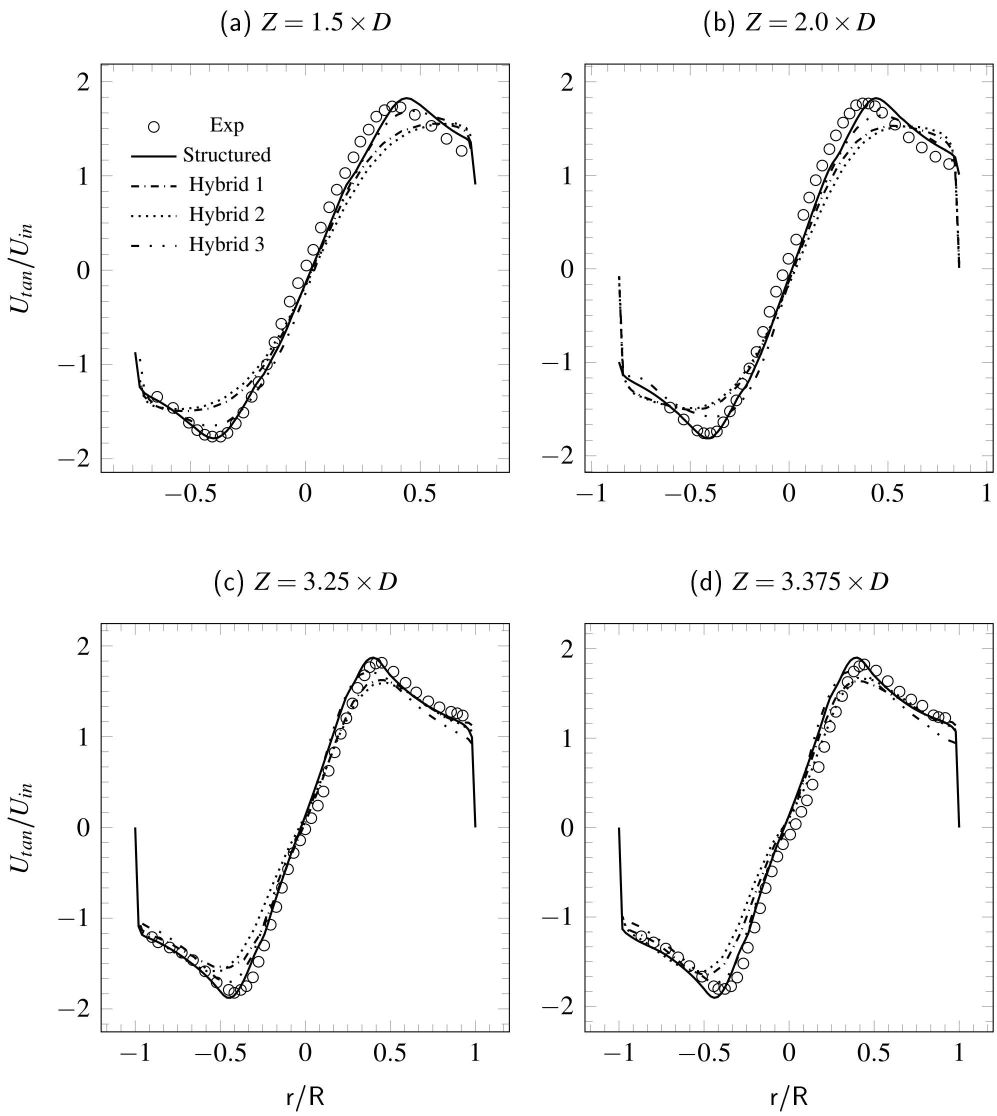

Fig. 7.19 Comparison of the tangential velocity profiles between the structured and hybrid mesh at different cross-sectional levels.

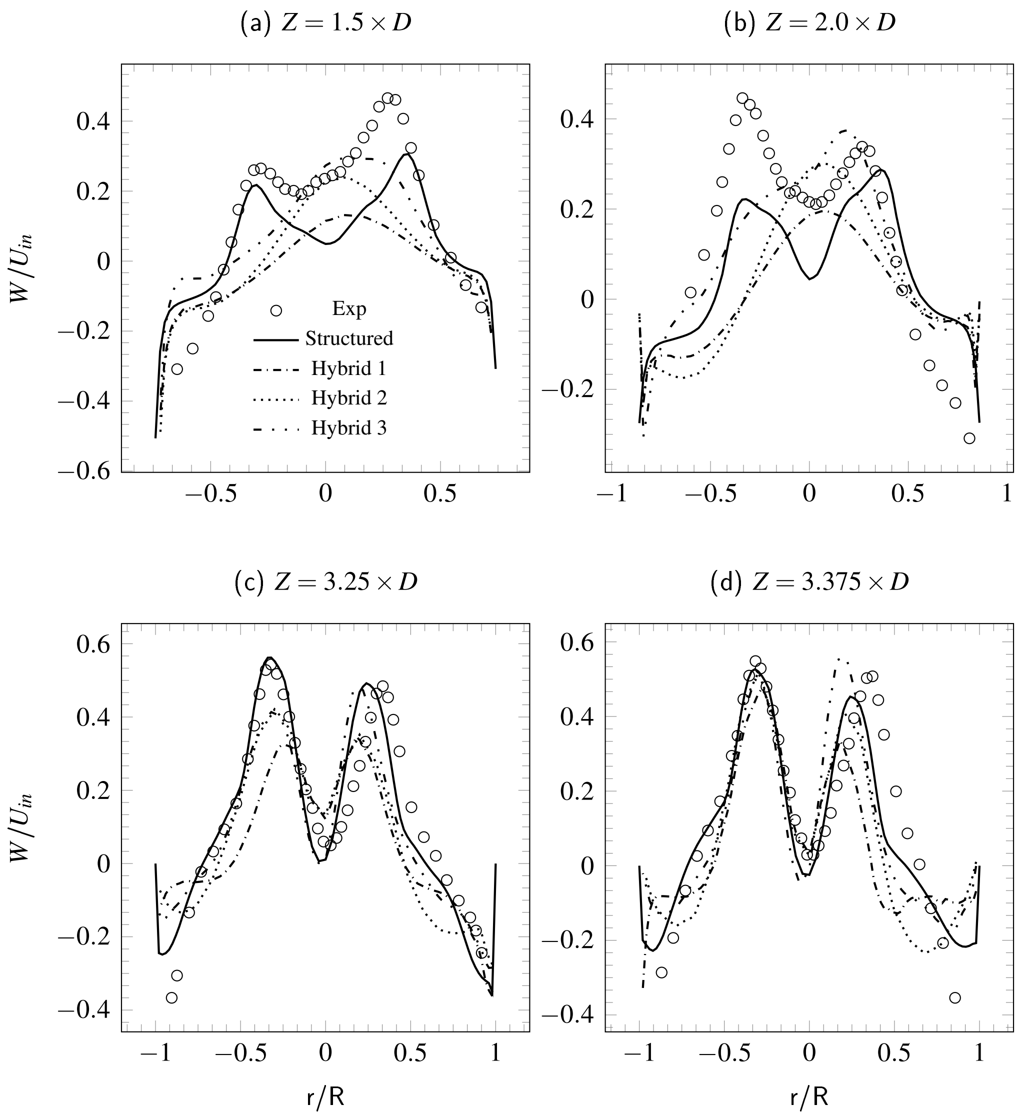

Fig. 7.20 Comparison of the axial velocity profiles between the structured and hybrid mesh at different cross-sectional levels.

7.3.7 Cyclone Performance and Efficiency

The efficiency of the cyclone separator is obtained by the measurement of two parameters, i.e, the collection efficiency and the pressure drop. The centrifugal force is the main factor that drives the particles toward the wall and then spiral down to the apex. From Newton's second law of motion, the magnitude of the tangential inlet velocity is proportional to the centrifugal force acting on the solid particles. On the contrary, the pressure drop and consequently the operational cost of the cyclone rises proportionally to the inlet velocity. Therefore, the present study focusing on accurately computing the swirling flow in cyclone is concluded by providing the performance information which is verified with the experiment as well.

The collection efficiency in this study is accounted by implementing the discrete phase modelling approach (DPM) to track the injected particles. The considered particles are of various sizes and the Rosin-Rammler technique [131] was applied for their initial distribution. The size of the injected particles are varies between $1 \times 10^{-5}(m)$ and $1 \times 10^{-7}(m)$. The mass fraction, Y_d, and the corresponding particles diameter are given in Table 7.9. The mean diameter was calculated from Fig. 7.21 and is approximately $3.4 \times 10^{-6}(m)$, while the average spread parameter is 1.675. The DPM was performed with the total flow rate of $0.001(kg/s)$ and the maximum number of steps was $200,000$.

Table 7.9 Pressure drop and the cut-off diameter of the proposed turbulence models and the experimental measurements.

Diameter Range (μm)	**Mass Fraction Range**	**Diameter, d (μm)**	**Mass fraction with diameter > d, Y_d**
0.1-1	0.05	1	0.95
1-1.5	0.1	1.5	0.85
1.5-2	0.35	2	0.5
2-5	0.3	5	0.2
5-7.5	0.15	7.5	0.05
7.5-10	0.05	10	0

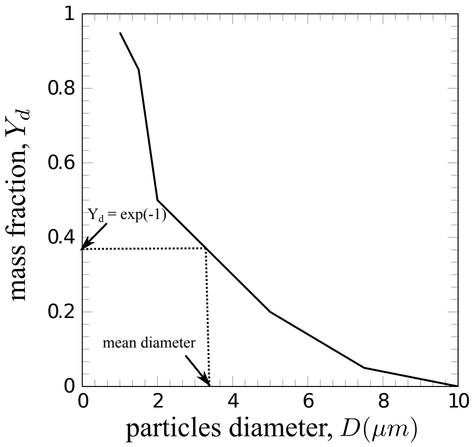

Fig. 7.21 Cumulative size distribution of particles.

The particles were injected from the inlet surface with velocity equal to the gas phase. The collection efficiency curve presented in Fig. 7.22 is drawn from the statistical data of the monitored particles. All particles that flow through the apex outlet are considered as collected particles, while the escaped particles are those flow through the top outlet. Some particles suspended inside the cyclone and recirculating near the top wall of the barrel part. Therefore, the efficiency, η, is calculated from relation given by equation (7.2). The cut-off size diameter of numerical results is approximately 2.39 (μm), which is reasonable compared to the 1.85 (μm) of the experimental calculation. Also, from chapter 6, the theoretical calculation of the critical diameter based on the Jones and Leith model is 1.8677 (μm).

$$\eta = \frac{trapped}{injected - suspended} \tag{7.2}$$

The total pressure drop in the cyclone device is a contribution of three major losses; losses in the inlet section, losses in the vortex finder and apex exit duct and losses resulting from the wall friction and irreversible losses within the vortex separation core. The latter has the major influence on the total pressure drop. The proposed model underestimated the pressure drop by approximately 8%. The dimensionless pressure drop (Euler number) and the cut-off diameter X_{50} of the experimental and the numerical results are depicted in Table 7.10.

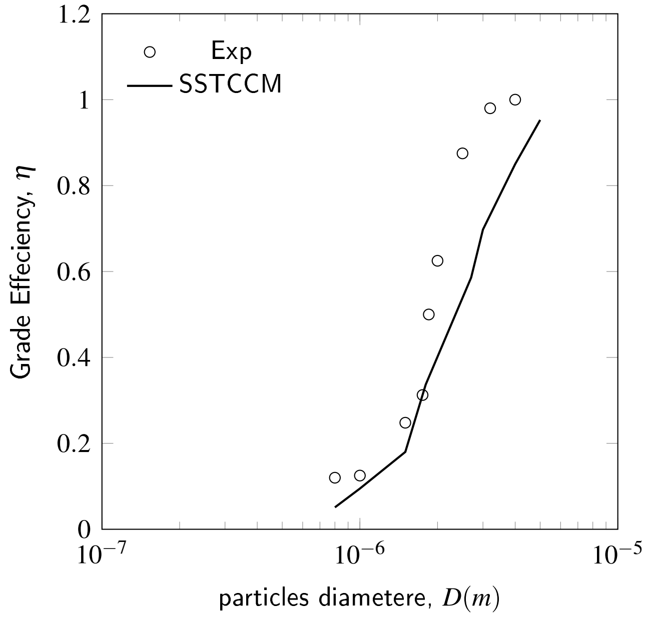

Fig. 7.22 Grade efficiency curve of the proposed SSTCCM model compared to the experimental measurement.

Table 7.10 Pressure drop and the cut-off diameter of the proposed turbulence models and the experimental measurements of Hoekstra [65].

	Euler number	$X_{50}(\mu m)$
Experiment	5.1	1.85
SSTCCM	4.8	2.39

Chapter 8

Conclusion and Future Work

8.1 Main Conclusions

It is widely believed that the EVM turbulence models are incapable of representing the physically correct simulation of the flow within cyclones. Hoekstra et al. [64], claimed that neither the tangential nor the axial velocity profile can be predicted using the EVMs models. This claim was supported by several numerical studies that have been conducted to investigate the flow within the cyclone separators. More specifically, if the flow exhibits a swirling motion, EVMs fail to represent the free-vortex rotation type at the peripheral part of the cyclone. This is attributed to the use of the Boussinesq hypothesis that assumes that the eddy viscosity is an isotropic scalar which is untrue for more complex flows such as cyclones. Therefore, the main objective of this work was to handle this weakness by modifying the SST turbulence model to account for the rotation and curvature effects.

Simulations of the turbulent flow through a 180 degree U bend and swirling flow in a confined cylinder with a rotating lid have been performed in order numerically to validate the proposed model. The results showed significant improvement of the proposed SSTCCM model over the conventional EVMs. Different numerical schemes were tested to address the sensitivity and accuracy of the proposed model when simulating swirling flows. Among the different first and second order schemes, it was found that the second order linear upwind scheme (LU) provided the best results. The preliminary 2D case studies allowed the author to narrow the selection of both the turbulence models and the numerical schemes. Three EVMs models (SSTCCM, SARCM and the standard SST) were implemented to simulate the swirling flow in the Stairmand high efficiency cyclone. The proposed model showed significant improvements in predicting the axial and tangential velocity profiles at different cross-sectional levels. The SARCM model, which is based on the one-equation SA model, showed some improvements when compared to the conventional SST model. These improvements occurred in the core region, where the solid-body type of rotation is expected. Also, it succeeded in representing the W patter of the axial velocity profile. The deficiencies of the SARCM are that this model is incapable of representing the free-vortex tape of rotation and that it underestimated the peak values of the axial velocity profile.

The result of this work also confirmed the previous observation regarding the importance of a proper set up of the boundary conditions. The earlier observations were supported by the simulations in which the finite element method was applied [33]. Within the context of the finite element method, one can directly impose the natural boundary conditions of the Neumann type involving forces. The explicit boundary conditions for forces in a mathematical formulation of the finite volume method proved impossible. Therefore, in the present work, it was necessary to apply other measures, relying on extending the exit outlet by including an additional cylindrical part, to guarantee physically meaningful boundary conditions. It was shown in the presented tests that the axial and tangential velocity profiles are highly sensitive to the applied boundary conditions. The problem of correctly imposed boundary conditions remains a challenge and has been frequently neglected in the published work. This is especially clear in the simulation based on commercial software. The thesis highlighted the importance of this problem.

The flow in the cyclone separator was also studied using two different grid types. The results reinforced the view that (in the context of the finite element method), the W pattern of the axial velocity profile can only be achieved when the flow domain is discretized based on the structural hexahedral elements. Although the semi-structured mesh is more efficient in terms of computational resources, the readings of the velocity components (the axial and tangential) are less accurate than with the full structured grid. This study also emphasizes that the numerical discretization of the flow governing variables should be of a higher order. The study showed that even for the scalar turbulent quantities the first order schemes are inadequate for complex flows such as the cyclone.

8.2 Recommendations for Future Work

As recommendations for future work, the proposed SSTCCM model will be implemented to investigate the flow field on a cyclone device with a vortex diameter less than half of the cyclone body. For this type of cyclone, the axial velocity profile takes the shape of an inverted V pattern. Then the tangential as well as the performance parameters will be compared to the available experimental data. In addition, the SSTCCM model will be tested under several operating conditions and swirling numbers.

List of Published Work

- **Conference Paper** 1. Alahmadi, Y and Nowakowski, A. F. (2013). The numerical simulation of swirling flow in liquid-solid hydrocyclones. In *8th International Conference on Multiphase Flow (ICMF 2013)*.

- **Journal Paper (submitted)** 1. Alahmadi, Y and Nowakowski, A. F. (2015). Modified shear stress transport model with curvature correction for prediction of swirling flow in a cyclone separator.

References

[1] Alexander, R. M. (1949). Fundamentals of cyclone design and operation. *Proc Australas Inst Min Metall*, 152(3):152–153.

[2] Altmeyer, S., Mathieu, V., Jullemier, S., Contal, P., Midoux, N., Rode, S., and Leclerc, J.-P. (2004). Comparison of different models of cyclone prediction performance for various operating conditions using a general software. *Chemical Engineering and Processing: Process Intensification*, 43(4):511–522.

[3] Amano, R. and Sundén, B. (2011). *Computational Fluid Dynamics and Heat Transfer: Emerging Topics*, volume 23. WIT Press.

[4] Anderson, J. (1995). *Computational Fluid Dynamics: The Basics with Applications*. McGrawhill Inc, New York, US, international edition.

[5] Association, B. C. U. R. (1963). *BCURA Monthly Bulletin*. Number v. 27. British Coal Utilisation Research Association.

[6] Avci, A. and Karagoz, I. (2001). Theoretical investigation of pressure losses in cyclone separators. *International Communications in Heat and Mass Transfer*, 28(1):107–117.

[7] Barakat, H. and Clark, J. (1966). Analytical and experimental study of the transient laminar natural convection flows in partially filled liquid containers. *Proceedings of the Third International Heat Transfer Conference*, 2:152–162.

[8] Barth, W. (1956). Design and layout of the cyclone separator on the basis of new investigations. *Brenn. Warme Kraft*, 8:1–9.

[9] Baskakov, A., Dolgov, V., and Goldobin, Y. M. (1990). Aerodynamics and heat transfer in cyclones with particle-laden gas flow. *Experimental Thermal and Fluid Science*, 3(6):597–602.

[10] Basu, P. (2006). *Combustion and Gasification in Fluidized Beds*. CRC press, Boca Raton, USA.

[11] Bernard, J., Andries, J., Scarlett, B., and Pitchumani, B. (1990). Cyclone performance at high temperatures and pressures. In *Proceedings of 5th World Filtration Congress, Nice, France*, volume 2, pages 510–515.

[12] Blazek, J. (2015). Chapter 3 - principles of solution of the governing equations. In Blazek, J., editor, *Computational Fluid Dynamics: Principles and Applications (Third Edition)*, pages 29 – 72. Butterworth-Heinemann, Oxford, third edition.

[13] Boris, J. P. and Book, D. L. (1973). Flux-corrected transport. i. shasta, a fluid transport algorithm that works. *Journal of Computational Physics*, 11(1):38–69.

[14] Bose, P., Roy, K., Mukhopadhya, N., and Chakraborty, R. (2010). Improved theoretical modeling of a cyclone separator as a diesel soot particulate emission arrester. *International Journal of Automotive Technology*, 11(1):1–10.

[15] Boussinesq, J. (1877). Essa sur latheories des eaux courantes, memoires presentes par divers savants a l'. *Academic des Sciences de l'Institut Nationale de France*, 23(1).

[16] Boysan, F., Ayers, W., and Swithenbank, J. (1982). A fundamental mathematical modelling approach to cyclone design. *Transactions of the Institution of Chemical Engineers*, 60(4):222–230.

[17] Briggs, L. W. (1946). Effect of dust concentration on cyclone performance. *Trans. Am. Inst. Chem. Eng*, 42(30):511–526.

[18] Casal, J., Martinez-Benet, J., and Valencia, E. (1989). Cálculo y diseño de ciclones. *Ingeniería Química. Madrid*, pages 115–124.

[19] Casal, J. and Martinez-Benet, J. M. (1983). Better way to calculate cyclone pressure drop. *Chemical Engineering*, 90(2):99–100.

[20] Chen, J. and Shi, M. (2007). A universal model to calculate cyclone pressure drop. *Powder Technology*, 171(3):184–191.

[21] Chen, L., Zang, J., Hillis, A., Morgan, G., and Plummer, A. (2014). Numerical investigation of wave–structure interaction using openfoam. *Ocean Engineering*, 88:91–109.

[22] Chou, P. Y. (1945). On velocity correlations and the solutions of the equations of turbulent fluctuation. *Quarterly of Applied Mathematics*, 3(1):38–54.

[23] Collins, G. (2003). *Fundamental Numerical Methods and Data Analysis*, volume 1. Harvard University Press.

[24] Cortes, C. and Gil, A. (2007). Modeling the gas and particle flow inside cyclone separators. *Progress in energy and combustion Science*, 33(5):409–452.

[25] Courant, R., Friedrichs, K., and Lewy, H. (1928). Über die partiellen differenzengleichungen der mathematischen physik. *Mathematische Annalen*, 100(1):32–74.

[26] Courant, R., Isaacson, E., and Rees, M. (1952). On the solution of nonlinear hyperbolic differential equations by finite differences. *Communications on Pure and Applied Mathematics*, 5(3):243–255.

[27] da Vinci, L. L. (2011). *The Notebooks of Leonardo Da Vinci, Vol. 2*. Courier Corporation.

[28] Davies, C. et al. (1950). The separation of airborne dust and particles. *Arhiv za Higijenu Rada*, 1(4):393–427.

[29] Davydov, B. (1960). On the statistical dynamics of an incompressible turbulent fluid. In *Soviet Physics Doklady*, volume 4, page 769.

[30] Dietz, P. W. (1981). Collection efficiency of cyclone separators. *AIChE Journal*, 27(6):888–892.

[31] Dirgo, J. and Leith, D. (1985). Cyclone collection efficiency: comparison of experimental results with theoretical predictions. *Aerosol Science and Technology*, 4(4):401–415.

[32] Dirgo, J. A. (1988). *Relationships Between Cyclone Dimensions and Performance*. PhD thesis, Harvard University, USA.

[33] Doby, M. J., Kraipech, W., and Nowakowski, A. F. (2005). Numerical prediction of outlet velocity patterns in solid–liquid separators. *Chemical Engineering Journal*, 111(2):173–180.

[34] Drikakis, D. and Rider, W. (2006). *High-Resolution Methods for Incompressible and Low-Speed Flows*. Springer Science & Business Media.

[35] Dyakowski, T. and Williams, R. (1993). Modelling turbulent flow within a small-diameter hydrocyclone. *Chemical Engineering Science*, 48(6):1143 – 1152.

[36] Elsayed, K. (2011). *Analysis and Optimisation of Cyclone Separators Geometry Using RANS and LES Methodologies*. PhD thesis, Vrije Universiteit Brussel.

[37] Elsayed, K. and Lacor, C. (2010a). Application of response surface methodology for modeling and optimization of the cyclone separator for minimum pressure drop. In *Fifth European Conference on Computational Fluid Dynamics (ECCOMAS CFD 2010), Lisbon, Portugal*.

[38] Elsayed, K. and Lacor, C. (2010b). Optimization of the cyclone separator geometry for minimum pressure drop using mathematical models and cfd simulations. *Chemical Engineering Science*, 65(22):6048–6058.

[39] Elsayed, K. and Lacor, C. (2011). The effect of cyclone inlet dimensions on the flow pattern and performance. *Applied Mathematical Modelling*, 35(4):1952–1968.

[40] Escudier, M. (1984). Observations of the flow produced in a cylindrical container by a rotating endwall. *Experiments in Fluids*, 2(4):189–196.

[41] Ferziger, J. H. and Perić, M. (2002). *Computational Methods for Fluid Dynamics*, volume 3. Springer Berlin, 3rd edition.

[42] Finch, J. M. (1885). Dust-Collectors. US Patent 325,521.

[43] First, M. (1949). Cyclone dust collector design. In *Am. Soc. Mech. Eng*, volume 49, pages 127–132.

[44] Flagan, R. C. and Seinfeld, J. H. (2012). *Fundamentals of Air Pollution Engineering*. Courier Dover Publications.

[45] Frank, T., Yu, Q., Wassen, E., and Schneider, J. (1999). Experimental and numerical investigation of particle separation in a symmetrical double cyclone separator. In *Proceedings of the 3rd ASME/JSME Joint Fluids Engineering Conferences. San Francisco, California, USA*.

[46] Fraser, S., Abdel-Razek, A., and Abdullah, M. (1997). Computational and experimental investigations in a cyclone dust separator. *Proceedings of the Institution of Mechanical Engineers, Part E: Journal of Process Mechanical Engineering*, 211(4):247–257.

[47] Fujimura, K., Yoshizawa, H., Iwatsu, R., Koyama, H. S., and Hyun, J. M. (2001). Velocity measurements of vortex breakdown in an enclosed cylinder. *Journal of Fluids Engineering*, 123(3):604–611.

[48] Funk, P. and Baker, K. (2013). Dust cyclone technology for gins–a literature review. *Journal of Cotton Science*, 17(1):40–51.

[49] Gentry, R. A., Martin, R. E., and Daly, B. J. (1966). An eulerian differencing method for unsteady compressible flow problems. *Journal of Computational Physics*, 1(1):87–118.

[50] Geuzaine, C. and Remacle, J.-F. (2009). Gmsh: A 3-d finite element mesh generator with built-in pre-and post-processing facilities. *International Journal for Numerical Methods in Engineering*, 79(11):1309–1331.

[51] Gil, A., Romeo, L. M., and Cortes, C. (2002). Effect of the solid loading on a PFBC cyclone with pneumatic extraction of solids. *Chemical Engineering & Technology*, 25(4):407–415.

[52] Gimbun, J., Chuah, T., Fakhru'l-Razi, A., and Choong, T. S. (2005). The influence of temperature and inlet velocity on cyclone pressure drop: a CFD study. *Chemical Engineering and Processing: Process Intensification*, 44(1):7–12.

[53] Golub, G. H. and Van Loan, C. F. (2012). *Matrix Computations*, volume 3. JHU Press.

[54] Gooray, A., Watkins, C., and Aung, W. (1984). Improvements to the k-epsilon model for calculations of turbulent recirculating flow. In *4th Symposium on Turbulent Shear Flows*, volume 1, page 18.

[55] Gorton-Hülgerth, A., Woisetschläger, J., Wigley, G., and Staudinger, G. (2000). Investigation of the flow field in the upper part of a cyclone with laser and phase doppler anemometry. *Particle & Particle Systems Characterization*, 17(1):21–27.

[56] Green, D. et al. (2008). *Perry's Chemical Engineers' Handbook*, volume 796. McGraw-hill New York.

[57] Griffiths, W. and Boysan, F. (1996). Computational fluid dynamics CFD and empirical modelling of the performance of a number of cyclone samplers. *Journal of Aerosol Science*, 27(2):281 – 304.

[58] Gronald, G. and Derksen, J. (2011). Simulating turbulent swirling flow in a gas cyclone: a comparison of various modeling approaches. *Powder Technology*, 205(1):160–171.

[59] Harasek, M., Horvath, A., and Jordan, C. (2004). Investigation of dependence of gas flow on the geometry of cyclonic separators by CFD simulation. In *CHISA, 16th International Congress of Chemical and Process Engineering, Czech Republic, Prague*.

[60] Harlow, F. H. and Nakayama, P. I. (1968). Transport of turbulence energy decay rate. Technical report, Los Alamos Scientific Lab., N. Mex.

[61] Hellsten, A. (1998). Some improvements in Menter's k-ω SST turbulence model. *AIAA Paper*, 2554:1998.

[62] Hirsch, C. (2007). Chapter 9 - Time Integration Methods for Space-discretized Equations. In *Numerical Computation of Internal and External Flows*, pages 413 – 489. Butterworth-Heinemann, Oxford, 2nd edition.

[63] Hirsch, H. (1990). Numerical computation of internal and external flows. *Computational Methods for Inviscid and Viscous Flows*, 2:536–556.

[64] Hoekstra, A., Derksen, J., and Van Den Akker, H. (1999). An experimental and numerical study of turbulent swirling flow in gas cyclones. *Chemical Engineering Science*, 54(13):2055–2065.

[65] Hoekstra, A. J. (2000). *Gas Flow Field and Collection Efficiency of Cyclone Separators*. PhD thesis, TU Delft, Delft University of Technology.

[66] Hoffmann, A., Groot, M. D., and Hospers, A. (1996). The effect of the dust collection system on the flowpattern and separation efficiency of a gas cyclone. *The Canadian Journal of Chemical Engineering*, 74(4):464–470.

[67] Hoffmann, A. C. and Stein, L. E. (2007). *Gas Cyclones and Swirl Tubes: Principles, Design, and Operation*. Springer Science & Business Media.

[68] Hoffmannc, A., Van Santen, A., Allen, R., and Clift, R. (1992a). Effects of geometry and solid loading on the performance of gas cyclones. *Powder Technology*, 70(1):83–91.

[69] Hoffmannc, A., Van Santen, A., Allen, R., and Clift, R. (1992b). Effects of geometry and solid loading on the performance of gas cyclones. *Powder Technology*, 70(1):83–91.

[70] Horvath, A., Jordan, C., and Harasek, M. (2008). Influence of vortex-finder diameter on axial gas flow in simple cyclone. *Chemical Product and Process Modeling*, 3(1).

[71] Howard, J., Patankar, S., and Bordynuik, R. (1980). Flow prediction in rotating ducts using coriolis-modified turbulence models. *Journal of Fluids Engineering*, 102(4):456–461.

[72] Iozia, D. L. and Leith, D. (1989). Effect of cyclone dimensions on gas flow pattern and collection efficiency. *Aerosol Science and Technology*, 10(3):491–500.

[73] Iozia, D. L. and Leith, D. (1990). The logistic function and cyclone fractional efficiency. *Aerosol Science and Technology*, 12(3):598–606.

[74] Jasak, H. (1996). *Error Analysis and Estimation for the Finite Volume Method with Applications to Fluid Flows*. PhD thesis, University of London, UK.

[75] Karagoz, I. and Avci, A. (2005). Modelling of the pressure drop in tangential inlet cyclone separators. *Aerosol Science and Technology*, 39(9):857–865.

[76] Kim, J. and Lee, K. (1990). Experimental study of particle collection by small cyclones. *Aerosol Science and Technology*, 12(4):1003–1015.

[77] Knight, D. and Saffman, P. (1978). Turbulence model predictions for flows with significant mean streamline curvature. *AIAA Paper*, 258:1978.

[78] Lapple, C. (1951). Processes use many collector types. *Chemical Engineering*, 58(5):144–151.

[79] Lapple, C. and Shepherd, C. (1940). Calculation of particle trajectories. *Industrial & Engineering Chemistry*, 32(5):605–617.

[80] Launder, B. and Sharma, B. (1974). Application of the energy-dissipation model of turbulence to the calculation of flow near a spinning disc. *Letters in Heat and Mass Transfer*, 1(2):131–137.

[81] Leith, D. and Jones, D. (1997). Cyclones. In *Handbook of Powder Science & Technology*, pages 727–752. Springer US.

[82] Leith, D. and Licht, W. (1972). The collection efficiency of cyclone type particle collectors: a new theoretical approach. In *AIChE Symp. Ser*, volume 68, pages 196–206.

[83] LeVeque, R. J. (2002). *Finite Volume Methods for Hyperbolic Problems*, volume 31. Cambridge university press.

[84] Lissman, M. A. (1930). An analysis of mechanical methods of dust collection. *Chem. and Met. Eng*, pages 630–634.

[85] Liu, Z., Zheng, Y., Jia, L., Jiao, J., and Zhang, Q. (2006). Stereoscopic piv studies on the swirling flow structure in a gas cyclone. *Chemical Engineering Science*, 61(13):4252–4261.

[86] Ma, L., Ingham, D., and Wen, X. (2000). Numerical modelling of the fluid and particle penetration through small sampling cyclones. *Journal of Aerosol Science*, 31(9):1097 – 1119.

[87] Marschall, H. (2011). *Towards the Numerical Simulation of Multi-Scale Two-Phase Flows*. PhD thesis, Munchen, Technische Universitat Munchen, Diss., 2011.

[88] McDonough, J. (2004). *Introductory Lectures on Turbulence Physics, Mathematics and Modeling*. Citeseer.

[89] Menter, F. R. (1994). Two-equation eddy-viscosity turbulence models for engineering applications. *AIAA Journal*, 32(8):1598–1605.

[90] Monson, D., Seegmiller, H., and McConnaughey, P. (1990). Comparison of experiment with calculations using curvature-corrected zero and two equation turbulence models for a two-dimensional u-duct. In *AIAA, Fluid Dynamics, 21st Plasma Dynamics and Lasers Conference, 21st, Seattle, WA, June 18-20, 1990. 17 p.*, volume 1.

[91] Morweiser, M. and Bohnet, M. (1996). Influence of temperature and pressure on separation efficiency and pressure drop of aerocyclones. *High Temperature Gas Cleaning*, pages 26–39.

[92] Mousavian, S. and Najafi, A. (2009). Numerical simulations of gas–liquid–solid flows in a hydrocyclone separator. *Archive of Applied Mechanics*, 79(5):395–409.

[93] Muschelknautz, E. (1972). Die berechnung von zyklonabscheidern für gase. *Chemie Ingenieur Technik*, 44(1-2):63–71.

[94] Muschelknautz, E. and Krambrock, W. (1970). Aerodynamische beiwerte des zyklonabscheiders aufgrund neuer und verbesserter messungen. *Chemie Ingenieur Technik*, 42(5):247–255.

[95] Muzaferija, S. (1994). *Adaptive Finite Volume Method for Flow Prediction Using Unstructured Meshes and Multigrid Approach*. PhD thesis, University of London, UK.

[96] Narita, Y. (2012). *Plasma Turbulence in the Solar System*. Springer Science & Business Media.

[97] Ontko, J. (1996). Cyclone separator scaling revisited. *Powder Technology*, 87(2):93 – 104.

[98] OpenCFD (2014). The open source CFD toolbox. *User Guide, OpenCFD Ltd*.

[99] Park, S. and Chung, M. (1989). Curvature-dependent two-equation model for prediction of turbulent recirculating flows. *AIAA journal*, 27(3):340–344.

[100] Patankar, S. (1980). *Numerical Heat Transfer and Fluid Flow*. CRC Press.

[101] Peng, W., Boot, P., Udding, A., Hoffmann, A., Dries, H., Ekker, A., and Kater, J. (2001). Determining the best modelling assumptions for cyclones and swirl tubes by cfd and lda. *Proceeding, Session: Multiphase flow/CFD, Nuremberg Germany*, pages 27–29.

[102] Peng, W., Hoffmann, A., Boot, P., Udding, A., Dries, H., Ekker, A., and Kater, J. (2002). Flow pattern in reverse-flow centrifugal separators. *Powder Technology*, 127(3):212 – 222.

[103] Ramachandran, G., Leith, D., Dirgo, J., and Feldman, H. (1991). Cyclone optimization based on a new empirical model for pressure drop. *Aerosol Science and Technology*, 15(2):135–148.

[104] Reynolds, O. (1883). An experimental investigation of the circumstances which determine whether the motion of water shall be direct or sinuous, and of the law of resistance in parallel channels. *Proceedings of the Royal Society of London*, 35(224-226):84–99.

[105] Reynolds, O. (1894). On the dynamical theory of incompressible viscous fluids and the determination of the criterion. *Proceedings of the Royal Society of London*, 56(336-339):40–45.

[106] Rhodes, M. J. (2008). *Introduction to Particle Technology*. John Wiley & Sons, Ltd, Chichester, UK, 2nd edition.

[107] Richardson, L. F. (2007). *Weather Prediction by Numerical Process*. Cambridge University Press.

[108] Rosin, P., Rammler, E., and Intelmann, W. (1932). Principles and limits of cyclone dust removal. *Zeit. Ver. Deutscher Ing*, 76:433–437.

[109] Runchal, A. and Wolfshtein, M. (1969). Numerical integration procedure for the steady state navier-stokes equations. *Journal of Mechanical Engineering Science*, 11(5):445–453.

[110] Rusche, H. (2003). *Computational Fluid Dynamics of Dispersed Two-Phase Flows at High Phase Fractions*. PhD thesis, University of London, UK.

[111] Samarskii, A. A., Matus, P. P., and Vabishchevich, P. N. (2002). *Difference Schemes with Operator Factors*. Springer.

[112] Shalaby, H., Pachler, K., Wozniak, K., and Wozniak, G. (2005). Comparative study of the continuous phase flow in a cyclone separator using different turbulence models. *International Journal for Numerical Methods in Fluids*, 48(11):1175–1197.

[113] Shephered, C. and Lapple, C. (1939). Flow pattern and pressure drop in cyclone dust collectors. *Industrial & Engineering Chemistry*, 31(8):972–984.

[114] Slack, M., Prasad, R., Bakker, A., and Boysan, F. (2000). Advances in cyclone modelling using unstructured grids. *Chemical Engineering Research and Design*, 78(8):1098 – 1104.

[115] Smirnov, P. E. and Menter, F. R. (2009). Sensitization of the SST turbulence model to rotation and curvature by applying the spalart–shur correction term. *Journal of Turbomachinery*, 131(4):041010.

[116] Smolik, J. (1975). Air pollution abatement, part I, scriptum no. 401-2099. *Techn. Univ. of Prague*.

[117] Solero, G. and Coghe, A. (2002). Experimental fluid dynamic characterization of a cyclone chamber. *Experimental Thermal and Fluid Science*, 27(1):87 – 96.

[118] Spalart, P. and Shur, M. (1997). On the sensitization of turbulence models to rotation and curvature. *Aerospace Science and Technology*, 1(5):297–302.

[119] Spalart, P. R. (2009). Detached-eddy simulation. *Annual Review of Fluid Mechanics*, 41:181–202.

[120] Spalart, P. R. and Allmaras, S. R. (1992). A one-equation turbulence model for aerodynamic flows. *AIAA Paper*, 92-0439, 1992.

[121] Stairmand, C. (1949). Pressure drop in cyclone separators. *Engineering*, 168:409–412.

[122] Stairmand, C. J. (1951). The design and performance of cyclone separators. *Trans. Inst. Chem. Eng*, 29:356–383.

[123] Swaray, S.-G. and Hamdullahpur, F. (2004). A new semi-empirical model for predicting particulate collection efficiency in low-to-high temperature gas cyclone separators. *Advanced Powder Technology*, 15(2):137–164.

[124] Ter Linden, A. (1949). Investigations into cyclone dust collectors. *Proceedings of the Institution of Mechanical Engineers*, 160(1):233–251.

[125] Theodore, L. and Paola, V. D. (1980). Predicting cyclone efficiency. *Journal of the Air Pollution Control Association*, 30(10):1132–1133.

[126] Toro, E. F. (2009). *Riemann Solvers and Numerical Methods for Fluid Dynamics: a Practical Introduction*. Springer Science & Business Media.

[127] Utikar, R., Darmawan, N., Tade, M., Li, Q., Evans, G., Glenny, M., Pareek, V., et al. (2010). Hydroynamic simulation of cyclone separators| nova. the university of newcastle's digital repository.

[128] Vahl, D. and Mallinson, G. (1972). False diffusion in numerical fluid mechanics. Technical report, New South Wales, Australia: Univ. of New South Wales, School of Mech. and Ind. Eng. Dept.

[129] Velilla, J. (2005). *Study of the flow at a PFBC cyclone dipleg*. PhD thesis.

[130] Versteeg, H. K. and Malalasekera, W. (2007). *An Introduction to Computational Fluid Dynamics: the finite volume method*. Pearson Education.

[131] Vesilind, P. (1980). The Rosin-Rammler particle size distribution. *Resource Recovery and Conservation*, 5(3):275 – 277.

[132] Weller, H. G., Tabor, G., Jasak, H., and Fureby, C. (1998). A tensorial approach to computational continuum mechanics using object-oriented techniques. *Computers in Physics*, 12(6):620–631.

[133] Wesseling, P. (2009). *Principles of Computational Fluid Dynamics*, volume 29. Springer Science & Business Media.

[134] Wilcox, D. C. et al. (2006). *Turbulence Modeling for CFD*. DCW Industries, third edition.

[135] Xiang, R., Park, S., and Lee, K. (2001). Effects of cone dimension on cyclone performance. *Journal of Aerosol Science*, 32(4):549 – 561.

[136] Yakhot, V., Orszag, S., Thangam, S., Gatski, T., and Speziale, C. (1992). Development of turbulence models for shear flows by a double expansion technique. *Physics of Fluids A: Fluid Dynamics (1989-1993)*, 4(7):1510–1520.

[137] Yoshida, H. (1996). Three-dimensional simulation of air cyclone and particle separation by a revised-type cyclone. *Colloids and Surfaces A: Physicochemical and Engineering Aspects*, 109(0):1 – 12.

[138] Zhang, Q. and Yang, Y. (2013). A new simpler rotation/curvature correction method for spalart–allmaras turbulence model. *Chinese Journal of Aeronautics*, 26(2):326–333.

[139] Zhao, B. (2004). A theoretical approach to pressure drop across cyclone separators. *Chemical Engineering & Technology*, 27(10):1105–1108.

[140] Zhao, B. and Su, Y. (2006). Particle collection theory for cyclone separators: Summary and comparison. *Particle & Particle Systems Characterization*, 23(6):484–488.

[141] Zhou, L. and Soo, S. (1990). Gas—solid flow and collection of solids in a cyclone separator. *Powder Technology*, 63(1):45 – 53.

Appendix A

SSTCCM Code

```
#include "kOmegaSSTCCM.H"
#include "addToRunTimeSelectionTable.H"
#include "backwardsCompatibilityWallFunctions.H"
// ************************************************//
namespace Foam
{
namespace incompressible
{
namespace RASModels
{
//*************** Static Data Members ***************//
defineTypeNameAndDebug(kOmegaSSTCCM, 0);
addToRunTimeSelectionTable(RASModel, kOmegaSSTCCM, dictionary);
//************* Private Member Functions *************//
tmp<volScalarField> kOmegaSSTCCM::F1(const volScalarField& CDkOmega)
    const
{
    tmp<volScalarField> CDkOmegaPlus = max
    (
        CDkOmega,
        dimensionedScalar("1.0e-20", dimless/sqr(dimTime), 1.0e-20)
    );
    tmp<volScalarField> arg1 = min
    (
        min
        (
            max
            (
                (scalar(1)/betaStar_)*sqrt(k_)/(omega_*y_),
                scalar(500)*nu()/(sqr(y_)*omega_)
            ),
            (4*alphaOmega2_)*k_/(CDkOmegaPlus*sqr(y_))
        ),
        scalar(10)
    );
    return tanh(pow4(arg1));
}
tmp<volScalarField> kOmegaSSTCCM::F2() const
{
    tmp<volScalarField> arg2 = min
    (
```

```
            max
            (
                (scalar(2)/betaStar_)*sqrt(k_)/(omega_*y_),
                scalar(500)*nu()/(sqr(y_)*omega_)
            ),
            scalar(100)
        );
        return tanh(sqr(arg2));
}
tmp<volScalarField> kOmegaSSTCCM::F3() const
{
        tmp<volScalarField> arg3 = min
        (
            150*nu()/(omega_*sqr(y_)),
            scalar(10)
        );

        return 1 - tanh(pow4(arg3));
}
tmp<volScalarField> kOmegaSSTCCM::F23() const
{
        tmp<volScalarField> f23(F2());

        if (F3_)
        {
            f23() *= F3();
        }
        return f23;
}
//*************** Constructors ***************//
kOmegaSSTCCM::kOmegaSSTCCM
(
        const volVectorField& U,
        const surfaceScalarField& phi,
        transportModel& transport,
        const word& turbulenceModelName,
        const word& modelName
)
:
        RASModel(modelName, U, phi, transport, turbulenceModelName),
        cr1_
        (
            dimensioned<scalar>::lookupOrAddToDict
            (
                "cr1",
                coeffDict_,
                1.0
            )
        ),
        cr2_
        (
            dimensioned<scalar>::lookupOrAddToDict
            (
                "cr2",
                coeffDict_,
                2.0
            )
        ),
```

```
    cr3_
    (
        dimensioned<scalar>::lookupOrAddToDict
        (
            "cr3",
            coeffDict_,
            1.0
        )
    ),
    alphaK1_
    (
        dimensioned<scalar>::lookupOrAddToDict
        (
            "alphaK1",
            coeffDict_,
            0.85034
        )
    ),
    alphaK2_
    (
        dimensioned<scalar>::lookupOrAddToDict
        (
            "alphaK2",
            coeffDict_,
            1.0
        )
    ),
    alphaOmega1_
    (
        dimensioned<scalar>::lookupOrAddToDict
        (
            "alphaOmega1",
            coeffDict_,
            0.5
        )
    ),
    alphaOmega2_
    (
        dimensioned<scalar>::lookupOrAddToDict
        (
            "alphaOmega2",
            coeffDict_,
            0.85616
        )
    ),
    gamma1_
    (
        dimensioned<scalar>::lookupOrAddToDict
        (
            "gamma1",
            coeffDict_,
            0.5532
        )
    ),
    gamma2_
    (
        dimensioned<scalar>::lookupOrAddToDict
        (
```

```
                "gamma2",
                coeffDict_,
                0.4403
            )
    ),
    beta1_
    (
        dimensioned<scalar>::lookupOrAddToDict
        (
            "beta1",
            coeffDict_,
            0.075
        )
    ),
    beta2_
    (
        dimensioned<scalar>::lookupOrAddToDict
        (
            "beta2",
            coeffDict_,
            0.0828
        )
    ),
    betaStar_
    (
        dimensioned<scalar>::lookupOrAddToDict
        (
            "betaStar",
            coeffDict_,
            0.09
        )
    ),
    a1_
    (
        dimensioned<scalar>::lookupOrAddToDict
        (
            "a1",
            coeffDict_,
            0.31
        )
    ),
    b1_
    (
        dimensioned<scalar>::lookupOrAddToDict
        (
            "b1",
            coeffDict_,
            1.0
        )
    ),
    c1_
    (
        dimensioned<scalar>::lookupOrAddToDict
        (
            "c1",
            coeffDict_,
            10.0
        )
```

```
    ),
    F3_
    (
        Switch::lookupOrAddToDict
        (
            "F3",
            coeffDict_,
            false
        )
    ),
    y_(mesh_),
    k_
    (
        IOobject
        (
            "k",
            runTime_.timeName(),
            mesh_,
            IOobject::NO_READ,
            IOobject::AUTO_WRITE
        ),
        autoCreateK("k", mesh_)
    ),
    omega_
    (
        IOobject
        (
            "omega",
            runTime_.timeName(),
            mesh_,
            IOobject::NO_READ,
            IOobject::AUTO_WRITE
        ),
        autoCreateOmega("omega", mesh_)
    ),
    nut_
    (
        IOobject
        (
            "nut",
            runTime_.timeName(),
            mesh_,
            IOobject::NO_READ,
            IOobject::AUTO_WRITE
        ),
        autoCreateNut("nut", mesh_)
    )
{
    bound(k_, kMin_);
    bound(omega_, omegaMin_);

    nut_ =
    (
        a1_*k_
      / max
        (
            a1_*omega_,
            b1_*F23()*sqrt(2.0)*mag(symm(fvc::grad(U_)))
```

```
        )
    );
    nut_.correctBoundaryConditions();

    printCoeffs();
}
//*************** Member Functions ***************//
tmp<volSymmTensorField> kOmegaSSTCCM::R() const
{
    return tmp<volSymmTensorField>
    (
        new volSymmTensorField
        (
            IOobject
            (
                "R",
                runTime_.timeName(),
                mesh_,
                IOobject::NO_READ,
                IOobject::NO_WRITE
            ),
            ((2.0/3.0)*I)*k_ - nut_*twoSymm(fvc::grad(U_)),
            k_.boundaryField().types()
        )
    );
}
tmp<volSymmTensorField> kOmegaSSTCCM::devReff() const
{
    return tmp<volSymmTensorField>
    (
        new volSymmTensorField
        (
            IOobject
            (
                "devRhoReff",
                runTime_.timeName(),
                mesh_,
                IOobject::NO_READ,
                IOobject::NO_WRITE
            ),
           -nuEff()*dev(twoSymm(fvc::grad(U_)))
        )
    );
}
tmp<fvVectorMatrix> kOmegaSSTCCM::divDevReff(volVectorField& U) const
{
    return
    (
      - fvm::laplacian(nuEff(), U)
      - fvc::div(nuEff()*dev(T(fvc::grad(U))))
    );
}
tmp<fvVectorMatrix> kOmegaSSTCCM::divDevRhoReff
(
    const volScalarField& rho,
    volVectorField& U
) const
{
```

```
    volScalarField muEff("muEff", rho*nuEff());

    return
    (
      - fvm::laplacian(muEff, U)
      - fvc::div(muEff*dev(T(fvc::grad(U))))
    );
}
bool kOmegaSSTCCM::read()
{
    if (RASModel::read())
    {
        cr1_.readIfPresent(coeffDict());
        cr2_.readIfPresent(coeffDict());
        cr3_.readIfPresent(coeffDict());
        alphaK1_.readIfPresent(coeffDict());
        alphaK2_.readIfPresent(coeffDict());
        alphaOmega1_.readIfPresent(coeffDict());
        alphaOmega2_.readIfPresent(coeffDict());
        gamma1_.readIfPresent(coeffDict());
        gamma2_.readIfPresent(coeffDict());
        beta1_.readIfPresent(coeffDict());
        beta2_.readIfPresent(coeffDict());
        betaStar_.readIfPresent(coeffDict());
        a1_.readIfPresent(coeffDict());
        b1_.readIfPresent(coeffDict());
        c1_.readIfPresent(coeffDict());
        F3_.readIfPresent("F3", coeffDict());

        return true;
    }
    else
    {
        return false;
    }
}
void kOmegaSSTCCM::correct()
{
    RASModel::correct();
    if (!turbulence_)
    {
        return;
    }
    if (mesh_.changing())
    {
        y_.correct();
    }
    const volScalarField S2(2*magSqr(symm(fvc::grad(U_))));
    volScalarField G(GName(), nut_*S2);
    tmp<volTensorField> tgradU = fvc::grad(U_);
    tmp<volTensorField> tSkew = skew(tgradU());
    tmp<volSymmTensorField> tSymm = symm(tgradU());
    volScalarField symInnerProduct =
    (
         max(2.0*tSymm()&&tSymm(),
         dimensionedScalar("small", dimensionSet(0, 0, -2, 0, 0), SMALL)
   )
      );
```

```
    volScalarField asymInnerProduct =
    (
        max(2.0*tSkew()&&tSkew(),
        dimensionedScalar("small", dimensionSet(0, 0, -2, 0, 0), SMALL))
     );
    volScalarField rStar = sqrt(symInnerProduct/asymInnerProduct);
    tgradU.clear();
    // Update omega and G at the wall
    omega_.boundaryField().updateCoeffs();
    tSkew.clear();
    tSymm.clear();
    volScalarField rTilda = (scalar(1.0)-rStar)/(rStar*rStar);
    volScalarField Frot
    (
        IOobject
        (
            "Frot",
            runTime_.timeName(),
            mesh_,
            IOobject::NO_READ,
            IOobject::AUTO_WRITE
        ),
        max
        (
            min
            (
                (scalar(1.0)+cr1_)*2.0*rStar/(scalar(1)+rStar)*(scalar(1.0)
                -cr3_*atan(cr2_*rTilda))-cr1_,
                scalar(1.25)
            ),
            scalar(0.0))
    );
    rStar.clear();
    rTilda.clear();
    const volScalarField CDkOmega
    (
        (2*alphaOmega2_)*(fvc::grad(k_) & fvc::grad(omega_))/omega_
    );
    const volScalarField F1(this->F1(CDkOmega));
    // Turbulent frequency equation
    tmp<fvScalarMatrix> omegaEqn
    (
        fvm::ddt(omega_)
      + fvm::div(phi_, omega_)
      - fvm::laplacian(DomegaEff(F1), omega_)
     ==
        gamma(F1)*S2*Frot
      - fvm::Sp(beta(F1)*omega_, omega_)
      - fvm::SuSp
        (
            (F1 - scalar(1))*CDkOmega/omega_,
            omega_
        )
    );
    omegaEqn().relax();
    omegaEqn().boundaryManipulate(omega_.boundaryField());
```

```
    solve(omegaEqn);
    bound(omega_, omegaMin_);
    // Turbulent kinetic energy equation
    tmp<fvScalarMatrix> kEqn
    (
        fvm::ddt(k_)
      + fvm::div(phi_, k_)
      - fvm::laplacian(DkEff(F1), k_)
     ==
       min(G*Frot, c1_*betaStar_*k_*omega_)
      - fvm::Sp(betaStar_*omega_, k_)
    );
    kEqn().relax();
    solve(kEqn);
    bound(k_, kMin_);
    // Re-calculate viscosity
    nut_ = a1_*k_/max(a1_*omega_, b1_*F23()*sqrt(S2));
    nut_.correctBoundaryConditions();
}
//*************************************************//
} // End namespace RASModels
} // End namespace incompressible
} // End namespace Foam
// *************************************************//
```

Appendix B

Finite Volume Scheme Directory

```
/*--------------------------------*- C++ -*----------------------------------*\
| =========                 |                                                 |
| \\      /  F ield         | OpenFOAM: The Open Source CFD Toolbox           |
|  \\    /   O peration     | Version:  2.3.1                                 |
|   \\  /    A nd           | Web:      www.OpenFOAM.org                      |
|    \\/     M anipulation  |                                                 |
\*---------------------------------------------------------------------------*/
FoamFile
{
    version     2.0;
    format      ascii;
    class       dictionary;
    location    "system";
    object      fvSchemes;
}
// * * * * * * * * * * * * * * * * * * * * * * * * * * * * * * * * * * * * * //
ddtSchemes
{
    default         backward;//Euler;
}
gradSchemes
{
    default         Gauss linear;
    grad(p)         Gauss linear;
    grad(U)         Gauss linear;
    grad(k)         Gauss linear;
    grad(omega)     Gauss linear;
}
divSchemes
{
    default         none;
    div(phi,U)      Gauss linearUpwindV grad(U);
    div(phi,k)      Gauss linearUpwind grad(k);
    div(phi,omega)  Gauss linearUpwind grad(omega);
    div((nuEff*dev(T(grad(U))))) Gauss linear;
}
laplacianSchemes
{
    default         Gauss linear limited corrected 0.5;
}
interpolationSchemes
```

```
{
    default            linear;
}

snGradSchemes
{
    default            corrected;
}
fluxRequired
{
    default            no;
    p;
}
// ************************************************************** //
```

Appendix C

Finite Volume Solution Directory

```
/*--------------------------------*- C++ -*----------------------------------*\
| =========                 |                                                 |
| \\      /  F ield         | OpenFOAM: The Open Source CFD Toolbox           |
|  \\    /   O peration     | Version:  2.3.1                                 |
|   \\  /    A nd           | Web:      www.OpenFOAM.org                      |
|    \\/     M anipulation  |                                                 |
\*---------------------------------------------------------------------------*/
FoamFile
{
    version     2.0;
    format      ascii;
    class       dictionary;
    location    "system";
    object      fvSolution;
}
// * * * * * * * * * * * * * * * * * * * * * * * * * * * * * * * * * * * * //
solvers
{
    p
    {
        solver                  GAMG;
        tolerance               1e-05;
        relTol                  0.01;
        smoother                DICGaussSeidel;
        cacheAgglomeration      true;
        nCellsInCoarsestLevel   500;
        agglomerator            faceAreaPair;
        mergeLevels             1;
    }
    pFinal
    {
        $p;
        tolerance               1e-05;
        relTol                  0;
    }
    U
    {
        solver                  PBiCG;
        preconditioner          DILU;
        tolerance               1e-06;
        relTol                  0.01;
```

```
    }
    UFinal
    {
        $U;
        tolerance           1e-06;
        relTol              0;
    }
    "(k|omega)"
    {
        solver              smoothSolver;
        smoother            DILUGaussSeidel;
        tolerance           1e-10;
        relTol              0.01;
    }
    "(k|omega)Final"
    {
        solver              smoothSolver;
        smoother            DILUGaussSeidel;
        tolerance           1e-10;
        relTol              0;
    }
}
PIMPLE
{
    nOuterCorrectors            1;
    nCorrectors                 2;
    nNonOrthogonalCorrectors    3;
}
relaxationFactors
{
    U       0.7;
    k       0.7;
    omega   0.7;
    p       0.3;
}

// ************************************************************** //
```

Appendix D

snappyHexMeshDict Directory

```
/*--------------------------------*- C++ -*----------------------------------*\
| =========                 |                                                 |
| \\      /  F ield         | OpenFOAM: The Open Source CFD Toolbox           |
|  \\    /   O peration     | Version:  2.3.1                                 |
|   \\  /    A nd           | Web:      www.OpenFOAM.org                      |
|    \\/     M anipulation  |                                                 |
\*---------------------------------------------------------------------------*/
FoamFile
{
    version     2.0;
    format      ascii;
    class       dictionary;
    location    "system";
    object      snappyHexMeshDict;
}
// * * * * * * * * * * * * * * * * * * * * * * * * * * * * * * * * * * * * //

castellatedMesh true;
snap            true;
addLayers       false;
geometry
{
        inlet.stl {type triSurfaceMesh; name inlet;}
        hopper.stl {type triSurfaceMesh; name hopper;}
        walls1.stl {type triSurfaceMesh; name walls1;}
        walls2.stl {type triSurfaceMesh; name walls2;}
        walls2e.stl {type triSurfaceMesh; name walls2e;}
        walls3.stl {type triSurfaceMesh; name walls3;}
        walls4.stl {type triSurfaceMesh; name walls4;}
        //volume.stl {type triSurfaceMesh; name volume;}
};
castellatedMeshControls
{
    maxLocalCells 1000000;
    maxGlobalCells 2000000;
    minRefinementCells 10;
    maxLoadUnbalance 0.10;
    nCellsBetweenLevels 1;
    features
    (
        {file "walls1.eMesh"; level 0;}
```

```
        {file "inlet.eMesh"; level 0;}
        {file "hopper.eMesh"; level 0;}
        {file "walls2.eMesh"; level 0;}
        {file "walls2e.eMesh"; level 0;}
        {file "walls3.eMesh"; level 0;}
        {file "walls4.eMesh"; level 0;}
    );
    refinementSurfaces
    {
        inlet {level (0 0);}
        hopper {level (0 0);}
        walls1 {level (0 0);}
        walls2 {level (0 0);}
        walls2e{level (0 0);}
        walls3 {level (0 0);}
        walls4 {level (0 0);}
    }
    resolveFeatureAngle 80;
    refinementRegions
    {
    }
    locationInMesh (0 0 0.5);
    allowFreeStandingZoneFaces true;
}
snapControls
{
    nSmoothPatch 3;
    tolerance 4.0;
    nSolveIter 30;
    nRelaxIter 5;
    nFeatureSnapIter 15;
  implicitFeatureSnap false;
  explicitFeatureSnap true;
  multiRegionFeatureSnap false;
}
addLayersControls
{
    relativeSizes false;
    layers
    {
        walls2
          {nSurfaceLayers 5;}
        walls4
          {nSurfaceLayers 5;}
    }
    expansionRatio 1.3;
    finalLayerThickness 1.070781e-3;
    minThickness 3.749104e-4;
    nGrow 0;
    featureAngle 80;
    nRelaxIter 3;
    nSmoothSurfaceNormals 1;
    nSmoothNormals 3;
    nSmoothThickness 10;
    maxFaceThicknessRatio 0.5;
    maxThicknessToMedialRatio 0.3;
    minMedianAxisAngle 130;
    nBufferCellsNoExtrude 0;
```

```
    nLayerIter 30;
}
meshQualityControls
{
    maxNonOrtho 65;
    maxBoundarySkewness 20;
    maxInternalSkewness 4;
    maxConcave 90;
    minFlatness 0.5;
    minVol 1e-13;
    minTetQuality 1e-9;
    minArea -1;
    minTwist 0.02;
    minDeterminant 0.001;
    minFaceWeight 0.02;
    minVolRatio 0.01;
    minTriangleTwist -1;
    nSmoothScale 4;
    errorReduction 0.75;
}
debug 0;
mergeTolerance 1E-6;
// ************************************************************************* //
```